Tracking active sites in metal-TiO_2 systems for photocatalytic H_2 production by *in situ* and *operando* spectroscopies

Elizaveta Kozyr

Università degli Studi di Torino
Doctoral School of the University of Torino
PhD Program in Chemical and Materials
Sciences XXXVII Cycle

Supervisor:
Prof. Lorenzo Mino
Co-supervisor:
Dr. hab. Aram Bugaev

Università degli Studi di Torino
Doctoral School of the University of Torino
PhD Program in Chemical and Materials Sciences XXXVII Cycle

Tracking active sites in metal-TiO_2 systems for photocatalytic H_2 production by *in situ* and *operando* spectroscopies

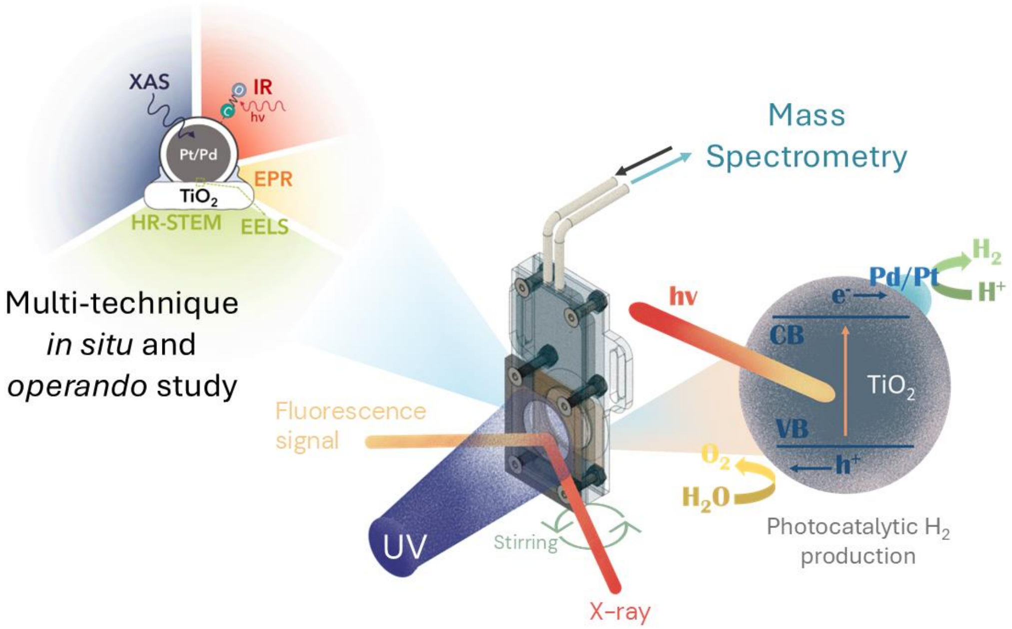

Elizaveta Kozyr

Supervisor: Prof. Lorenzo Mino

Co-supervisor: Dr. hab. Aram Bugaev

Università degli Studi di Torino

Doctoral School of the University of Torino

PhD Program in Chemical and Materials Sciences XXXVII cycle

Tracking active sites in metal-TiO_2 systems for photocatalytic H_2 production by *in situ* and *operando* spectroscopies

Candidate: **Elizaveta Kozyr**

Supervisor: Prof. **Lorenzo Mino**

Co-supervisor: Dr. hab. **Aram Bugaev**
Paul Scherrer Institute

Jury Members: Prof. **Elena Clara Groppo**
Dipartimento di Chimica
Università degli Studi di Torino

Dr. **Mickaël Rivallan**
Physics and Analysis Division
IFP Energies nouvelles

Prof. **Jeroen Anton van Bokhoven**
Department of Chemistry and Applied Biosciences
ETH Zürich

Head of the Doctoral School: Prof. Alberto Rizzuti
PhD Program Coordinator: Prof. Bartolome Civalleri

Torino, 2024

PREFACE

Photocatalytic hydrogen (H_2) production represents a promising pathway for sustainable energy generation by using solar energy to drive water splitting reactions. Metal-TiO_2 systems are at the forefront of this research due to their unique catalytic properties and potential for high efficiency in H_2 production. However, the identification and understanding of active sites within these complex systems remain a significant challenge. Traditional characterization methods often fail to provide real-time insights into the dynamic processes occurring at the catalytic interface. This study addresses these challenges by employing *in situ* and *operando* spectroscopic methods to track the evolution and performance of active sites in metal-TiO_2 photocatalysts. This approach offers a comprehensive understanding of the catalytic mechanisms at work, thereby advancing the design and optimization of efficient photocatalysts for hydrogen production. The thesis is sub-divided into the following parts:

Chapter 1. TiO_2 based systems for photocatalytic hydrogen production

The first chapter of the thesis provides an overview of significant research made in the area of photocatalytic hydrogen production. It outlines the importance of creating new hydrogen production strategies for a green renewable energy future. The focus of the chapter is on TiO_2-based photocatalytic systems, highlighting their advantages, disadvantages, and restrictions for hydrogen production. Particular attention is given to the primary mechanisms for enhancing photocatalytic activity. Various modifications to the TiO_2 system are overviewed, with a particular emphasis on noble metal nanoparticles, which are among the most commonly used co-catalysts.

Chapter 2. *In situ/operando* spectroscopy in photocatalysis

This chapter covers a wide range of *in situ* and *operando* spectroscopic techniques, with a special focus on X-ray absorption spectroscopy (XAS). It concludes with an assessment of surface characterization techniques such as infrared (IR) spectroscopy applied to the study of photocatalysts. The chapter highlights the critical role and importance of combining multiple spectroscopic tools supported by complementary techniques such as transmission electron microscopy (TEM) to more thoroughly characterize the properties of metal nanoparticle-supported on titania. Furthermore, the inherent challenges and complexities associated with performing *in situ* and *operando* measurements in the context of photocatalysis are discussed.

Chapter 3. Materials and methods

The first part of this chapter explains the sample preparation strategies used in this work. It describes the synthesis procedures for the different morphologies of TiO_2 support and two methods of metal deposition on it. Additionally, it provides experimental details of the techniques employed in the analysis in this thesis, such as XAS, Fourier Transform Infrared Spectroscopy (FT-IR), Scanning Transmission Electron Microscopy (STEM) with Energy Dispersive X-ray (EDX) mapping analysis, and Electron Energy Loss Spectroscopy (EELS) and others. The combined application of *in situ/operando* laboratory spectroscopy and synchrotron spectroscopy represents the novelty of this project.

Chapter 4. *Operando* spectroscopic study of Pt/TiO_2 photocatalyst during photodeposition and hydrogen evolution reaction

This chapter is devoted to *operando* spectroscopic research of catalytic system during photodeposition of Pt on TiO_2 and photostimulated H_2 production. For the study a custom-made 3D-printed photocatalytic cell was designed, which allows one to perform simultaneous XAS, UV-Vis and mass spectrometry measurements. Preliminary results were obtained in laboratory conditions using a Rigaku XAS spectrometer, where the photodeposition process was studied in detail. Afterwards, the study was carried out at the synchrotron radiation source at ESRF. The study was also supplemented by studying the effect of titanium dioxide morphology during the photodeposition of platinum on it and the role of the effect of metal-support interaction on the redox properties of the sample.

Chapter 5. *In situ* photodeposition of palladium particles on TiO_2

Continuing the topic of the previous chapter concerning the photodeposition process of metals on TiO_2, this chapter follows the formation of Pd/TiO_2 photocatalyst by the combination of *in situ* XAS spectroscopy with high angle annular dark field scanning transmission electron microscopy (HAADF-STEM), as a powerful workflow for detailed investigation of the formation mechanisms of the catalysts. In this study, a similar 3D-printed cell was used at a synchrotron light source to follow the formation steps of Pd/TiO_2 photocatalysts.

Chapter 6. Origin of strong metal-support interaction in Pd/TiO_2 catalysts and its impact on structural and redox properties

The unusual redox properties discovered in the previous sections for Pt and Pd/TiO_2 catalysts were attributed to the strong-metal support interaction (SMSI), whose formation and effect on the structural and electronic properties of samples was investigated in detail in this section for the case of Pd/TiO_2. Two samples, synthesized by photodeposition and deposition-precipitation techniques were considered. The different behavior of the samples under oxidizing and reducing conditions was investigated by several *in situ* experimental methods, including XAS, high-resolution scanning transmission electron microscopy (HR-STEM), IR spectroscopy, and electron paramagnetic resonance (EPR) spectroscopy. This chapter also highlighting that the synthesis procedure is one of the key factors of SMSI formation.

Chapter 7. Conclusions

The final chapter summarizes the main findings and ideas gained from the research presented in the thesis, reporting also some perspectives and possible future research developments of the project.

Chapter 8. Side activities

This chapter provides an overview of several parallel research projects that, while not included in the main body of my PhD thesis, significantly contributed to my understanding of photocatalysis and catalyst characterization. These studies, conducted in collaboration with colleagues from the University of Turin, ALBA Synchrotron, Paul Scherrer Institute, KU Leuven, Southern Federal University and the University of Palermo, focused on the use of *in situ* and *operando* spectroscopic characterization of different catalytic systems. These supplementary projects deepened my expertise in *operando* and *in situ* spectroscopy, as well as theoretical methods, provided insights into catalyst behavior based on noble metals, and offered valuable data that complemented and enhanced the findings in my primary research.

1 TiO_2 based systems for photocatalytic hydrogen production

1.1 Hydrogen production: state of the art and challenges

Energy lies at the core of the climate problem and is the key to its solution. One of the most significant challenges of our time is the replacement of traditional carbon-based fuels with alternative energy sources that do not comply with restrictions. The revised Renewable Energy Directive raised the EU's overall target for renewable energy consumption to 32% by 2030 [1]. To achieve this goal, there is a need to create and exploit effective and alternative environmentally friendly energy sources. Hydrogen is increasingly recognized as a pivotal element in the transition towards sustainable energy systems. In the modern world, hydrogen is utilized in various sectors, including transportation, industry, production of chemicals, and power generation. The potential for hydrogen to be produced from renewable sources further enhances its appeal, aligning with global efforts to reduce carbon emissions. It has the potential to become the most desirable fuel of the future, because of its energy capacity (142 MJ/mol) which surpasses twice the amount energy received by fossil fuels, with a huge advantage of not having the CO_2 emission.

Despite the great potential of hydrogen applications, its storage and transportation still pose significant technical and economic challenges. Hydrogen has a very low energy density in its gaseous form, meaning it must be either compressed to high pressures (up to 700 bar) or liquefied at extremely low temperatures (−253 °C) for efficient storage and transport. Both methods require advanced materials and technologies, which increase costs and energy consumption. Compressed hydrogen storage requires specialized high-strength tanks that can withstand high pressures, while liquefied hydrogen storage involves costly cryogenic systems to maintain low temperatures. Transportation also faces obstacles due to hydrogen's highly flammable nature and the need for specialized infrastructure, such as pipelines or hydrogen-compatible vehicles.

These difficulties are compounded by the fact that currently, the main hydrogen production technologies are associated with fossil fuels, which ultimately looks like a vicious circle. Hydrogen can be produced by the so-called grey or blue hydrogen ways (***Figure 1***). Grey hydrogen is produced through steam methane reforming (SMR), where natural gas is heated with steam to produce hydrogen, along with significant carbon dioxide (CO_2) emissions. This method is widely used but has a high environmental impact due to the release of CO_2. Blue hydrogen is also produced via SMR, but the key difference is that the CO_2 emissions are captured and stored through carbon capture and storage technologies. While blue hydrogen is less environmentally harmful than grey hydrogen, it still relies on fossil fuels.

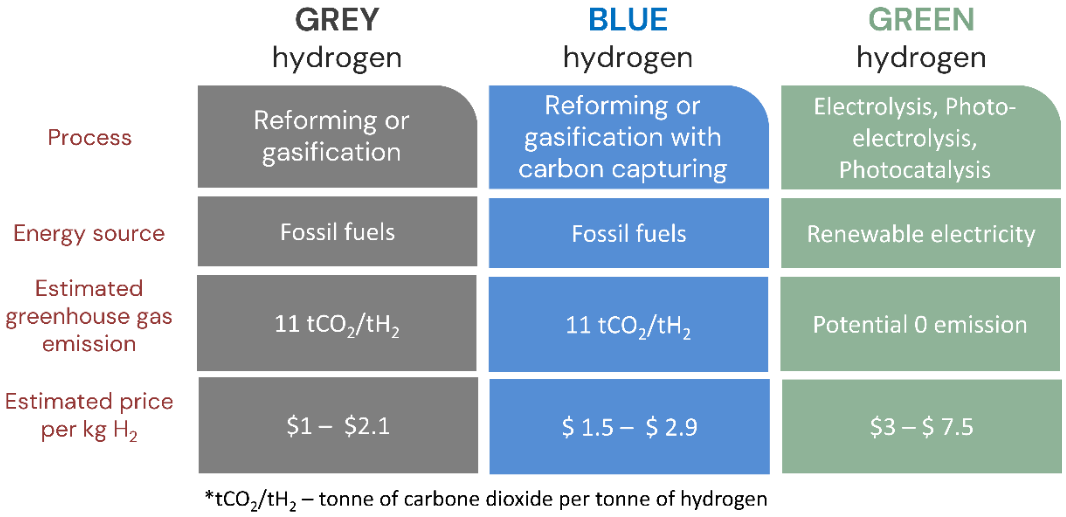

	GREY hydrogen	**BLUE** hydrogen	**GREEN** hydrogen
Process	Reforming or gasification	Reforming or gasification with carbon capturing	Electrolysis, Photo-electrolysis, Photocatalysis
Energy source	Fossil fuels	Fossil fuels	Renewable electricity
Estimated greenhouse gas emission	11 tCO_2/tH_2	11 tCO_2/tH_2	Potential 0 emission
Estimated price per kg H_2	\$1 – \$2.1	\$ 1.5 – \$ 2.9	\$3 – \$ 7.5

*tCO_2/tH_2 – tonne of carbone dioxide per tonne of hydrogen

Figure 1. The source of feedstock for hydrogen is determined by its ‘color’ name. Adopted from [2].

Efforts are constantly being made to develop and refine a transit from traditional grey or blue hydrogen production to green hydrogen technology to make it more efficient and environmentally friendly. Its production can be achieved using renewable energy sources, which are sustainable and reduce environmental impact [3].

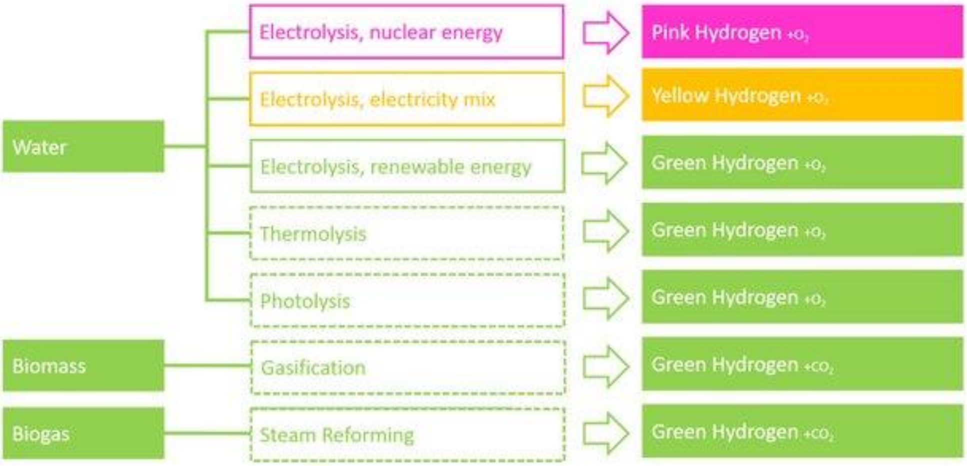

Figure 2. Overview of possible hydrogen production by various technologies using renewable and electricity sources. Dashed boxes indicate technologies that are not yet available on an industrial scale. Adopted from [4].

What are the most efficient ways to produce green hydrogen?

Figure 2 presents the available methods according to the energy used to drive the process. These methods include those powered by a single form of energy (electrical, thermal, photonic, or biochemical), hybrid methods that use two forms of energy (electrical + thermal, electrical + photonic, biochemical + thermal, photonic + biochemical) have been identified [4, 5]. Unfortunately, current green hydrogen production technologies are not yet capable of achieving reasonable efficiency and cost-effectiveness. Hydrogen produced from water, however, remains the most accessible resource [6, 7] and has the potential to compete with blue and grey hydrogen production methods. Therefore, if enough energy is applied, a water molecule can be broken into hydrogen and oxygen. The water-splitting process can be carried out using various technologies. Hydrogen can be extracted from water using electricity (electrolysis), photon energy (photolysis), or heat energy (thermolysis). Of interest is the production of hydrogen using solar water splitting, also known as the solar hydrogen process which can be divided into two main systems: (1) photoelectrochemical water splitting process and (2) photocatalytic water splitting process.

Photocatalysis refers to the process of converting photon energy into chemical energy, performed by a catalyst capable of absorbing light, a photocatalyst. This photon energy is used to speed up reaction kinetics or promote non-spontaneous reactions without the need for an external energy source. Main photocatalytic methods to produce hydrogen by water splitting involve the use of nanomaterials [8, 9]. Titanium dioxide [10-12], graphitic carbon nitride (g-C_3N_4) [13-15] and cadmium sulfide (CdS) [16, 17] have become some of the most widely studied photocatalysts for green hydrogen production in recent decades. Among them, TiO_2 stands out as most advanced and reference photocatalyst due to its photostability, high efficiency, suitable band gap, biocompatibility, and non-toxicity [18].

Despite the substantial amount of research devoted to this topic, there is still room for new discoveries. The rational design of a photocatalyst requires a detailed understanding of the relationship between structure and activity, which makes it possible to improve its catalytic performance and avoid rapid degradation.

1.2 TiO_2 as a photocatalyst

TiO_2 is a material of significant interest in scientific research due to its unique and advantageous properties, which make it highly suitable for a wide range of applications. The reasons for the widespread studies of TiO_2 include: (i) abundancy of TiO_2 in nature and relatively low production cost, which makes it an economically viable option for large-scale applications, (ii) high chemical stability: TiO_2 is resistant to corrosion, and does not degrade easily under environmental conditions, ensuring long-term performance and durability, (iii) TiO_2 is generally considered non-toxic and environmentally friendly, making it safe for use in consumer products, including sunscreens and food additives, (iv) TiO_2 exists in several different polymorphs, which all behave differently, they can be easily modified to enhance its properties for specific applications. The most common of these are rutile, brookite and anatase (***Figure 3***).

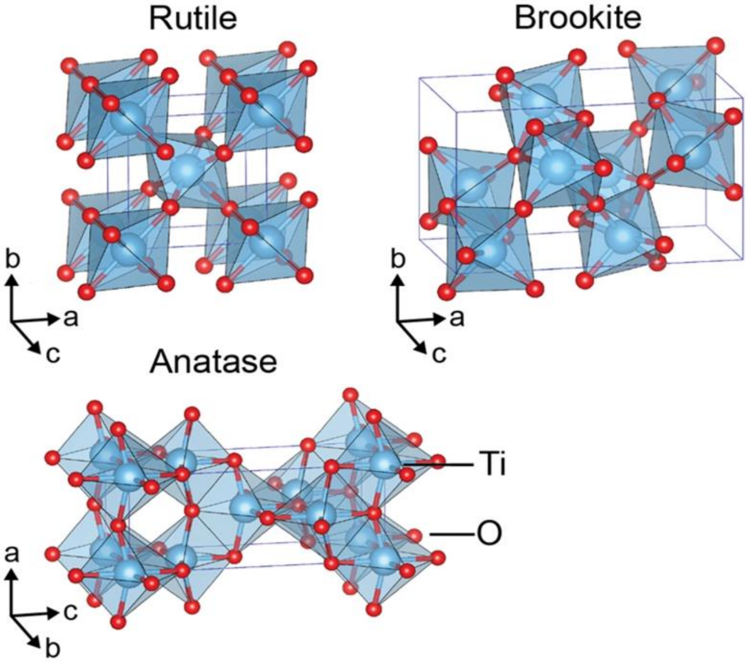

Figure 3. Phase structure of the titania polymorph. Adapted from [10].

Since A. Fujishima and K. Honda discovered the splitting of water by sunlight using TiO_2, opening a completely new chapter in solar energy conversion [19], many works have been devoted to improving this system. To define the strategy for improving titanium dioxide photocatalyst, it is necessary to go deeper in understanding of water splitting process. In photogenerated catalysis, photocatalytic activity depends on the ability of the catalyst to create electron-hole pairs that generate free radicals capable of undergoing secondary reactions.

Figure 4 shows a schematic illustration of the main steps involved in the photocatalytic water splitting process. At the first step, electron–hole pairs are generated. During the photocatalytic process, irradiation with ultraviolet (UV) light activates the photocatalyst, creating a redox environment in an aqueous solution. The semiconductor photocatalyst absorbs incident photons with energies equal to or greater than its bandgap. Each photon of the required energy that hits an electron in the occupied valence band of a semiconductor can excite that electron to an unoccupied conduction band. This results in the excited-state conduction band electrons and holes in the positive valence band.

The second step consists of charge separation and migration of photogenerated electron–hole pairs. Ideally, all electrons and holes should reach the surface without recombination to maximize the efficiency of the photocatalyst. This process can be summarized as:

$$\mathrm{TiO_2} \xrightarrow{h\nu \geq E_g} h_{VB}^{+} + e_{CB}^{-} \qquad (1)$$

In the last step, electrons that move to the surface of the catalyst participate in the reduction reaction and generate hydrogen, and holes diffuse from the valence band to the surface of the photocatalyst, which participates in the oxidation reaction to form oxygen.

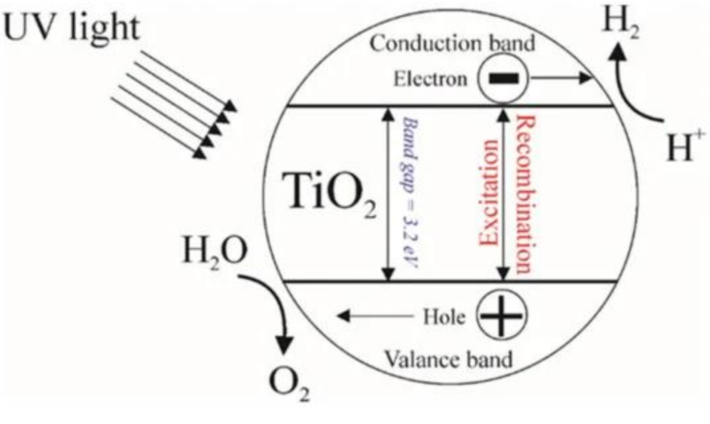

Figure 4. Schematic illustration of the main photocatalytic steps of a TiO_2 photocatalyst. Adapted from [20].

Redox reactions on the surface of the photocatalyst are described by the following equations:

Oxidation: $\mathrm{H_2O} + 2h^+ \rightarrow 2\mathrm{H}+ + \frac{1}{2}\mathrm{O_2}$ (2)

Reduction: $2\mathrm{H}^+ + 2e^- \rightarrow \mathrm{H_2}$ (3)

Overall reaction: $\mathrm{H_2O} + E\ (\sim 1.23\ \mathrm{eV}) \rightarrow \mathrm{H_2} + \frac{1}{2}\mathrm{O_2}$ (4)

The redox properties of a photoexcited semiconductor depend predominantly on the energy positions of the highest energy state of the valence band and the lowest energy state of the conduction band. Currently, the efficiency of energy conversion from solar to hydrogen by photocatalytic splitting of water into TiO_2 is still unsatisfactorily low, mainly due to the following reasons:

(1) Recombination of photogenerated electron–hole pairs: Conduction band electrons can very quickly recombine with valence band holes and release energy in the form of unproductive heat or photons.

$$h_{VB}^{+} + e_{CB}^{-} \xrightarrow{recombination} Energy \tag{5}$$

(2) Fast reverse reaction: The decomposition of water into hydrogen and oxygen is an energy-increasing process, so the reverse reaction (recombination of hydrogen and oxygen into water) occurs easily.

(3) Inability to use visible light: To make water splitting happen the conduction band needs to be more negative than the energy required to produce hydrogen (0.00 *E* vs. NHE) and the valence band must be more positive than the energy required to produce oxygen (1.23 *E* vs. NHE) (***Figure 5***). The minimum energy needed for water splitting is 1.23 eV, corresponding to absorbing light with a wavelength of 1010 nm, covering almost 70% of the sunlight spectrum. However, because of energy losses in the process, the ideal energy band gap is around 2.0-2.2 eV. The problem with TiO_2 is that its band gap is too large (3.2 eV), meaning it can only absorb UV light, which makes up just 4% of sunlight.

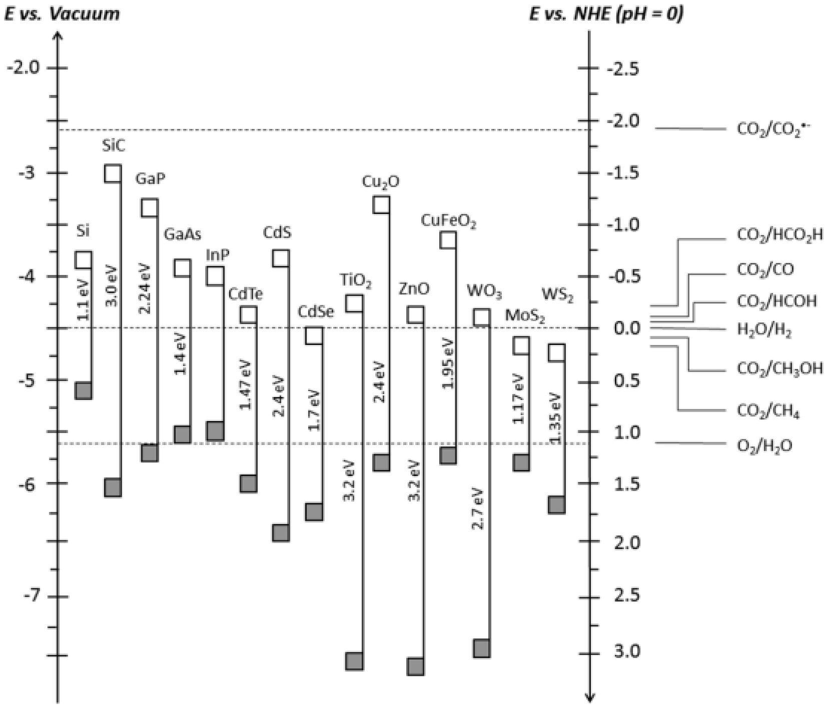

Figure 5. Band diagrams for various semiconductors with respect to vacuum scale and normal hydrogen electrode (NHE). Adapted from [21].

Similarly, for H_2 production from water, numerous studies have concluded that directly splitting water into H_2 and O_2 has very low efficiency due to the rapid reverse reaction. A much higher hydrogen production rate can be obtained by the addition of the so-called "sacrificial reagents," such as alcohols and other organics [22-25]. Hole scavengers play a critical role in photocatalytic hydrogen production by preventing electron-hole recombination, a major factor that limits the efficiency of photocatalytic systems. By capturing photogenerated holes, scavengers facilitate effective charge separation, ensuring that the photogenerated electrons are available for the hydrogen evolution reaction. This process not only enhances the overall efficiency of the system but also influences the reaction pathways, selectivity, and product distribution.

Methanol and formic acid are widely used as hole scavengers in photocatalytic hydrogen production, each offering distinct advantages. Methanol, known for its reactivity with hydroxyl radicals ($HO^{\cdot}$), generates hydroxymethyl radicals ($^{\cdot}CH_2OH$), which contribute to further reductive reactions [26]. Its oxidation progresses through intermediates such as formaldehyde and formic acid before ultimately converting to CO_2. Methanol's dual role as a hole scavenger and substrate enhances its effectiveness in photocatalytic systems, although its industrial production is not environmentally sustainable, raising concerns about its application in green technologies [27]. Formic acid, on the other hand, is highly efficient due to its ability to form inner-sphere complexes with Ti atoms, promoting charge transfer and effective hole trapping. It lowers the pH of the reaction medium, creating favorable conditions for electron transfer to the conduction band and improving overall photocatalytic efficiency. However, formic acid reduces the formation of $HO^{\cdot}$ radicals by competing with water molecules for holes, which may limit certain oxidation pathways. Despite its efficiency, formic acid is less selective, interacting with both holes and radicals.

The choice of an appropriate hole scavenger, therefore, is pivotal for optimizing photocatalytic performance and achieving high hydrogen production rates. However, to consider photoreforming a true green technology, the organic compounds used as sacrificial agents should be wastes or they should be produced through CO_2 neutral processes.

Attention should be drawn to the fact that this work does not address the direct production of hydrogen from water. Instead, the focus is on studying the hydrogen evolution reaction in the presence of suitable hole scavengers.

1.3 Effect of TiO_2 morphology on photoactivity

The morphology of titanium dioxide plays a crucial role in altering its properties and, consequently, its efficiency in photocatalytic reactions.

Numerous TiO_2 morphologies have been developed and investigated to enhance its photocatalytic performance [28-30]. However, it is important to begin with simpler forms to better understand how morphological variations can influence catalytic activity.

Anatase TiO_2 is the most used polymorph specifically for photocatalytic water splitting. The production of hydrogen on anatase TiO_2 is characterized by a noticeable dependence on the ratio between the (101) and (001) surfaces of TiO_2 nanoparticles [31]. Higher hydrogen evolution rates were observed with the increasing presence of (101) planes due to their reducing nature [32, 33].

Interestingly, interfaces between rutile and anatase were believed to improve photocatalytic activity by facilitating charge carrier separation [34], and as a result, biphasic titanium dioxide was often considered to have improved functionality as a photocatalyst. The electronic difference between the anatase and rutile phase originates from the different locations of the conduction band, which are predominantly formed by the unoccupied 3d orbitals of titanium. However, for anatase, the CB is cathodically shifted by 0.2 eV with respect to the rutile's one that instead almost coincides with the NHE potential. This gives anatase a higher redox driving force for water splitting reaction with respect to the rutile. The valence band on the other hand is mainly generated by the 2*p* orbitals of oxygen, and for both structures is located at ~3 eV [35].

Thus, the combination of TiO_2 polymorphs allows one to achieve exceptionally high photocatalytic activity in pure titanium dioxide structures. This strategy is used in commercial Degussa/Evonik P25 system which shows great photoactivity results in hydrogen production [36]. P25 combining two TiO_2 polymorphs and consists of 80% anatase and 20% rutile. However, P25 remains unsuitable for use in the visible light spectrum, as its bandgap for various crystalline phases of TiO_2 is located in the UV region. (P25 – 3.25 eV, anatase – 3.2 eV, rutile – 3.0 eV and brookite – 3.3 eV) [37].

1.4 TiO_2 modifications

Various strategies for tuning the bandgap and regulating the electronic properties of TiO_2 have been reported. Tuning of the shape and size of TiO_2 nanostructures like nanorods or nanosheets further enhances the surface area and charge carrier dynamics, boosting overall photocatalytic performance. Additionally, defect engineering, through the introduction of oxygen vacancies or Ti^{3+} states, enhances electron transport, light absorption, and charge separation, further increasing catalytic activity [37].

However, improving TiO_2 alone is insufficient for achieving efficient water splitting at a scale suitable for industrial applications. To overcome these limitations, multiphase materials have been developed by integrating TiO_2 with other elements, including organic compounds, inorganic materials, or metals. These strategies include doping with non-metals and metals, coupling TiO_2 with other semiconductors, and incorporating metal nanoparticles [18, 38-41]. Each approach is designed to enhance TiO_2 photocatalytic efficiency by modifying its light absorption characteristics and optimizing charge carrier dynamics.

Among the various non-metallic dopants [42-44], carbon, nitrogen, and fluorine have garnered significant interest. Studies have shown that the band gaps of these doped systems are narrower compared to undoped TiO_2 [45-48]. These dopants not only increase light absorption but also extend the optical absorption range into the visible light region. The improvement in visible light photocatalytic activity is attributed to enhanced electron transfer, higher charge carrier density, extended electron lifetime, and increased diffusion coefficients. However, some investigations on non-metallic dopants have reported limited effects on band edge positions [49] or, despite improved optical absorption, the photocatalytic system was ineffective for water splitting.

It has been found that among all possible modifications, combination of noble metals with TiO_2 can improve electron transport between the valence band and the conduction band near the Fermi level [50]. Diverse approaches have been implemented for the synthesis of supported TiO_2 noble metal nanoparticles with their advantages and disadvantages [51]. One of the most frequently used is impregnation. In this technique, a metal precursor is deposited onto the support's surface, followed by calcination and/or reduction. In contrast, alternative methods for preparing supported metal catalysts include colloidal precipitation methods, which allows for better control of the size and shape of metal particles, since in impregnation methods, agglomeration often occurs during drying, high-temperature calcination, and reduction. Colloidal deposition methods consist of three preparation steps: (1) reduction of metal ions to metal nanoparticles in the presence of protecting polymers, (2) deposition of metal nanoparticles on TiO_2 support, followed by (3) oxidative decomposition of polymers and reduction of metal nanoparticles [52]. However, a drawback of this method is that surfactants or organic ligands, used as stabilizing agents to prevent the agglomeration of noble metal nanoparticles, tend to adsorb onto the active sites and are difficult to remove, leading to a loss of catalytic activity.

However, as demonstrated in the literature [53-55], the most used techniques for synthesizing supported metal NPs for hydrogen production are:

Deposition-Precipitation Method: This approach involves the gradual addition of a metal acid precursor to a basic slurry containing the support material. The metal precipitates out as a metal oxide or hydroxide. A subsequent reduction step is necessary to convert the precipitate into its metallic state. The weakness of this method is the lack of control over metal distribution and surface composition.

Photochemical Deposition Method: This method has green nature and convenience, but also it has the potential in to adjusting chemical states, morphology, interface, etc. The metal nanoparticles are formed by irradiating an aqueous solution containing a sacrificial agent (the photocatalyst powder, metal precursor or an electron donor molecule). The metal ions in solution are reduced by electrons generated through UV excitation of the semiconductor. Meanwhile, the holes oxidize the sacrificial agent, releasing additional electrons that further facilitate metal reduction. No additional thermal treatment is needed as the metal nanoparticles are already in their metallic state, though washing steps may be required to remove any organic residues.

The deposition of metal nanoparticles onto the TiO_2 substrate forms a Schottky junction, which leads to an intimate interface contact. These materials have shown better activity towards the photocatalytic hydrogen production [56-61]. Metal co-catalysts directly affect the electronic characteristics of the TiO_2 surface. When metal NPs are coupled with TiO_2 semiconductors the electron-hole separation efficiency can be improved, leading to absorption in the visible range and even into the near-infrared region. In this case, the incorporated metal serves as an electron trap, capturing electrons from the CB of TiO_2 (***Figure 6***).

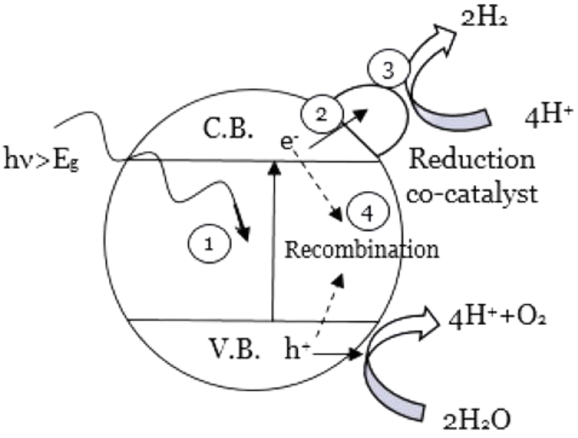

Figure 6. Schematic illustration of the main photocatalytic steps of a supported metal on TiO_2 photocatalyst. (1) light absorption and charge excitation from valence band to conduction band, (2) transfer of the photo-generated electrons and holes to the catalyst surface, (3) surface redox reactions, and (4) charge recombination. Adapted from [62].

Given the shortage and high cost of noble metals, it is critical to improve the performance of supported noble metal nanoparticles. Tuning the size of noble metal nanoparticles has been proven to be a highly effective strategy, significantly improving the catalyst's performance. If the particle size decreases, we increase the active surface and modulate the work function, band gap, surface oxidation states, and other electronic states [21]. The particle size affects the catalytic activity, and in general, increasing the particle size would result in decreasing the reaction rate. But in practice it is more complicated. Al-Azri et. al [63] systematically explored the effect of metal particle size and the metal loading on the photocatalytic activity of TiO_2 (with M = Pd, Pt, Au) for H_2 production in ethanol–water mixtures. Photocatalysts with metal loadings of 0–4 wt. % were synthesized by the deposition–precipitation method using the conventional Degussa P25. They showed that, unlike the case of a thermal catalytic reaction, larger particles perform better than smaller ones in photoproduction of hydrogen. However, such conflicting results may also indicate the formation of a metal-support interaction effect for smaller particles, which prevents photocatalytic reaction.

It has been demonstrated that the catalytic properties of the heterogeneous catalysts can be tuned using a great variety of metal–support interaction (MSI) types. Typical phenomena associated with metal supports include charge transfer, interfacial perimeter effects, nanoparticle morphology, and strong metal-support interactions (SMSI) (***Figure 7***).

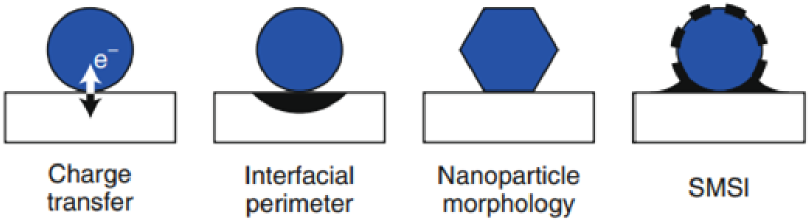

Figure 7. Schematic representation of five main metal-support interactions. Adapted from [64].

Incorporating metal ions into the support TiO_2 causes the changes in the electronic state of the guest metal [65]. The stored electrons on the metal particles can then be transferred to protons adsorbed on the surface and further reduce the protons to hydrogen molecules. The promoted by noble metals electron transfer results in higher photocatalytic activity.

The shape and crystal structure of nanoparticles significantly impact their catalytic performance, as different shapes expose specific facets with either favorable or unfavorable atomic configurations. The adhesion energy at the metal-support interface affects the shape of the nanoparticles. In the case of platinum and palladium, the round shape is usually considered the most suitable for hydrogen production. In the work [66], Pt polyhedral and spherical NPs were synthesized on TiO_2. It was proved that spherical shape NPs were more efficient for photocatalytic hydrogen production, what was attributed to the electron transfer capabilities of the different exposed crystallographic planes of spherical and cubic (polyhedral) nanoparticles. It was also proven that cubes NPs contain dominant (001), (010), (100) facets, the electron transfer is inhibited compared to the spherical particles that contained a high amount of high indexed facets, which facilitates the electron transfer.

This result was also found in the case Pd [67]. It was demonstrated that by adjusting the geometry of Pd nanoparticles several major photocatalytic activity-related aspects can change. Cubic and round nanoparticles on different polymorphs (anatase, rutile, P25) of titanium dioxide were synthesized with similar size distribution. Also here, spherical shape Pd NPs showed better activity in photocatalytic hydrogen production. It was also shown that the band gap was smaller for all samples with palladium nanoparticles compared to pure titanium dioxide, while for spherical nanoparticles that showed better activity, a smaller band gap was not always observed.

Among other interactions between metal particles and reducible metal oxide supports the SMSI is a phenomenon of significant interest in the modern heterogeneous catalysis research [64], drawing attention due to its potential to fine-tune the catalytic properties and stabilization of metal particles on supports. Understanding the parameters that govern SMSI and its impact on the properties of supported metals is crucial for developing new strategies for tailoring the catalyst properties through variations in the synthetic and/or pre-treatment procedure [68]. The SMSI effect was first emphasized by Schwab [69] and then by Tauster et al. for noble metals supported on TiO_2 [70]. The proposed explanations of the SMSI phenomenon include a charge transfer, as first proposed by Tauster, and an encapsulation of metal particles by the support, which acts as a site blocker[71, 72]. Early studies by Bracey, Logan, Datey and Liu have already demonstrated that a thin layer of TiO_x can be formed around the metal NPs, blocking the interaction of gas molecules with their surfaces [73-76]. This model has been also suggested in more recent studies using high-resolution electron microscopy [77-80].

In the last decade, SMSI effect has been actively exploited for the optimization of catalytic performance and stability of materials in different (photo)catalytic reactions, including hydrogenations, oxidations and green hydrogen production.

2 *In s*itu *and operando* characterization techniques in photocatalysis

The ambition to improve catalytic systems through rational design, where we clearly understand the relationship between the structure and function of our systems to predict their properties, remains a shared goal among researchers. Understanding how catalyst structure influences reactivity and selectivity continues to be a major challenge in modern heterogeneous catalysis. The development of advanced characterization techniques has greatly enhanced our understanding of the relationship between catalyst structure and performance. However, obtaining this information requires studying catalysts under realistic operating conditions, such as temperature, pressure, and the composition of surrounding gases or liquids, to accurately capture their behavior and responses to these conditions.

This type of research is referred to as *in situ* characterization, which has been used for over 60 years. Derived from Latin, meaning "on-site," it refers to the application of controlled environments for the study of systems. However, while *in situ* studies provide valuable structural information, they often lack insights into reaction products, which are crucial for evaluating catalyst performance.

Unlike *in situ* methods, which examine the catalyst structure without it being actively involved in a reaction, *operando* techniques offer more comprehensive tools by simultaneously studying both the catalyst's properties and its direct impact on catalytic activity. This approach offers a more complete understanding of reaction mechanisms. In contrast to *in situ*, the term "*operando*" (Latin for "working") is relatively recent, first used about 20 years ago [81, 82]. *Operando* methodology enables the study of catalysts under actual working conditions, providing simultaneous insights into both their structure and performance during reactions.

Traditional methods often attempt to correlate catalyst's structure with observed photocatalytic behavior. In some studies, catalysts were synthesized *in situ* and subsequently subjected to catalytic reaction conditions [83]. The complexity of photocatalytic reactions due to multiple electron/hole transfers on various space-time scales presents a challenge. Nonetheless, with the advancement of *in situ* and *operando* characterization methods that monitor photocatalysts under real or near-real conditions, our understanding of photoresponsive material design and photocatalytic processes has improved significantly.

There are numerous advanced *in situ* and *operando* characterization methods available to study fundamental issues in heterogeneous photocatalysis. These techniques provide critical information on morphology and structural changes, charge transport and distribution, as well as the detection of surface species and reaction intermediates during photocatalytic reactions. Spectroscopies, in particular, stand out as an indispensable and powerful tools for addressing these questions [84].

As noted in a recent review titled "Introduction: *Operando* and *in situ* studies in catalysis and electrocatalysis" [85], the experimental maturity in physical chemistry sciences underscores a fundamental truth: to have a deep understanding of the catalyst's morphology, structure, and surface/bulk composition and their intricate interplay with reacting molecules and reaction conditions we desperately need a synergistic combination of spectroscopy, diffraction and microscopy technics. Combining multiple techniques provides a possibility to look at catalytic systems from different perspectives by getting complementary information.

Although all mentioned methods have greatly advanced photocatalysis research, they still require significant improvement. This is partly due to the fact that two general strategies can be used in photocatalytic reactions [86]. The first one involves dispersing or suspending the photocatalyst in a solution, which is believed to result in a better mass transfer. However, the distribution of light from the external source through the volume of such reactors is typically inhomogeneous. An alternative approach uses an immobilized catalyst, typically deposited on a UV-transparent window, which can be easily illuminated in a constant manner. For spectroscopic studies, an approach when the catalyst is deposited on a window of an *in situ/operando* cell is more often exploited [84, 87].

In practice, it implies the design of customized experimental setups for each specific system under the study. This requires not only a comprehensive literature review of relevant research but also creativity and ingenuity from researchers to overcome the inherent limitations of various characterization methods. Furthermore, despite the common assumption that many methods do not change or affect the samples properties and behavior, as we will see, this is not always the case. This issue is particularly pronounced in photocatalysis, where many methods involve irradiation to collect data. Therefore, it is crucial to carefully select appropriate characterization methods for photocatalysts, interpret data with caution, and avoid relying entirely on the results of a single method.

In the following sections, I will focus on three key methods: *in situ* and *operando* XAS, *in situ* FTIR, and *in situ* TEM, since in the course of my thesis research, these techniques required a non-trivial approach and the development of specialized experimental setups. I will begin with a brief introduction to X-ray absorption spectroscopy, as one of the central methods employed in my research. Additionally, I will address some of the limitations and challenges associated with applying all used techniques to the study of photocatalytic systems.

2.1 *In situ* and *operando* X-ray absorption spectroscopy

X-ray absorption spectroscopy (XAS) has become one of the standard tools in heterogenous catalysis, despite the need of using synchrotron radiation either to detect typically low-concentrated metal species or to follow fast photocatalytic processes [88-91]. XAS selectively probes the local structure around a specific element, which can be used for active site monitoring and to reveal structural properties of metal species of the photocatalysts during synthesis and under reaction conditions. [92, 93]. XAS exploits the interaction of matter with photons with energies in the X-ray range selected according to the binding energy of the core electrons in the atoms (typically metals), whose local environment is of interest. In this energy range, incident radiation is absorbed due to the photoelectric effect (***Figure 8***). If the incident X-ray photon has an energy equal to the binding energy of the core-level electron, a sharp increase in absorption occurs. This 'jump' is called the absorption edge or edge jump, and it corresponds to the transition of an electron from the core level to unoccupied electronic states in the material.

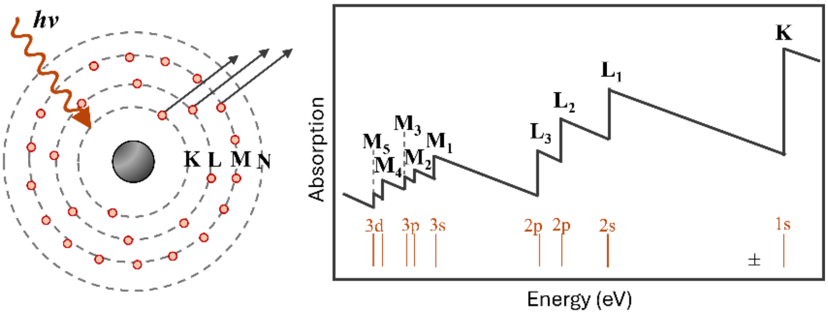

Figure 8. The photoelectric effect, in which an x-ray is absorbed, and a core level electron is promoted out of the atom and the absorption cross-section.

The X-ray absorption spectrum is obtained by measuring the dependence of the absorption coefficient μ above the absorption edge of the core-level electron energy for a known type of atom. Absorption coefficient μ shows the probability of X-rays being absorbed in accordance with Bouguer-Lambert-Beer's law [94, 95]:

$$I_1 = I_0 e^{-\mu d} \tag{6}$$

where I_0 is the intensity of the incident X-ray radiation before the sample, d is the thickness of the sample, I_1 is the intensity of the beam passing through the sample, μ is a smooth function of energy with a value that depends on the sample density ρ, atomic number Z, atomic mass M and X-ray energy E:

$$\mu \approx \frac{\rho Z^4}{M E^3} \tag{7}$$

In XAS, the dependence of the absorption coefficient μ(E) can be measured in transmission or fluorescence geometries (***Figure 9***).

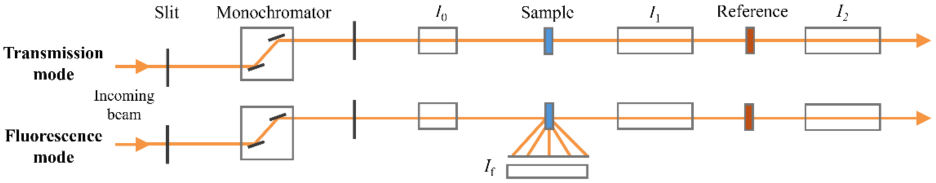

Figure 9. Geometry configuration for XAS measurements transmission fluorescence.

Figure 10 shows the typical energy dependence of the absorption coefficient (after normalization) on the energy of incident photons. The XAS spectrum is usually divided into two parts: X-ray absorption near-edge structure (XANES), which is usually around 50 – 100 eV beyond the edge, and extended X-ray absorption fine structure (EXAFS). XANES is sensitive to the formal oxidation number and coordination environment (e.g., point symmetry and types of ligands) of the absorbing atom, while EXAFS is used to determine the distances, coordination numbers, and types of neighbors of the absorbing atom.

The analysis of XANES spectra is usually carried out using the fingerprint method, however, in some cases semi-quantitative approaches, such as Natoli’s rule, existed [96-98]. Quantitative analysis of XANES spectra still remains a non-trivial task requiring ab initio modelling of spectra, which was powered by machine learning methods in the recent years [99-101]. In the case of EXAFS, the methodology for analyzing the spectra is well known. In the EXAFS region, modulation of the absorption coefficient is observed above the absorption edge, due to the scattering of a photoelectron on neighboring atoms with subsequent interference.

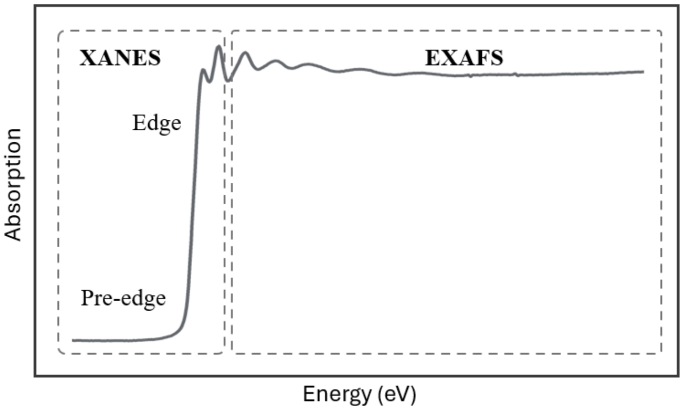

Figure 10. An example of XAS spectrum divided into XANES and EXAFS regions.

We can describe the oscillations in the EXAFS region as a function of the photoelectron wave number:

$$\chi(k) = \sum_{i}^{\infty} \frac{N_i f_i(k) e^{-2k^2\sigma^2} \sin[2kR_i + \delta_i(k)]\, S_0^2}{kR_i^2} \tag{8}$$

where N_i is the coordination number, R_i is the interatomic distance, S_0^2 is the spectroscopic factor describing the reduction in amplitude due to inelastic processes, σ^2 is the Debye-Waller parameter, $f_i(k)$ is the scattering amplitude and $\delta_i(k)$ is the scattering phase, i is the number of the coordination sphere. The use of fitting approach makes it possible to unambiguously extract the abovementioned structural parameters from the experimental data.

Since each atom has electrons at the nuclear level with clearly defined energies, it is possible to select the element to study by tuning the X-ray energy to the appropriate absorption edge, which accounts for one of the main advantages of the XAFS method - its elemental selectivity. But XAS requires certain sample preparation to meet the following conditions for sample thickness.

1. The total absorption, *μd,* of the system/sample should not exceed 2.5, otherwise the number transmitted photons will be simply not enough to accumulate the necessary statistics.
2. The change in absorption coefficient immediately before and after the absorption edge, should be close to 1 (as called absorption jump).

These two conditions are not always fulfilled simultaneously. For example, the total absorption may be unacceptably large, due to absorption by other elements in the material, or the thickness of the sample can be insufficient, which is a common issue in *in situ* and *operando* XAS studies in heterogeneous catalysis.

This complexity increases for *in situ* and *operando* spectroscopy studies in photocatalysis, where several factors impose additional constraints on experimental setups. In photocatalysts, the concentration of active metallic species is typically lower relative to the substrate, and the photocatalytic processes often take place in the presence of a liquid phase, which strongly absorbs X-ray photons. All this makes fluorescence geometry the only possible alternative in most cases. Therefore, it requires more complicated designs of experimental cells, especially when multiple techniques are combined in one *in situ*/*operando* cells [102-104].

Combining multiple spectroscopic techniques in one experimental setup offers the possibility of observing catalytic systems from different perspectives that provide complementary information. Tinnemans et al. [105] revealed the possibilities of combining several operando techniques in one spectroscopic-reaction cell. Their work [106] was devoted to operando DRIFTS combined with HERFD–XANES and XES to study the mechanisms behind photothermal catalytic oxidation of CO over Pt/TiO_2. The methods turned out to be sensitive enough to uncover a change in the electronic structure of the Pt sites upon light illumination. In another work [107], the “design gap” was eliminated by using a reaction vessel, where the addition of reactants and their stirring and mixing were carried out, while XAS and UV–Vis spectra were recorded in a spatially separated measurement cell. Yoshida et al. [83] attempted an ex situ XAS and UV–Vis of Pt/TiO_2 at different times of photodeposition. Although the potential of combined operando UV–Vis and XAS under working conditions is huge [108-110], there are still only a few studies devoted to the mechanisms of the photodeposition process and the structure of photodeposited metal particles.

Furthermore, in *in situ/operando* XAS studies, it is generally expected that only chemically induced transformations will take place. However, in photocatalysis, where the reactions are driven by photoexcitation, an additional factor, the X-ray beam itself, must be considered [111].

2.2 *In situ* and *operando* Fourier transform IR spectroscopy

As discussed in Chapter 1, the surface of a catalyst plays a critical role in providing active sites what remain in a dynamic state throughout the reaction. Therefore, real-time dynamic characterization of photocatalyst surfaces is essential for understanding the underlying mechanisms of photocatalytic reactions. To date, Fourier transform infrared spectroscopy (FTIR) has been extensively applied in this field, using as a powerful tool for investigating these surface processes. Recently, the interpretation of experimental IR data has often been further facilitated by the parallel development of first-principles calculations that can estimate the interaction energies and vibrational frequencies of probe molecules adsorbed on different surface sites [112].

The combination of XAS and FTIR has demonstrated their effectiveness in the study of photocatalysts [106, 113-115]. Drawing on the experience of other researchers, IR spectroscopy was selected as a central complementary technique in this work. IR spectroscopy not only enables relatively fast and accessible data acquisition under laboratory conditions but also offers additional insights into surface interactions. While XAS, utilizing hard X-rays, is a bulk-sensitive technique due to its ability to penetrate deep into the sample, IR spectroscopy provides information primarily about the sample's surface. The combination of XAS, offering a comprehensive understanding of the entire sample, and IR spectroscopy, which focuses on surface interactions, is therefore crucial for obtaining a complete structural understanding of the photocatalysts under study.

Various detection modes are available for infrared spectroscopy, including transmission, diffuse reflectance (DRIFTS), and attenuated total reflectance (ATR) (***Figure 11***).

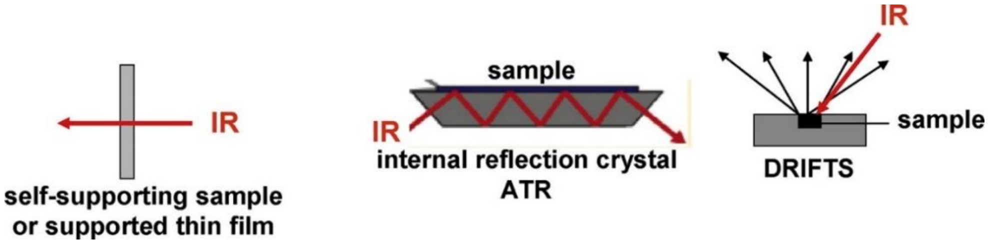

Figure 11. Basic schemes of the three IR techniques used in thermal catalysis and photocatalysis. Adopted from [116].

In situ DRIFTS offers significant advantages in terms of operability and accuracy, particularly for gas/solid-phase reactions [117-120], and its compatibility with irradiation makes it widely used for photocatalytic studies. Nevertheless, DRIFT has limitation, it cannot be measured in solid/liquid photocatalytic reaction systems, even though the majority of photocatalytic reactions occur in aqueous environment. Moreover, in the case of DRIFTS for photocatalysis studies, achieving full irradiation of the sample by excitation photons is challenging, which presents a disadvantage. The IR spectra capture signals from both irradiated and unirradiated particles, complicating the interpretation of the effects of excitation photons.

Oppositely, in photocatalysis for transmission IR spectroscopy measurement usually samples prepared as thin, self-supporting pellets or deposited on Si wafers what allows to have really thin layer of catalyst to be completely penetrated by the UV radiation [121, 122]. This approach often eliminates the need for additional experimental setups and is compatible with conventional IR transmission cells. However, as in the case of DRIFTS, it is limited by its inability to facilitate measurements in the liquid phase. But transmission IR spectroscopy still has advantages, it makes it easier to identify weak transitions compared to other modes. This technique is sensitive to weak transitions, as more light is transmitted than absorbed. When normalizing spectral intensities in other methods, weak signals are often overshadowed by stronger absorption lines, but the transmission mode allows for a clearer observation of these weaker transitions.

ATR is particularly well-suited for probing solid-liquid interfaces, as the limited penetration depth of the evanescent wave allows for the study of liquids with high attenuation coefficients, such as water. In the study [87], an innovative *in situ* liquid-phase ATR-FTIR under aqueous conditions was used. The setup allowed real-time monitoring of growth of Pt NPs during photodeposition and their evolution during photocatalytic methanol oxidation. This versatile setup offers new insights into reaction mechanisms and catalyst behavior in near-application environments, advancing photocatalysis research. Another study [123] also utilized a flow-through ATR-IR spectroscopy setup to investigate the photocatalytic mineralization of malonic and succinic acids over P25 TiO_2 *in situ*, highlighting its capability to monitor real-time changes on the catalyst surface. The experimental setup, enhanced by modulation excitation spectroscopy and isotope labeling, enabled detection of CO_2 and intermediates, revealing the mineralization pathways. Although, many successful examples, as in the case of XAS spectroscopy, this approach requires the development of dedicated liquid cells, and to date, only homemade devices have been employed.

The primary interest in IR spectroscopy for photocatalysis arises from its ability to study the system under irradiation. IR spectroscopy can give detailed information about how different molecules on the surface of a photocatalyst change over time UV during radiation. In this way, it is possible to monitor the accumulation of intermediates and reaction products and to derive kinetic laws expressed in terms of surface concentrations. However, IR also offers valuable information even in the absence of activating photons, as it can be used to investigate the structure of photocatalyst surfaces elucidating processes occurring in the dark.

As an example, *operando* FTIR spectroscopy was used to investigate TiO_2 and Pt/TiO_2 photocatalysts for CO_2 photoreduction, identifying carboxylates as key intermediates in surface reactions [124]. This approach clarifies reaction pathways, aiding in understanding the photocatalyst surface behavior under real conditions and paving the way for more detailed future kinetic studies. In another study devoted to a new *BEA-Ti photocatalyst, combining *BEA zeolite with TiO_2, was studied for gas-phase methanol oxidation [125]. A new operando setup has been made to study the photooxidation process. Time-resolved IR spectroscopy, paired with mass spectrometry, provided quantitative insights into surface reactions and key factors influencing reactivity and selectivity, underscoring operando-IR’s effectiveness in studying heterogeneous photocatalysis and potential applications in air purification.

IR is commonly used to identify the oxidation states of metal sites by tracking the vibrational frequencies of probe molecules, as well as to determine the type of metal surface and the geometries of adsorbed species. The use of CO probe molecules in combination with FTIR spectroscopy can monitor the probe-surface interaction with sufficient sensitivity. The interaction between CO and transition metals usually involves electron exchanges between them. The CO molecule has an electron pair in the 5σ orbital. This pair can be donated to the transition metals, forming a bond. At the same time the metal has electrons in its d orbitals that can be sent back into an empty orbital of the CO molecule, specifically the 2π* antibonding orbital. When CO donates electrons to the metal and receives electrons back from the metal, the C-O bond becomes weaker. This is because the back-donation into the 2π* antibonding orbital disrupts the C-O bond more. As more electrons are back-donated into the 2π* antibonding orbital, the bond between carbon and oxygen weakens further, leading to a lower C-O stretching frequency.

The amount of back-donation, or how much the metal sends electrons back into the CO molecule, depends on how many metal atoms the CO is attached to. This connection affects the CO molecule's vibrational frequency. In the case of palladium and platinum when CO molecule is attached to just one metal atom, it is expected to show a specific vibrational frequency in the range of 2130-2000 cm^{-1}. When the CO molecule is connected to two metal atoms (forming a bridge), its vibrational frequency drops to between 2000-1880 cm^{-1}, while in the case of bonding with three metal atoms, the vibrational frequency lowers even further, to below 1880 cm^{-1}. These three positions are referred to in the literature as linear, bridge, and hollow, as shown in ***Figure 12***.

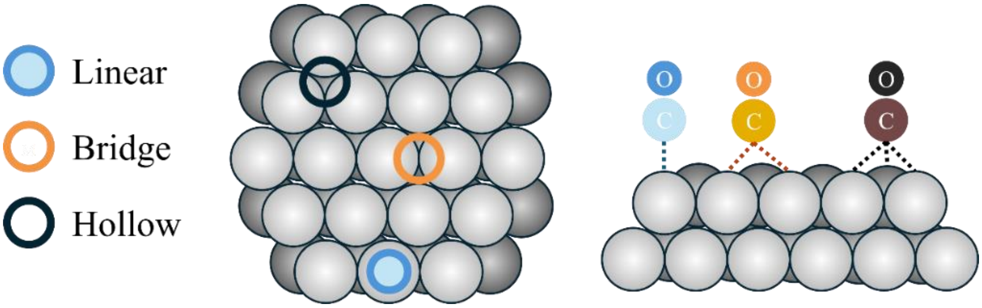

Figure 12. Schematic illustration of geometry of CO adsorption on metals (grey circles).

Thus, *in situ* IR spectroscopy is capable of distinguishing between various geometric distortions of the adsorbed molecule. However, the literature also highlights that CO molecules, which on the one hand are commonly used as probe molecules, on the other hand can arise as intermediate reaction products and have an irreversible effect on the sample. This underscores the necessity of employing *in situ* characterization techniques that minimize the impact of the method itself on the sample, ensuring a more accurate interpretation of the data [126].

2.3 *In situ* electron microscopy

Another technique that plays a big role in photocatalysis study is electron microscopy. In fact, it is now quite difficult to find any study of heterogeneous catalysts that does not include at least one SEM or TEM image. The high spatial resolution of TEM allows for a detailed examination of the correlation between the structural characteristics of nanoparticles and their photocatalytic performance. Electron microscopy also plays a crucial role in identifying defects, lattice fringes, and interfaces between the metal and oxide support, thereby offering valuable insights into atomic-level interaction mechanisms.

EM can be further equipped with additional analytical techniques such as energy-dispersive X-ray spectroscopy (EDS) and electron energy loss spectroscopy (EELS). EDS can identify the elemental composition of nanoparticles, confirming the presence and distribution of specific metals on support. EELS provides information on the electronic structure and oxidation states of the elements, which is essential for understanding the behavior of the systems under reaction conditions.

In situ EM allows for the real-time visualization of catalyst particles under actual reaction conditions, enabling an understanding of their structural and compositional responses to environmental changes [127]. This can provide an understanding of phase transition mechanisms and kinetics. Moreover, *in situ* TEM has been employed to observe dynamic behavior at the solid-liquid interface during heterogeneous reactions [128].

In recent years, *in situ* microscopy has gained even greater significance with the introduction of advanced heating holders that have replaced conventional ones. This type of *in situ* microscopy, referred to as environmental transmission electron microscopy (ETEM), enables investigations of dynamic changes in materials with atomic resolution while simultaneously applying reactive gas environments and heat. ETEM also facilitates real-time microscopic visualization of photocatalytic reactions, significantly advancing the study of photocatalysis [129]. However, due to the complexity of technology and the high cost of *in situ* ETEM, there are only a few studies on the application of ETEM during photocatalytic reactions.

Despite the widespread application of the above experimental methods, challenges in *in situ* photocatalytic studies using electron microscopy involve both technical and scientific issues. For example, a significant issue in studying the effects of visible light within an electron microscope is the difficulty in differentiating between the effects caused by visible light and those induced by the high-energy electron beam. Consequently, systematic investigations are required for each specific system under study [130].

3 Materials and Methods

3.1 Materials

3.1.1 The TiO_2 nanopowders

The preparation of TiO_2 nanosheets was carried out with a solvothermal method following an established literature procedure (see ***Figure 13***) [29]. In a typical synthesis 25 mL of $Ti(OBu)_4$ (Aldrich reagent grade 97%) was poured in a 150 mL Teflon lined stainless steel reactor and 3.5 mL of concentrated hydrofluoric acid (Aldrich reagent grade 47%) was added dropwise under stirring. The reactor was sealed and kept under stirring at 250 °C for 24 h. The resulting bluish paste was centrifuged and washed with acetone to remove the residual organics and then with water (Milli-Q). Finally, the obtained aqueous suspension was freeze-dried obtaining a bluish powder. The sample in this form is labeled as TiO_2 Nsh throughout the text.

The bipyramidal shape TiO_2 sample was synthesized by forced hydrolysis of an aqueous solution (see ***Figure 13***). The bipyramidal shape TiO_2 NPs were obtained by mixing titanium isopropoxide ($Ti[OCH(CH_3)_2]_4$) with triethanolamine ($N(CH_2CH_2OH)_3$, initial pH 10) at a molar ratio of 1 : 2 under dry air to form a compound of Ti^{4+} stable against hydrolysis at room temperature, followed by addition of doubly distilled water to make an aqueous stock solution of 0.50 mol dm^{-3} in Ti^{4+}. Then, 10 cm^3 of the stock solution was mixed with the same volume of doubly distilled water. The synthesis was carried out by hydrothermal treatment at 180 °C K for 90 h in an autoclave. At the end of the hydrothermal treatment the sample was calcined at 400 °C for 2 hours. Further details on the preparation of these NPs, hereafter referred to as TiO_2 Bipy, which show a bipyramidal shape, mainly limited by (101) facets, can be found in our previous publication [131].

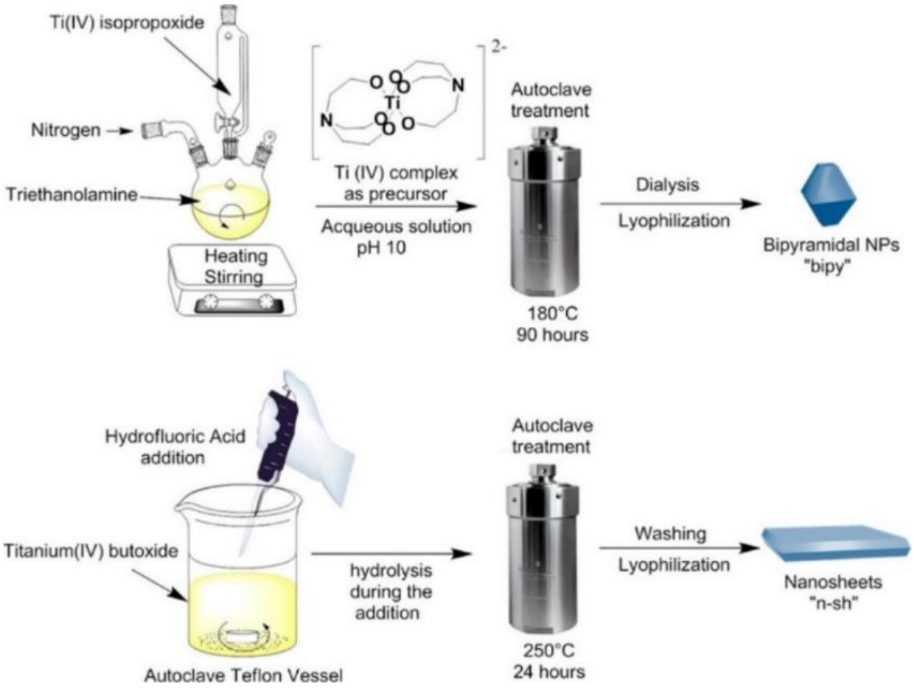

Figure 13. Synthesis of TiO_2 Nanosheets and TiO_2 Bipyramidal Nanoparticles. Adapted from [29].

TiO_2 P25 was provided by Evonik (formerly Degussa) (80% anatase and 20% rutile; purity 99.50 wt%).

3.1.2 Synthesis of metal nanoparticles supported on TiO_2

M/TiO_2 (M=Pt, Pd) samples were prepared using different morphology types of TiO_2 as a support described in previous section. The synthesis was carried out in magnetically stirred cylindrical quartz cell (***Figure 14***) with 4 cm inner diameter and 2.5 cm height. TiO_2 as a powder was suspended in ultrapure water (MilliQ) in the quartz cell through sonication for 10 minutes. Then the metal source was added to the slurry containing TiO_2.

- H_2PdCl_6 as Pd source (Sigma Aldrich, 1010 µg/mL Pd in 5 wt.% HCl),
- K_2PtCl_6 or H_2PtCl_6 as Pt source (Sigma Aldrich, 8 wt. % in H_2O),
- K_2PtCl_6 (Sigma Aldrich) as Pt source.

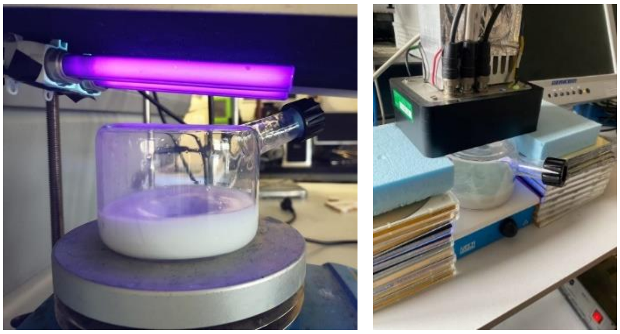

Figure 14. Synthesis set-up of quartz reactor for the photodeposition of metal nanoparticles on TiO_2 under UV led lamp.

Usually, the dependence of metal loading on hydrogen production has a bell-shaped form with a maximum of 1 wt.% or lover [132, 133]. However, it is crucial to note that the nominal loading during photodeposition cannot coincide with the real one. Therefore, 2% is the optimal solution, since it can simultaneously solve 2 problems: this loading is enough for good signal in XAS and FTIR measurements.

The metal photodeposition has been performed in the presence of 0.1 M formic acid as a hole scavenger. Formic acid proves advantageous as a hole scavenger for the photodeposition of Pt and Pd on TiO_2 due to its pH-adjusting capabilities and high reduction potential [134]. Studies show that at low pH values, the interaction between negatively charged Pt or Pd precursors and the positively charged TiO_2 surface enhances deposition rates due to favorable electrostatic interactions. Formic acid, with its acidic nature, ensures an environment conducive to efficient metal reduction. The photodeposition of Pt benefits from the high reduction potential of radicals formed in the presence of formic acid, favoring the nucleation of smaller, well-distributed nanoparticles instead of promoting particle growth. Moreover, acidic conditions provided by formic acid inhibit the formation of oxidized metal states like PtO_2, leading to a higher prevalence of metallic Pt(0), which is essential for catalytic activity.

Similarly, Pd photodeposition achieves optimal results due to formic acid's ability to create a pH environment that balances precursor hydrolysis and electrostatic interactions.

The deposition of the metals was maintained constant for each experiment: under continuous irradiation by UV light ($\lambda = 365$ nm) for 20 min with irradiance $E = 30$ W m^{-2}. Before and during irradiation, the cell containing the slurry was carefully purged with nitrogen to remove oxygen from the reaction environment (15 min at 100 ml/min). The removal of oxygen is fundamental to avoid the competitive oxygen reduction reaction.

As a post-deposition, the sample was washed twice by centrifugation to remove organic chlorine and residual metal synthesis byproducts. The samples and the remaining liquid after centrifugation were then frozen at −24 °C, followed by overnight freeze-drying.

Commercial samples have been provided by Chimet S.p.A. Unreduced catalyst was prepared by deposition-precipitation method using TiO_2 P25 as a support, Na_2CO_3 as basic agent, and precursor Na_2PdCl_4 as Pd source (2 wt.% Pd with respect to the support). The pre-reduced catalyst was prepared using the same deposition-precipitation protocol adding a liquid phase reduction step with HCOONa at 65 °C. All catalysts were carefully washed until complete Cl removal was achieved and then dried at 105 °C overnight.

3.2 XAS data collection

3.2.1 Pt L_3-edge laboratory XAS measurements

Pt L_3-edge X-ray XANES spectra were measured in *operando* regime using R-XAS Looper (Rigaku, Japan) laboratory X-ray absorption spectrometer at the Smart Materials Research Institute of Southern Federal University. The measurements were performed in fluorescence geometry. The energy was selected by a Si(620)

Johansson-bent monochromator, providing energy resolution of $\Delta E = 1.5$ eV at Pt L_3-edge energy (11564 eV). The incident beam intensity was measured by Ar-filled (300 mbar) ionization chamber, and the fluorescence signal was measured by a silicon drift detector.

For these measurements the custom-made photocatalytic cell was used, which will be discased in more detail in Chapter 4 section 4.1.

Experimental procedure involves preparation of the solution of formic acid (>98% Sigma-Aldrich) and deionized water (1:3) was prepared and stirred for 10 minutes at room temperature. 2 mg of K_2PtCl_6 (Sigma Aldrich) was then added to 13.3 mL of the prepared solution and stirred for 30 minutes. The TiO_2 ink was prepared by mixing ca. 7 mg of TiO_2 (634662 Sigma-Aldrich, titanium(IV) oxide, mixture of rutile and anatase, nanopowder, <100 nm particle size (BET), 99.5% trace metals basis) with 100 µl deionized water. The ink was deposited on the window of the photocatalytic cell and left to dry for 15 min. The solution of K_2PtCl_6 (ca. 10 mL) was then added, and the closed cell was bubbled with Ar (20 mL/min, 15 min). Then, the gas inlet was adjusted to flush only the headspace of the cell in order not to create bubbles in the liquid during the measurements. The LED UV light source (370 nm, 3.9 W) was applied from the window opposite to the TiO_2 layer.

3.2.2 Pt L_3-edge synchrotron XAS measurements

The Pt L_3-edge XAS measurements were performed at BM23 beamline of ESRF, France. The energy was selected by Si (111) double-crystal monochromator operated in step-scanning mode. The Rh-coated mirrors were used to reject the contribution of higher harmonics. For energy calibration, platinum foil was measured simultaneously with the sample using a 3^{rd} ionization chamber. The beam size dimensions were 0.5 x 2 mm.

For the first experimental procedure, fluorescence mode was used. The different TiO_2 powders were prepared as inks as in the case of the laboratory XAS experiment and deposited on the windows of the custom-made photocatalytic cell for photocatalytic studies. Then the procedure for preparing the solution was repeated. The amount of Pt precursor was calculated for every sample depending on the amount of TiO_2, to reach the nominal Pt loading of 2 wt.%. The cell was placed between the first and second ionization chambers. The fluorescence detector was oriented at *ca.* 45° with respect to the incoming beam, from the same side as the UV source (see ***Figure 22***). The closed cell contentiously bubbled with Ar (20 mL/min).

For the second experimental procedure *in situ* XAS data were collected in transmission mode. The samples were pressed into a pellet to optimize the absorption step at Pt L_3-edge. The pellet was loaded inside the microtomo cell [135] allowing us to control the sample temperature and atmosphere.

During the experimental procedure the fresh samples were first reduced in a flow of 4% H_2 (50 ml/min) at 150 °C. The subsequent procedure included a sequence of oxidation in a flow of 10% O_2 in He (50 ml/min), at temperatures from 50 to 400 °C followed by exposure at 400 °C for 25 min with collection of XAS data at each step. In total 14 subsequent spectra were collected during the temperature ramp in H_2 and 30 spectra for ramp in O_2. After each step with temperature heating, EXAFS spectra up to k=12 Å^{-1} were taken for further comparison of reduced and oxidized states. The photon energy was scanned from 11.35 to 12.42 keV for the temperature ramps and 11.35 to 12.42 keV for reduced and oxidized states.

XAS data analysis, including LCA and EXAFS fitting, was done in Demeter software [136]. First-shell fitting of the averaged EXAFS data was performed in R-space in the 1.5-3.2 Å range on $k^{1,2,3}$-weighted data Fourier-transformed in 3-10 Å^{-1} range. The first-shell Pt–Pt interatomic distance ($R_{Pd\text{-}Pd}$), Debye–Waller factor ($\sigma_{Pd\text{-}}$

$_{Pd}$), coordination number (N_{Pd-Pd}), and zero potential correction (ΔE_0) were used as fitting variables.

3.2.3 Pd K-edge synchrotron XAS measurements

In situ Pd *K*-edge XAS data were collected at the NOTOS beamline of ALBA synchrotron (Spain). The NOTOS beamline source is a 1.42 T bending magnet with 8.5 keV critical energy and a maximum flux of 10^{11} photons/s at this critical energy. The beamline optics consist of a cylindrical mirror (M1) with a downward orientation, with a Si and a Rh stripe, that collimates the beam onto a double crystal monochromator (DCM) made by CINEL. The DCM is a direct drive monochromator with a fixed exit and two pairs of crystals, Si(111) and Si(220), enabling an energy range between 4.7 and 30 keV. The beam coming from the DCM impinges on a Rh-coated double channel toroidal mirror (M2, with 34- and 55-mm sagittal radii of curvature), which allows for horizontal focusing of the beam on the sample. For this experiment, the beamline optics were optimized for the Pd *K*-edge (24.35 keV) by using the Rh-coated stripe of M1, the Si(111) crystals pair, and the 34 mm channel of M2. The beam size dimensions were 250 x 370 μm^2 (HxV) approximately. The DCM was operated in continuous scanning mode and the energy was scanned within 24.2 – 24.9 keV range (ca. 1 min per spectrum).

The improved custom-made photocatalytic cell (see ***Figure 35***) for the Pd photodeposition on TiO_2 was oriented perpendicularly to the incoming X-ray beam, allowing the collection of both fluorescence and transmission signals. The transmission measurements were acquired with three ion chambers as detectors with a proper gas mixture, optimized to improve the measured signal (absorbing *ca*. 15%, 85% and 85% respectively). The custom-made photocatalytic cell was placed between the first and second ionization chambers, and a Pd metallic reference foil was placed between the second and the third to check for energy calibration. The fluorescence detector, a 13 channel Si drift detector (SDD) from

Mirion Technologies (Canberra Olen), was oriented at *ca.* 45° with respect to the incoming beam, from the same side as the UV source (see ***Figure 35***).

Pd/TiO_2 samples were prepared directly during the XAS experiment. First, the P25 powder was dissolved in water and the resulting TiO_2 ink (~15 mg of dry powder, measured for each sample) was deposited on the window of the photocatalytic cell and left drying. The cell was then filled with a mixture of 15 ml of Mili-Q water and 10 μL of formic acid. The amount of Pd source (1 mg ml^{-1} Pd in 5% HCl, Sigma-Aldrich) was calculated for every sample (~300 μL) depending on the amount of TiO_2, in order to reach the theoretical maximal loading of 2 wt% Pd/TiO_2. The cell was tightly sealed and permanently flushed with He at 20 ml min^{-1}, the outlet being monitored by a Cirrus 3-XD mass spectrometer (MKS Instruments). Then, the cell window was irradiated by a remotely controlled UV LED source (λ = 365 nm). After 20 min of total exposure to UV radiation, an additional 1 ml of formic acid was added to the cell as a hole scavenger and the cell was continuously exposed to UV irradiation.

XAS data for redox treatment were collected using the *operando* cell [137] and remotely controlled gas setup. The catalyst (ca. 20 mg) was loaded and fixed with a quartz wool inside the *operando* cell equipped with two graphite windows. As in the case witch Pt the experimental procedure includes the sequence of the reduction of fresh samples in a flow of 4% H_2 (50 ml/min) at 150 °C for 15 min, followed by oxidation (in a flow of 48 ml/min 10% O_2 in He) at temperatures from 50 to 400 °C exposure at 400 °C for 25 min with a continuous collection of XAS data at each step.

Here also Demeter software was used for XAS data analysis [136]. The First-shell EXAFS fitting was performed in *R*-space in the 2-3 Å range on $k^{1,2,3}$-weighted data Fourier-transformed in 3-11 $Å^{-1}$ range. The fitting variables *include* $R_{Pd\text{-}Pd}$, $\sigma_{Pd\text{-}Pd}$, $N_{Pd\text{-}Pd}$, and ΔE_0.

Additional Pd *K*-edge XAS measurements were done at SuperXAS beamline of the Swiss Light Source (SLS, Villigen, Switzerland) [138] to monitor the temperature evolution of Pd NPs under inert atmosphere. The data was also measured in transmission geometry using Ar-filled ion chambers (ca. 10% absorption in each chamber). The channel-cut Si(111) monochromator was operated in quick scanning mode oscillating at 1 Hz. Ca. 20 mg of the sample has been loaded inside 3 mm quartz glass tubes and fixed from both sides with a quartz wool. The capillary was connected to a remotely controlled gas system. Two heating cartridges on the top and bottom parts of the capillary were used to regulate the temperature. During the experimental procedure the fresh samples were first reduced in the flow of 5% H_2 (20 ml/min) at 150 °C for 15 min. The subsequent procedure included heating in inert flow (Ar, 50 mL/min) from 50 to 400 °C with a continuous collection of XAS data. For these spectra, the data extraction was done in ProQEXAFS code [139], which included energy calibration, normalization and averaging. First-shell fitting was performed on the averaged data (by 4 min, 240 spectra) with same parameters as described above, but using the *k*-range of 3-13 $Å^{-1}$.

3.3 UV-Vis data collection

UV-Vis spectra were measured on Shimadzu UV-2600 spectrophotometer. The photocatalytic cell was equipped with a needle outlet, through which the aliquots of the solution (ca. 1 mL) were taken for the UV-Vis spectrum accumulation (ca. 3 min), and then returned to the cell. The sample and the reference (distilled water) were filled into two quartz cuvettes of 5 mm thickness. First, the UV-Vis spectrum was collected for a solution purged for 15 minutes with Ar. Then, starting from the moment of UV light irradiation, the probe was taken every 6 minutes and, upon completion of spectrum accumulation, was returned back to the cell. For all data the spectral acquisition was performed with a 0.5 nm step in the 600-185 nm range.

3.4 Mass spectrometry data collection

Several *operando* mass spectrometry experiments were done during hydrogen production using Pt/TiO_2 samples.

Thew MC data for laboratory experiment was collected using online quadrupole mass spectrometer TekhMas 7-100 (AtomTyazhMash, Russia), and for synchrotron experiment the resulting gas mixture after the sample was analysed by online mass spectrometer (Pfeiffer OmniStar GSD 320) on BM23 ESRF, France and Cirrus 3-XD mass spectrometer (MKS Instruments) on NOTOS beamline, ALBA synchrotron, Spain. The device was attached via T-connection to the gas outlet of the photocatalytic cell to monitor the signal of the produced H_2 ($m/Z = 2$). The signals of Ar, water, oxygen, nitrogen and formic acid were also tracked.

3.5 Photocatalytic hydrogen evolution tests

The hydrogen production experiments were performed irradiating with UV light at 365 nm with an irradiance of 40 W/m^2. The irradiation experiments were carried out in magnetically stirred, cylindrical quartz cells containing 5 mL of slurry with 5 mg of sample. Slurries containing 750 μL of methanol as hole scavenger. Before irradiation the cell containing the slurry was carefully purged with nitrogen to remove oxygen from the reaction environment. The removal of oxygen is fundamental to avoid thecompetitive oxygen reduction reaction. Hydrogen and CO_2 evolution was followed by sampling periodically 2.5 mL of gas from the irradiation cell and replacing it with the same volume of N_2. The gas sample was analysed with an Agilent 490 Micro GC gas chromatograph equipped with a Molsieve 5 Å column for H_2 analysis and a Poraplot U column for CO_2 quantitation.

During the analysis the columns were kept at temperatures of 363 K and 313 K at a pressure of 200 kPa and 150 kPa, respectively. The carrier gases were argon and helium, respectively. The total amounts of H_2 and CO_2 produced as a function of time were calculated from the concentration in the sampled gas, considering the total volume of gas in the irradiation cell and the previous samplings.

3.6 X-ray diffraction measurements

XRD patterns were collected using a Bruker D2 PHASER instrument (Bruker, Billerica, MA, USA) with a Cu K_α source. The sample for XRD measurement was prepared by dissolving 20 mg of K_2PtCl_6 in 133 mL solution of formic acid and deionized water (1:3). The solution was irradiated by UV light for 1 h and then dried overnight. The remaining solid fraction was put on a low-background sample holder and the XRD data were collected in Bragg–Brentano geometry in the 2θ range from 20–90° with a step of 0.01°. The Pawley fitting was done in Jana2006 [140].

3.7 X-ray fluorescence analysis

Pt content in TiO_2 after the photodeposition was determined by X-ray fluorescence (XRF) spectroscopy on M4 Tornado spectrometer (Bruker, Billerica, MA, USA) with an XFlash 430 detector in the range from 0 to 25 keV. The signal was collected from 20 different points of the sample, and the averaged value together with the standard deviation were calculated.

3.8 FTIR data collection

FTIR measurements were carried out in transmission mode. To conduct the experiment samples were pressed into thin self-supporting pellets. For the pellet, optical density (O.D.) was calculated (ca. 10 $mg \cdot cm^{-2}$)) so that after obtaining the

IR spectra, it was possible to perform normalization for comparing the samples with each other.

$$\mathrm{O.D.} = \frac{Mass\ of\ pallet\ (gr)}{Area\ of\ pallet\ (cm^2)} \qquad (9)$$

The pellet was mounted in a gold frame and placed in an IR cell made of quartz (***Figure 15***), which allows performing *in situ* experiments. The cell allows performing measurements under a controlled gas atmosphere or vacuum as well as temperature treatment from R.T. to 800 °C (***Figure 15*a**). *In situ* IR cell is equipped with KBr windows that allow the incoming IR beam to pass through the samples and detect the transmitted radiation.

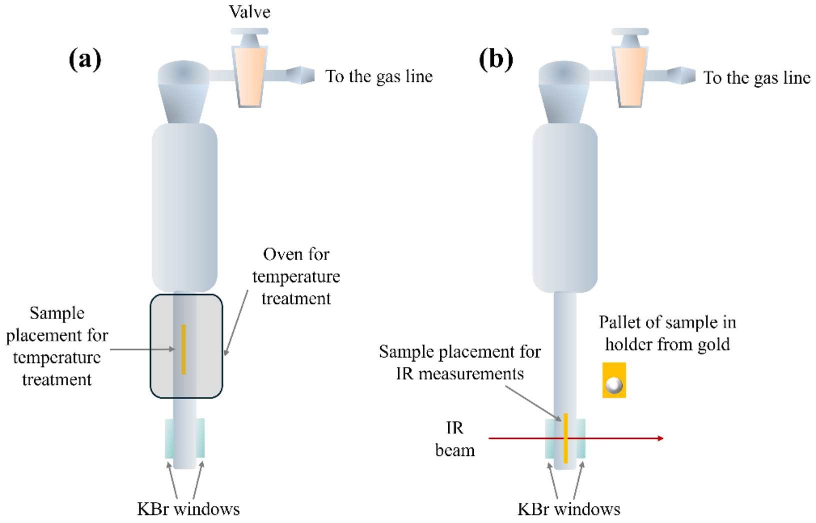

Figure 15. Scheme of quartz *in situ* cell used for activation of the sample and IR analysis in transmission mode (a) configuration for temperature treatments, (b) configuration for IR measurements.

The cell is connected to a dedicated vacuum line, which allows for controlled dosing of gas inside the cell and subsequent stepwise outgassing.

Thermal treatment was prior to *in situ* IR spectroscopy analysis and was performed in a dynamic vacuum while heating with rate 10 °C/min from R.T. to 400 °C and then staying for 1 hour at upper temperature. This was followed by oxidation with 50 mbar of O_2 in static condition for 15 minutes. Then degassing under a dynamic vacuum for 30 minutes. The oxidation was repeated 2nd time but then followed by cooling to 150 °C in an oxygen atmosphere and only after that degassing step of 30 minutes was made. As a final step sample was cooled down to room temperature in a dynamic vacuum.

FTIR spectroscopic measurements were performed in transmission mode on a Bruker INVENIO FTIR spectrometer equipped with MCT or DTGS detectors.

DTGS detectors (Deuterated alanine doped Tri-Glycine Sulphate) are based on a pyroelectric effect. Incoming IR radiation heats and expands the detector material. This FTIR detector works particularly well under room temperature conditions. However, they require a high amount of IR radiation to produce spectra of decent quality.

MCT detectors (Mercury cadmium telluride) are based on an internal photoelectric effect. Here, incoming IR radiation excites electrons into the conduction band. This excitation can also be triggered by thermal processes. Thus, it is necessary to cool MCT detectors to suppress thermally induced noise. As a result, they offer the highest sensitivity in IR applications. They are typically used in low-light scenarios. MCT FTIR detectors offer significantly better signal-noise ratios and exhibit much faster response times than DTGS detectors.

The infrared spectra were measured in transmission mode with 4 cm^{-1} resolution. The spectra were collected by averaging 64 scans.

Once the IR spectrum of the activated sample was collected, 35 mbar of CO were admitted to the cell and IR spectra were collected over an hour: 5 spectra during the first 10 min (i.e. a spectrum every 2 min), 5 spectra during the following 25 min (every 5 min), and finally 3 more spectra with a delay of 10 min.

3.9 *Ex situ* HAADF-STEM measurements

HAADF-STEM micrographs and Energy-Dispersive X-ray spectroscopy (EDX) elemental maps were acquired in a double-corrected Spectra 300 STEM microscope (ThermoFisher Scientific) operated at 300 kV. The images from TEM were processed in ImageJ (v.1.54g , National Institutes of Health, Bethesda, MD, USA) code [141]. Histograms of particle size distribution were obtained by measuring 150-250 particles for each sample. For sample deposition, powder samples were dispersed in water, sonicated and deposited on lacey carbon Cu grids with ultrathin carbon layer.

3.10 *In situ* HR-STEM characterization

In situ STEM experiment was conducted at Ernst Ruska-Center, Forschungszentrum Jülich, Germany). The two powder samples were prepared on Norcada *in situ* heating chips and analyzed with a probe-corrected environmental STEM Hitachi HF5000 cold FEG electron microscope.

The experiment was made at 200 kV and 80 kV to account for the effect of the beam damage. Images were acquired in high-angle annular dark field (HAADF), bright field (BF), and secondary electron (SE) modes. During *in situ* experiment, the samples were exposed to flows of H_2 (2.7 sccm/sec) and O_2 (0.6 sccm/sec) and were heated up to 150 °C and 400 °C, respectively, with rate 1 °C/sec. After the *in situ* experiment, energy-dispersive X-ray spectroscopy (EDX) element maps (UltimMAX LTE, Oxford instruments, UK) and electron energy loss spectra (EELS) (CEFID, CEOS GmbH, Germany) were collected under vacuum conditions. To calculate Pearson correlation coefficient for Ti and Pd EDX maps, the corresponding images were first convoluted with a 2-pixel-width Gaussian, and then the signal and the background were separated by applying a threshold value of 15 to the 265-bit images. Both image processing and Pearson correlation coefficient calculation were performed in Python using NumPy and SciPy libraries. The particle size distributions were obtained by counting 150-200 NPs for each sample at each step.

3.11 *In situ* EPR spectroscopy measurements

X-band (9.5 GHz) electron paramagnetic resonance (EPR) spectroscopy experiments were performed at 77 K on an EMX Bruker spectrometer, equipped with a cylindrical cavity operating at 100 kHz field modulation. All treatments were performed *in situ* in a quartz cell connected to a conventional high-vacuum apparatus (residual pressure $<10^{-4}$ mbar). Sample reduction was performed by dosing 50 mbar of hydrogen in the EPR cell and subsequent heating at 150 °C for 15 min.

4 *Operando* and *in situ* spectroscopy study of Pt/TiO_2 photocatalyst during photodeposition and hydrogen evolution reaction

A number of works has been devoted to studying the process of hydrogen production using TiO_2 photocatalysts containing Pt using UV-Vis spectroscopy [142-144]. But examples of *operando* XAS experiments are less common [102, 103], which, as we have already discussed above, is due to the complexity of creating cells for conducting such measurements.

The work discussed in this chapter is focused on the *operando* investigation of a catalytic system during photodeposition of Pt on TiO_2 and photostimulated H_2 production, by simultaneous laboratory X-ray absorption and UV-Vis spectroscopies with using mass spectrometry for online monitoring of the reaction products. As we discussed, combination of multiple spectroscopic techniques is a commonly used approach for gaining complementary information about the materials' structure. To make this experiment possible, a custom-made photocatalytic 3D-printed cell was designed to study the photocatalysts under *operando* conditions in real time.

4.1 Design of custom-made photocatalytic cell

Inspired by other works, we designed a custom-made photocatalytic cell (***Figure 16***). The cell was 3D-printed using a digital light processing 3D printer Asiga UV MAX (Asiga, Australia, Sydney) with a wavelength of 385 nm and a light intensity of 7.25 mW/cm^2. The first layer was chosen to be 25 μm and was exposed for 20 s to avoid delamination of the print from the platform. The thickness of the layers was set to 25 μm and each layer was exposed for 1.1 s. To avoid delamination of the layers during the process the z-compensation was set to 300 μm. For better processability of the resin, the resin was processed at an optimized temperature of 47 °C. Immediately after printing the cell underwent sonication in IPA for one minute at 80 kHz, and then mounted in the holder for manual flushing of with IPA. After flushing the cell was blown dry with nitrogen. Lastly, the cell was post-cured for 2 min using a UV-radiation lamp (type Flash DR-301C, Asiga, Australia, Sydney).

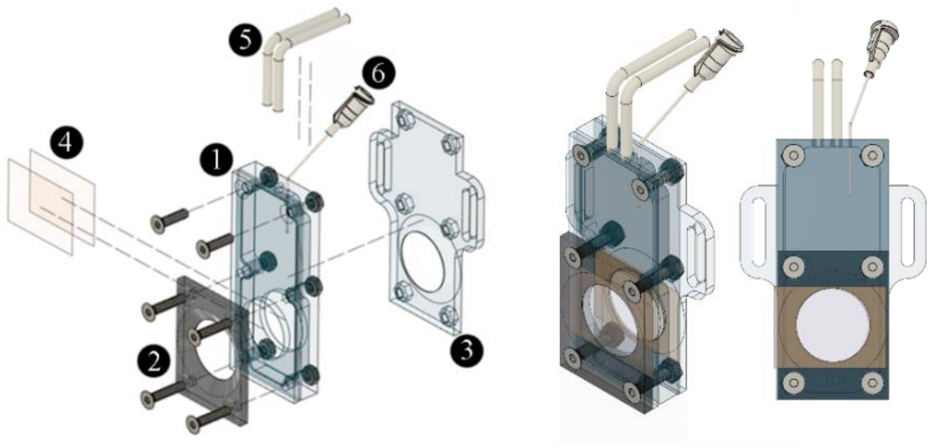

Figure 16. Schematic of the photocatalytic cell with its main parts: 1 - main body, 2 - front window cap, 3 - back window cap with fixture for Rigaku sample holder, 4 - front and back windows, 5 - pipes for gas inlet and outlet, 6 -needle for liquid inlet/outlet.

The cell has a hollow design. The body – **1** (size 3 by 8 cm) is connected by screws, on one side, to the front cover – **2**, made in the form of a square plate. On the other side, the body is connected to the back cover – **3**. The back cover is made with two side loop-shaped fasteners, with the help of which the cell is fixed in the position most convenient for XAS measurements.

The main body, front cover and back cover have a hole with an inert diameter of 2 cm. These holes are positioned so that when the cell is closed with screws they coincide. The front cover and back cover serve to press the windows together, thereby preventing leakage. The windows – **4** are fabricated from materials transparent to X-rays and UV radiation. The distance between two windows, i.e. the thickness of the solution, was 4.6 mm.

The front window is designed to apply the catalyst in the form of ink, as well as for carrying out XAS measurements in the fluorescence mode. UV irradiation can be applied either to the front window or to the back window, depending on the required configuration specified by the location of the X-ray and UV detectors. An LED lamp can be used as a source of UV radiation (for carrying out photocatalytic reactions).

In the upper part of the body, two plastic pipes – **5** are installed to supply inert gas and remove gas reaction products, respectively. The reaction products can then be sent to a mass spectrometer. In the upper part of the cell body, there is also a small hole – **6**, which is used to supply and remove the analyzed solution during the reaction.

The custom-made photocatalytic cell allows simultaneous XAS/UV-Vis/MS characterization in the liquid phase under irradiation with a light source.

To test the developed cell, an experiment was conducted in laboratory conditions. An *operando* photocatalytic cell was mounted inside a Rigaku R-XAS spectrometer as shown in ***Figure 17*** adopting the fluorescence geometry: the incoming X-ray beam arrived from the left at ca. 45° with respect to the front window, while the fluorescence detector was located above the sample at ca. 90° with respect to the incoming beam. The 370 nm UV source with a remotely controlled digital power supply was applied from the back window. Pt L_3-edge XAS spectra were measured in fluorescence mode.

The process of preparing the system for measurements involves the preparation of a sample in ink form. The TiO_2 ink was prepared by mixing TiO_2 with deionized water. The ink was deposited on the front window of the custom-made photocatalytic cell and left drying for 15 min. The magnetic stirring bar was placed inside the cell before closing it with front and back covers with already attached windows. Then the cell was filled via the upper inlet with the solution necessary for the reaction to occur. The solution consists of a mixture of formic acid and deionized water (1:3), with 2 mg of K_2PtCl_6 as a Pt (for more details see Chapter 3 section 3.2.1).

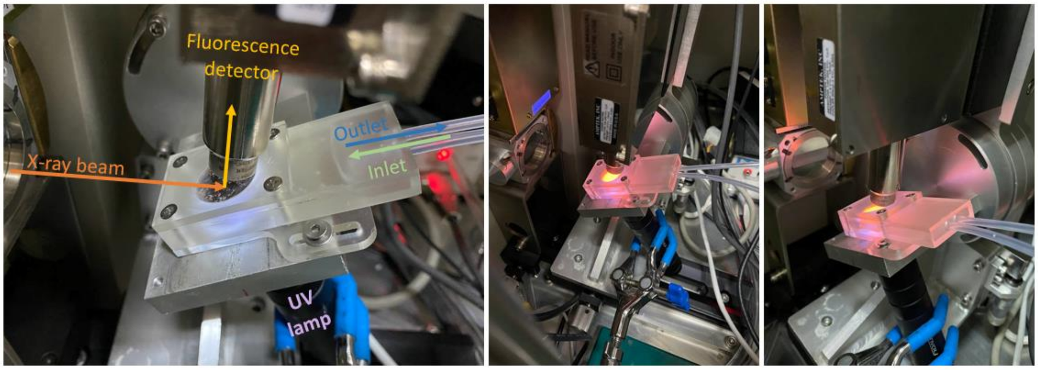

Figure 17. Photo of the cell installed in the Rigaku R-XAS spectrometer during the photocatalytic experiment.

The cell was placed above the magnetic stirrer for continuous mixing of the solution. The inlet pipe was used for continuous purging of the cell with an Ar for 15 min to avoid the presence of atmospheric oxygen inside the cell, which can lead to the formation of by-products of the reaction. Then, the gas inlet was adjusted to flush only the headspace of the cell in order not to create bubbles in the liquid during the measurements. The gas outlet was employed for MAS spectroscopy measurements. The LED UV light source (with irradiance 400 W/m^2) was applied from the window opposite to the TiO_2 layer.

4.2 Tracking Pt photodeposition on TiO_2 in laboratory conditions

The first challenge was to track the evolution of the oxidation state of Pt on the course of photodeposition. At the beginning of the experiment, Pt is in the cationic form in solution. However, the concentration of Pt in the solution adopted during the photodeposition experiment was too low to collect high-quality XAS data, which was further complicated by the attenuation length of Pt *L*$_3$-edge energy photons in water of only about 3 mm. For this reason, a reference K_2PtCl_6 salt was measured *ex situ* (deposited on the window in the same setup but without the solution and TiO_2) resulting in the characteristic Pt^{4+} XANES spectrum as shown in ***Figure 18a***, black line.

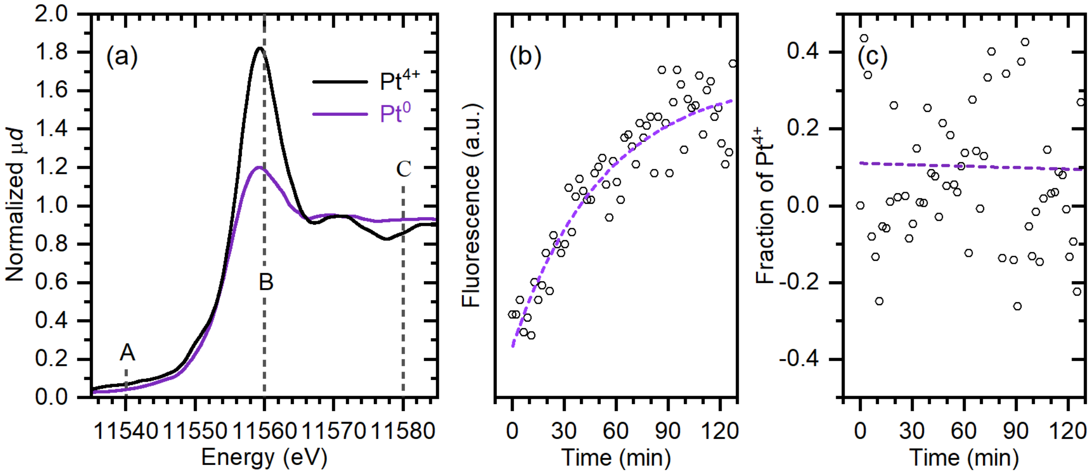

Figure 18. (a) Pt *L*$_3$-edge XANES of solid K_2PtCl_6 (black) and Pt/TiO_2 at the end of *in situ* photodeposition experiment (purple). The dashed vertical lines highlight the energy points in which the time-resolved fluorescence was collected. (b) Evolution of the absolute intensity of the fluorescence Pt signal in points B and C over time during the *in situ* photodeposition experiment, fitted by an exponential function (purple dashed line). (c) Estimation of Pt^{4+} fraction based on Equation (1), fitted by a linear function (purple dashed line).

A second challenge derives from the use of a laboratory source for collecting XAS spectra. A significant amount of time was required for the collection of a single spectrum compared to the synchrotron sources, which was not compatible with the time resolution needed to follow the Pt photodeposition process. Therefore, on the basis of the K_2PtCl_6 reference spectrum, three energy points were chosen (A, B, and C in ***Figure 18a***): before the edge (11540 eV), at the white line (11560 eV), and after the white line (11580 eV). During the *in situ* Pt photodeposition from the solution onto the TiO_2 support under UV irradiation, the fluorescence signal was continuously collected in these three points only. After 2 h of irradiation, the UV source was switched OFF, and a complete XANES spectrum was collected *in situ* (***Figure 18b***, violet curve). This spectrum was characterized by a significantly reduced intensity of the white line at 11560 eV, with respect to that of K_2PtCl_6, and is characteristic of the Pt^0 state.

The relative fraction, *γ*, of the Pt^{4+} species that contributes to the fluorescence counts were estimated based on the relative intensity of the white line (point B), following Equation (10):

$$\gamma = \left(\frac{I_B - I_A}{I_C - I_A} - \frac{I_B^0 - I_A^0}{I_C^0 - I_A^0}\right) \Big/ \left(\frac{I_B^{4+} - I_A^{4+}}{I_C^{4+} - I_A^{4+}} - \frac{I_B^0 - I_A^0}{I_C^0 - I_A^0}\right) \qquad (10)$$

where I_A, I_B, and I_C are the intensities of the fluorescence signal at 11540, 11560, and 11580 eV, respectively, measured for the *in situ* sample (I), metallic Pt reference (I^0), and K_2PtCl_6 reference (I^{4+}).

As can be seen from ***Figure 18c*** the Pt^{4+} fraction on TiO_2 was negligible at every stage of the experiment. Within the standard deviation, it was close to zero and did not show any trend. It should be also noted that the attenuation length of the Pt L_3-edge energy for TiO_2 was ca. 50 μm, while the estimated thickness of the TiO_2 layer was below 5 μm. Thus, the collected XAS signal is representative of the whole thickness of the TiO_2 layer, while is not informative about the Pt precursor present in the bulk of the solution. Based on the above, it can be concluded that only Pt^0 species were found on the TiO_2 layer during the whole photodeposition experiment.

The XRF analysis was made to determine actual Pt loading during the photodeposition. The results show 1.97 ± 0.47 Pt content (wt.%) after 1 h under UV and proof that only Pt and TiO_2 are present in the samples.

Simultaneously with XAS data acquisition, H_2 evolution was monitored by online MS (***Figure 19a***). The signal of hydrogen was observed at the beginning and reached a value close to its maximum after only the first 10 min of experiment, even though the Pt photodeposition was still in progress and required a much longer time to be completed. This is evident in ***Figure 18b***, which reports the evolution of the integral fluorescence signal over time proportional to the amount of platinum photodeposited onto the TiO_2. A less significant increase in H_2 production activity after the first 10 min may be explained by the fact that the parallel increase of the fluorescence signal, proportional to the amount of Pt in the TiO_2, was associated with the growth of existing particles and not their quantity.

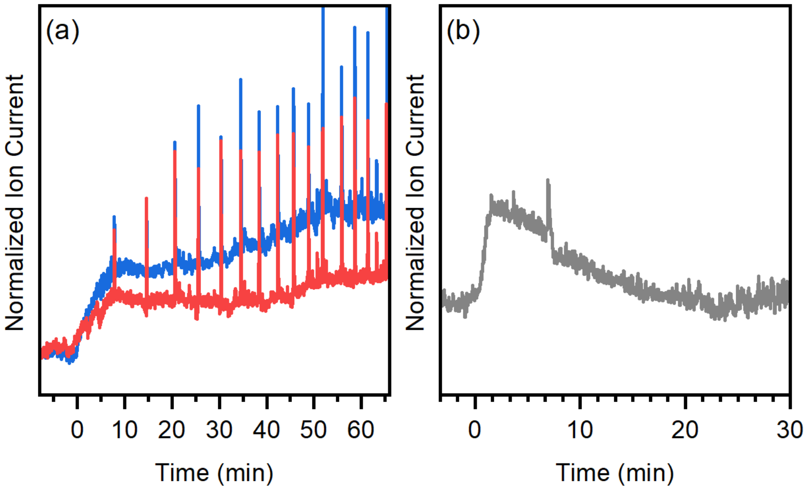

Figure 19. (a) MS signal of m/Z = 2 (blue) and m/Z = 44 (red) divided by the signal of m/Z = 40 and normalized by area. (b) Normalized MS signal of m/Z = 44 recorded during the UV irradiation of K_2PtCl_6 dissolved in the solution of deionized water with formic acid (1:3) same as in (a) but without addition of TiO_2.

Additional *ex situ* experiments using the GC were performed to better assess the photocatalytic performance of the system and have quantitative data (***Figure 19b***). The H_2 photoproduction had a linear trend in 60 min test. The H_2 evolution rate was about 3.5 mmol g_{cat}^{-1} h^{-1}, with a similar rate for CO_2 production. The evolution rate for H_2 and CO_2 is nearly the same due to the stochiometric ratio in the formic acid photoreformig rection, the slight difference (~6%) falls well within the experimental error of this kind of experiment. The observed rate is comparable to other Pt/TiO_2 systems reported in literature [145, 146].

4.3 Insights on the Pt species in solution

Every 6 min during the photodeposition experiment, small aliquots of the solution (ca. 1 mL) were extracted for UV–Vis measurements and were immediately returned to the cell after a spectrum was collected. The spectrum of the initial solution (black in ***Figure 20a***), measured against distilled water as a reference, had two bands at 260 nm and in the 200–250 nm range, corresponding to the charge transfer transition involving the Pt^{4+} species and absorption by formic acid, respectively.

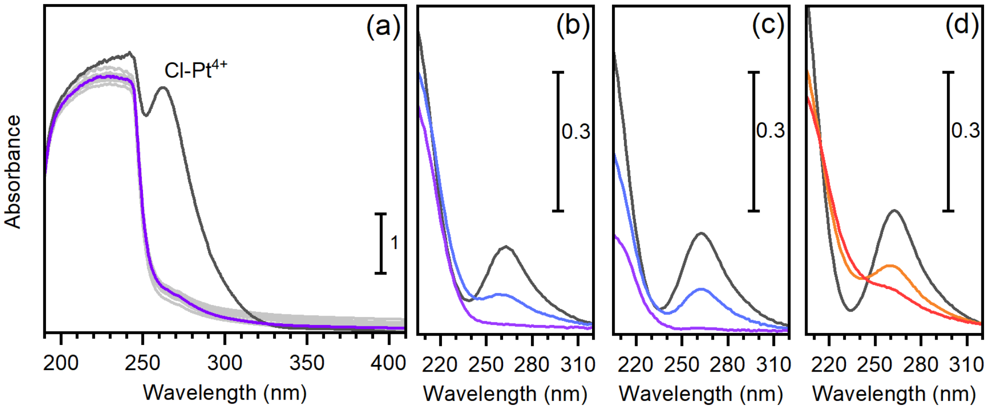

Figure 20. (a) Evolution of UV–Vis spectra of the K_2PtCl_6 solution during photodeposition of Pt on TiO_2. The spectra before and after 90 min UV irradiation are shown in black and violet, respectively; intermediate data are shown in light grey. (b-d) Evolution of UV-Vis spectra of the solution containing K_2PtCl_6 upon UV irradiation. The K_2PtCl_6 precursor was added to (b) a solution of water and formic acid (3:1) with TiO_2, (c) a solution of water and formic acid (3:1) without TiO_2, and (d) deionized water only. Initial states are shown by black lines, and the spectra taken after 30 s, 90 s, 5 min, and 15 min, are shown by blue, purple, orange, and red lines, respectively.

Notably, the latter band had already disappeared from the collected spectrum after 6 min of UV irradiation, and no significant changes were observed over the following 90 min. Formic acid absorption also decreased over time. At the same time, the fluorescence signal of the Pt^0 on TiO_2 grew over a significantly larger time scale (***Figure 18*****b**), indicating that only a minor part of the reduced Pt^{4+} species are deposited on the TiO_2 support in the first 6 minutes of the reaction.

To track the Pt photoreduction process in more detail, three additional UV-Vis experiments were carried out (K_2PtCl_6 precursor was addedto a solution of water and formic acid (3:1) with TiO_2 (***Figure 20b***), a solution of water and formic acid without TiO_2 (***Figure 20c***) and deionized water only (***Figure 20d***) with better time-resolution (ca. 30 s per spectrum) without simultaneous XAS data collection.

First photodeposition experiment repeats all experimental conditions as initial one, but to slow down thereduction of Pt^{4+} species and monitor a gradual decrease of the corresponding peak in the UV-Vis spectra, the Pt concentration was lowered by the factor of 5, and the UV lamp was placed at 0.3 m distance from the cell. The obtained results (***Figure 20b***) also demonstrate a rapid decrease of the Pt^{4+} signal already after 30 s of exposure (blue spectra).

A second experiment was performed under similar conditions but omitting the addition of TiO_2. The results (***Figure 20c***) were very similar to those obtained in presence of TiO_2, indicating that the reduction of the K_2PtCl_6 precursor occurred exclusively due to UV irradiation, and interaction with TiO_2 was not necessary at this stage. This finding also explained why the reduction of the Pt^{4+} precursor in solution, as monitored by UV-Vis spectroscopy, occurred before its deposition on TiO_2 as observed by XAS. However, evidence of the formation of Pt nanoparticles was not observed in the solution, which would give rise to a broad spectral feature in the UV-Vis spectra, arising from light scattering by the nanoparticles.

Finally, the third experiment was performed removing also the formic acid from the solution (i.e. only K_2PtCl_6 precursorin deionized water). The results shown in

Figure 20*d* indicate that the reduction process was slowed down by an order of magnitude, which emphasizes the role of the hole scavenger in the photoreduction of Pt^{4+} to Pt^0.

For this reason, the fourth experiment was performed where the same amount of K_2PtCl_6 precursor was dissolved in a mixture of deionized water and formic acid (3:1) and irradiated by UV light. In this experiment the UV-Vis data were measured against the solution of formic acid and water as a reference to exclude formic acid absorption from the resulting spectrum. As can be seen in

Figure* 21*a, the Pt^{4+} signal completely disappeared after 1 h of irradiation (from black to purple) as was observed for initial UV-Vis experiment. After UV irradiation, the solution became dark and provided an increased background to the UV–Vis spectra, which can be attributed to the scattering by Pt nanoparticles in the solution [147].

The solution after the 4th experiment was dried, and the remaining fraction was probed by XRD. Broad peaks of *fcc* platinum with a cell parameter of 3.9194(4) Å co-existed with the reflections from KCl salt with a cell parameter of 6.3011(5) Å (

Figure* 21*b). The average crystallite size of the platinum particles, determined according to the *LX* parameter of the Lorentzian-broadening dependence on the scattering angle, was 3.2 nm.

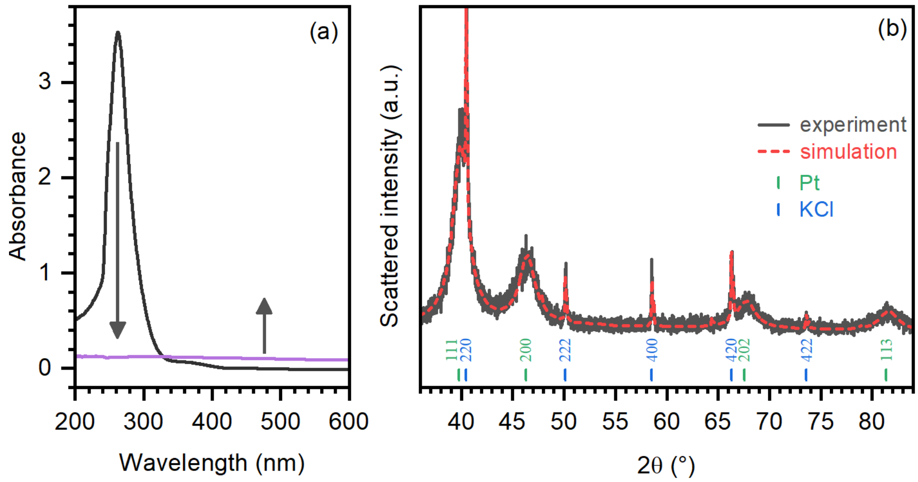

Figure 21. (a) UV–Vis spectra of K_2PtCl_6 in the solution of water and formic acid (3:1) without TiO_2 before (black) and after 1 h of UV irradiation (purple). (b) Experimental (solid black) and simulated (dashed pattern) intensities of the dried sample after UV irradiation.

It is worth noting that, although the reduction of Pt^{4+} was observed in the absence of TiO_2, no hydrogen production was detected in such a sample. However, a CO_2 signal was registered immediately upon the activation of UV light, suggesting its role in the reduction of platinum.

These results demonstrate gradual reduction of platinum during its photodegradation process. The amount of photodeposited Pt on TiO_2 identified as Pt^0 grew progressively over ca. 1 h, while the signal of the produced H_2 was detected and saturated mainly in the first 10–20 min. At the same time, the characteristic Pt^{4+} peak of the precursor in the solution for the UV–Vis data disappeared immediately as soon as the UV light was switched on in the presence of formic acid acting as a hole scavenger. The reduction of Pt^{4+} in the solution to Pt^0 nanoparticles by UV irradiation was also confirmed in absence of TiO_2.

4.4 Synchrotron study of Pt photodeposition process

After acquiring the results under laboratory conditions, a synchrotron XAS experiment using the same custom-made photocatalytic cell was carried out to track the evolution of platinum species during photodeposition process. As in the previous case the Pt L_3-edges XAS measurements were performed in fluorescence mode, with transmission signals collected for energy alignment using Pt foils.

The XAS experiment was conducted at the BM23 beamline at the ESRF synchrotron (see Chapter 3 section 3.2.2). To match the beamline configuration the photocatalytic cell was positioned vertically (***Figure 22***), maintaining a 45° angle relative to the fluorescence detector. In this configuration, the UV irradiation applied from the front window.

The UV irradiation and collection of the fluorescence signal from the same side provided several advantages such as

- It ensures homogenous irradiance of the catalyst over time.
- It confines Pt distribution to UV-accessible regions of TiO_2, ensuring all Pt/TiO_2 species could be considered photoactive.
- It minimizes direct interaction of UV light with Pt species in solution.

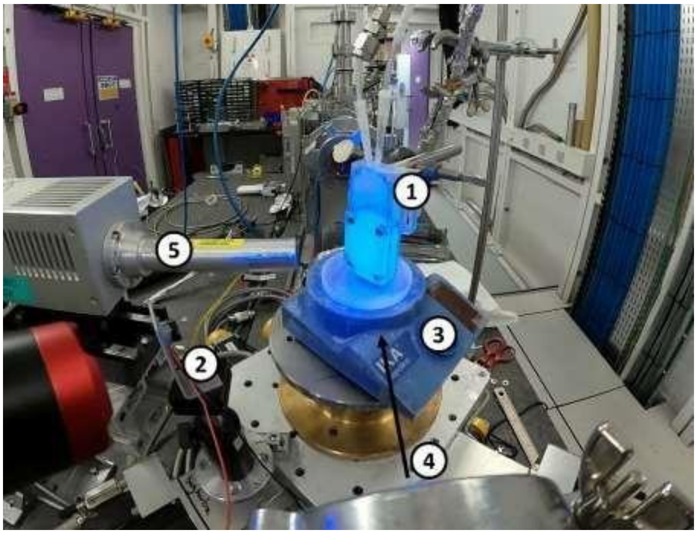

Figure 22. Experimental setup for *operando* photocatalytic studies employed at the ESRF BM23 beamline. (1) Custom-made photocatalytic cell, (2) UV light source, (3) magnetic stirrer, (4) incoming X-ray beam, (5) X-ray fluorescence detector.

The sample preparation was similar to that used in the Rigaku laboratory XAS experiment, except H_2PtCl_6 was used as a Pt precursor, keeping the constant nominal metal loading of 2 wt.%.

UV irradiance was reduced to track the intermediate products in the Pt reduction. Two lower irradiances of 18 and 40 W/m^2 (compared to 400 W/m^2 used during laboratory experiments) were tested during Pt deposition on P25. UV irradiation was applied for 10 s, 20 s, 30 s, 4 min, 10 min and 15 min resulting in cumulative irradiation times of 10 s, 30 s, 1 min, 5 min, 15 min and 30 min, respectively. After each step, XAS spectra were collected to probe the state of the photodeposited Pt.

Notably, during the first XAS spectra measurement a slight reduction of Pt occurred already in the dark due to the beam effect, since synchrotron radiation is stronger than laboratory source (dark green XANES spectra of system in the dark compered to dashed blue XANES spectra of reference H_2PtCl_6 ***Figure 23a***).

The XAS data from both irradiances showed increasing Pt signal with longer X-ray exposure times. However, once saturation was reached, further X-rays exposure had no distinguishable effect on the sample, as indicated by the red lines on ***Figure 23 a* and *b***.

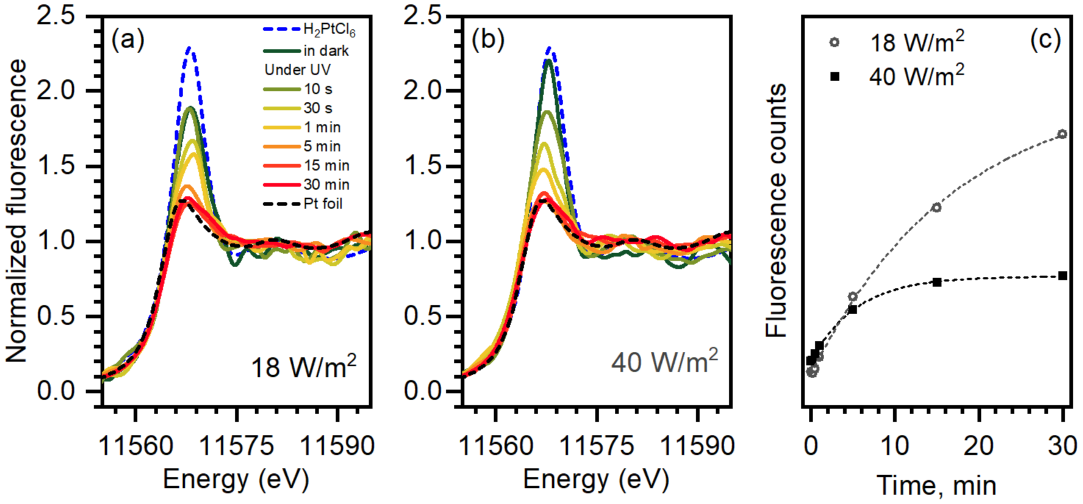

Figure 23. Evolution of XANES spectra during *in situ* UV illumination for 30 min total with different irradiance (18 and 40 W/m^2).

Moreover, the reduction of sample became apparent with the appearance of a dark spot on the cell window and an increase in the fluorescence signal during prolonged XAS spectra acquisition at one point. Unlike UV light, X-rays can penetrate much thicker layers of TiO_2, allowing for deeper interactions. This reduction effect occurred throughout the entire film thickness, meaning that the TiO_2 thickness influenced the final intensity of the fluorescence. The evolution of the fluorescence signal intensity is shown in ***Figure 23c***. The stronger signal observed for lower irradiation value is attributed to the thicker layer of TiO_2 due to the impossibility of applying the same amount of TiO_2 homogenously throughout the whole surface of the cell window, despite all the standardization efforts. Nevertheless, such an approach allows for qualitative tracking of the amounts of photodeposited metal.

4.5 Effect of TiO_2 morphology on Pt photodeposition process

During the XAS synchrotron measurements, the influence of morphology on the platinum photodeposition process was studied. For this, three TiO_2 morphologies were selected: P25, nanosheets (Nsh), and bipyramidal (Bipy) particles (see Chapter 3, section 3.1.1). These TiO_2 powders were prepared as inks using the same method applied in previous experiments and were deposited on the windows of the custom-made photocatalytic cell. The samples resulting from this synthesis will be referred to as Pt_{insitu}/P25, Pt_{insitu}/Nsh and Pt_{insitu}/Bipy, respectively.

XANES spectra for three different TiO_2 morphologies (***Figure 24a-c***) show a gradual reduction of metal from Pt^{4+}, as in the precursor, to metallic Pt^0 state without formation of extra intermediates.

Interestingly, the evolution of XAS spectra was identical for the Pt_{insitu}/P25 and Pt_{insitu}/Bipy samples, while the platinum reduction spectra for Pt_{insitu}/Nsh were shifted towards lower energies, suggesting the possibility of distinct photodeposition mechanisms in the case of (101) and (001) facets of TiO_2. After photodeposition, platinum was reduced to a metallic state, according to linear combination fitting (LCF) using reference spectra of Pt foil and H_2PtCl_6 and FT-EXAFS analysis (***Figure 24 d*** and ***e***).

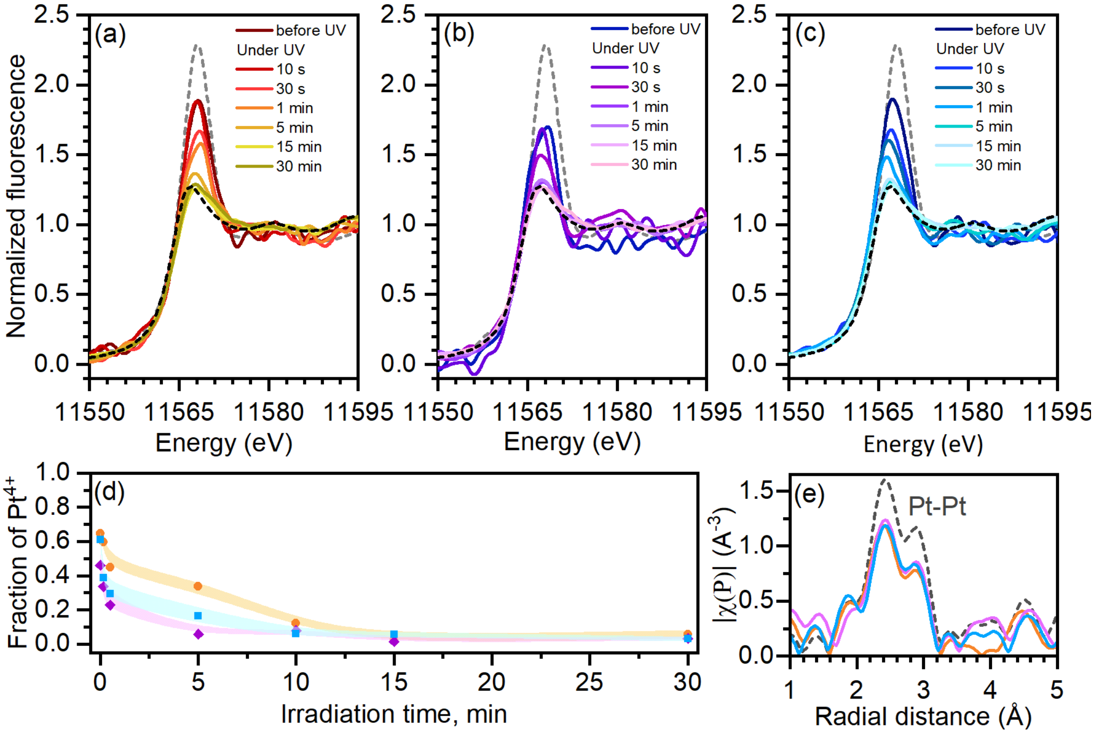

Figure 24. Evolution of Pt L_3-edge XANES spectra during UV irradiation (from dark to light) for Pt on P25 (a) Bipy (b) and Nsh (c) TiO2 morphology with reference Pt precursor (dashed grey) and Pt foil (dashed black). (c) Fraction of Pd0 obtained by LCF: the error is represented by the width of lines (e) the |FT|-EXAFS data for Pt_P25 (orange), Pt_Bipy (purple) and Pt_Nsh (blue) with reference Pt foil (dashed grey).

The coordination numbers obtained from the spectra after 30 min of irradiation are considerably lower compared to bulk platinum indicating the nanometric dimensions of the particles in all samples (***Table 1***).

Table 1. Coordination numbers for samples with different TiO_2 morphology after *in situ* photodeposition.

Sample	$CN_{Pt\text{-}Pt}$
Pt_{insitu}/P25	10.6 ± 1.0
Pt_{insitu}/Bipy	9.1 ± 1.9
Pt_{insitu}/Nsh	9.1 ± 1.5

4.6 Photocatalytic H_2 evolution over Pt/TiO_2

The second procedure during synchrotron measurements was aimed to follow the process of hydrogen production on samples synthesized *in situ*. To highlight the differences, the light was periodically switched on and off with 4 XANES spectra collected under every condition. To emphasize the contrast, all XANES spectra under UV and in the dark were merged, and the difference between the two final spectra is shown as the gray line in ***Figure 25 a-c***.

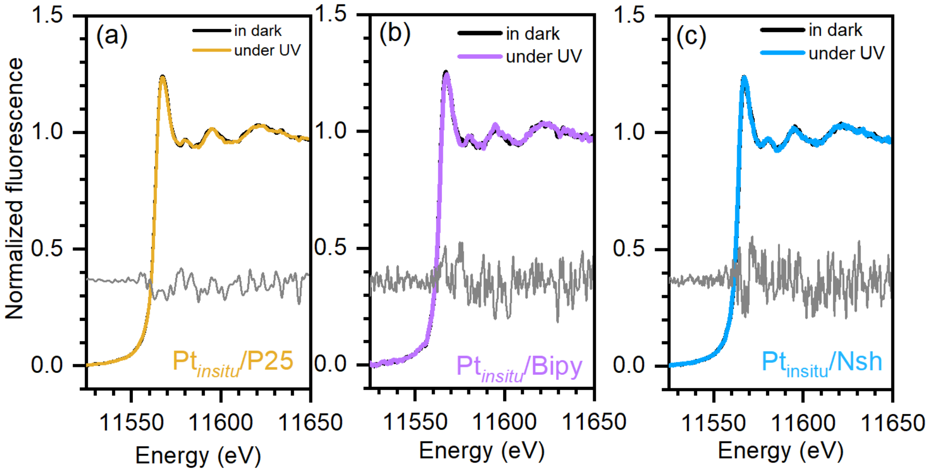

Figure 25. Pt L_3-edge XANES spectra averaged over 4 UV irradiation cycles for hydrogen production, with grey line as a difference between spectra taken in the dark and under UV irradiation for Pt_{insitu}/P25 (a), Pt_{insitu}/Bipy (b) *and* Pt_{insitu}/Nsh (c).

Regrettably, no significant difference in XANES spectra during UV irradiation and in the dark was not observed, with Pt being in metallic states in both cases.

The literature reports on tracking charge carrier dynamics for pure TiO_2 without metal co-catalysts, which typically have femtosecond resolutions and require the time-resolved XAS spectroscopy [148]. However, based on the current literature, no reports have been published on the investigation of charge carrier dynamics in metal/TiO_2 systems using XAS.

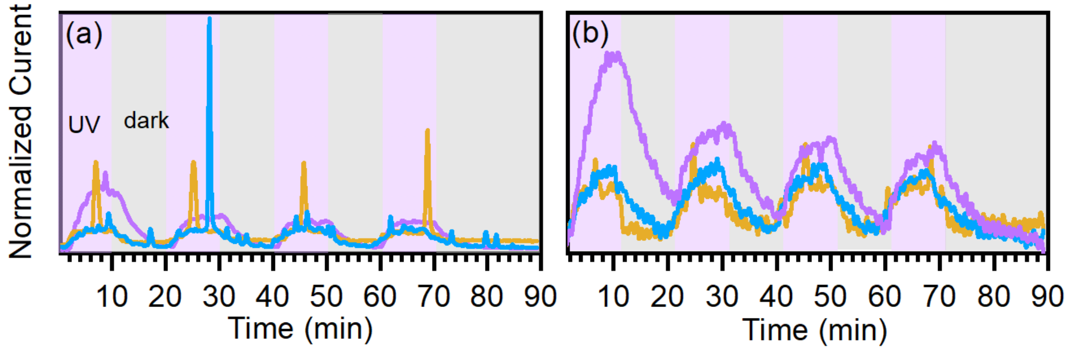

Figure 26. Mass spectroscopy data for signal (a) m/Z = 2 and (b) (m/Z = 44) divided by the signal of m/Z = 40 during H_2 evolution experiment run over the *in situ* made samples Pt_{insitu}/P25 (yellow), Pt_{insitu}/Bipy (purple) *and* Pt_{insitu}/Nsh (blue).

At the same time, the evolution of hydrogen during the UV irradiation was clearly observed (***Figure 26*a**). The decrease in H_2 production was associated with a decomposition of formic acid in the system, confirmed by the simultaneous decrease in the CO_2 signal (***Figure 26b***).

To obtain quantitative data on H_2 production, laboratory measurements using gas chromatography were performed. For this purpose, the samples were synthesized *ex situ* in laboratory in the conventional batch procedure (see Chapter 3, section 3.1.2). Samples prepared using this synthesis method will be referred as Pt_{batch}/P25, Pt_{batch}/Bipy and Pt_{batch}/Nsh corresponding to the TiO_2 powder used during the synthesis.

For laboratory batch synthesis, a nominal metal loading of 0.8 wt% was selected, as titanium dioxide was not applied as ink but was suspended in the reaction solution. This approach would presumably lead to a smaller difference between the nominal and actual metal loading and would correspond to samples synthesized *in situ* at the synchrotron.

As we have seen from the chapter “Materials and Methods” section “Synthesis of metal nanoparticles supported on TiO2”, during photodeposition, it is preferable to work in an acidic environment. Formic acid is more suitable for this purpose, as it has been shown that an acidic environment prevents the formation of platinum oxide. However, for hydrogen production reactions, methanol is more effective due to its higher hydrogen yield [149]. Methanol is also an ideal substrate for investigating the process, which justifies the significant efforts undertaken to clarify its operative mechanism. This makes methanol an excellent choice for model reactions and comparisons between different morphologies.

For all materials, a constant H_2 photoproduction vs. time was observed (***Figure 27***). The oxygen concentration was continuously monitored and remained consistently low. The ratio between H_2 and CO_2 production was approximately 1:10 (***Figure 27b***). Such a high H_2 to CO_2 ratio reflects efficient charge separation and effective water reduction to hydrogen.

Among the samples, the Pt_{batch}/P25 catalyst exhibited the highest activity, suggesting that the rate of H_2 formation is enhanced by the presence of (101) surfaces, which are known for their reducing properties. As previously discussed, when electron-hole pairs are generated, electrons tend to migrate along the (101) faces, while holes migrate towards the (001) faces. This phenomenon can be attributed to the surface heterojunction. The CB of the (101) faces is less negative than that of the (001) faces, while the VB of the (101) faces is more positive. Consequently, photogenerated electrons preferentially move to (101) surfaces, while holes migrate to (001) surfaces. Given that hydrogen production involves a reduction reaction, a higher percentage of exposed (101) faces correlates with an increased hydrogen production rate. Therefore, the Pt_{batch}/Nsh catalyst demonstrated the lowest activity among the three materials, likely due to the predominance of (001) facets.

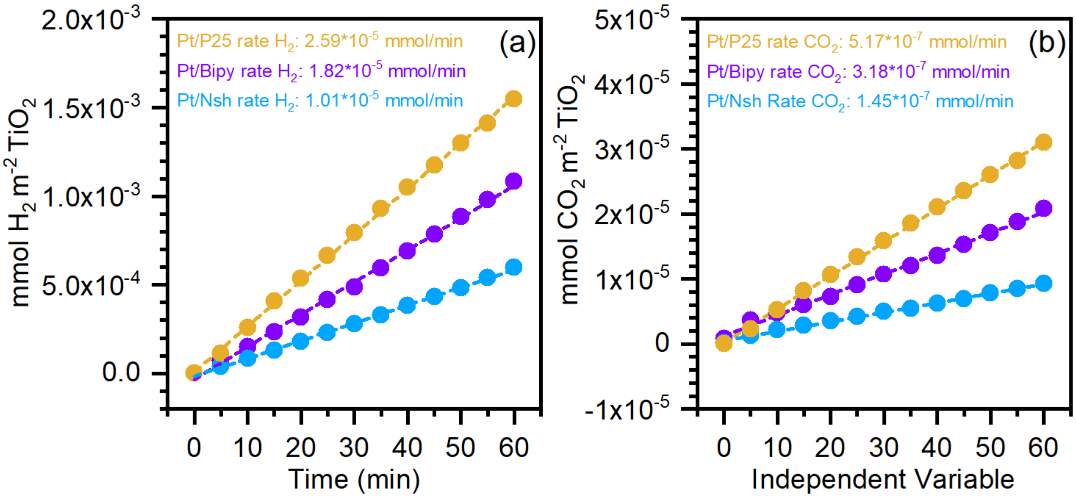

Figure 27. Formation of H_2 (a) and CO_2 (b) during PHER analyzed by GC for Pt_{batch}/P25 (yellow), Pt_{batch}/Bipy (purple) and Pt_{batch}/Nsh (blue) normalized by specific serface area for diferent TiO_2 morphologies morphologies in the presence of methanol as hole scavenger.

4.7 Impact of TiO_2 morphology on Pt surface properties

The surface of the TiO_2 was investigated at a molecular level by FTIR spectroscopy using CO as a probe molecule. CO is a versatile probe, capable of interacting with both Ti and Pt centers. Therefore, it was employed to examine the surface-active sites of different samples (described in previous section). To probe the Ti^{4+} sites, the IR experiment was conducted at low temperature (liquid nitrogen temperature). The IR spectroscopy of adsorbed CO requires pre-treatment of samples at high temperature. This treatment results in the complete desorption of H_2O molecules and in the removal of the overwhelming part of OH groups from surfaces. During the treatment, the samples were pre-treated through oxidation at 400 °C (see Chapter 3 section 3.8).

The spectrum of the sample after activation (***Figure 28a***) recorded at 70 K is characterized by a broad absorption band of low intensity in the 3500 – 3000 cm^{-1} region, attributed to the ν(OH) stretching mode, is due to the presence of strongly bound water molecules interacting via hydrogen bond. While the defined peak at

3670 cm^{-1} is due to ν(OH) vibration of surface Ti-OH groups. At 1600 cm^{-1} is also present the characteristic peak of water bending δ(HOH). Three well defined peaks appear at 2958 cm^{-1}, 2927 cm^{-1} and 2850 cm^{-1} and can be assigned to vibrational frequencies of the (-CH) group, due to the presence of organic residue from synthesis. The signals present in the region between 1600-1300 cm^{-1} are attributed to carbonates and carboxylates from the remaining organic species during the oxidation process. The spectrum of Pt_{batch}/Bipy has also an extra peak at 2345 cm^{-1} of the linearly adsorbed CO_2 due to some synthetic organic impurities trapped in internal cavities of the TiO_2 NPs that, during the activation, the increase in temperature degraded to CO_2. Below the 1200 cm-1 region, a very intense signal is present due to the vibrations of the TiO_2 framework.

The primary feature of the FTIR spectrum ***Figure 28b*** of CO adsorbed at 70 K on TiO_2 is the peak at ~2180 cm^{-1} due to CO adsorption on (101) surfaces. This peak is more intense for the P25 and Bipy structures, which have similar dominant facet (101), while it is much weaker in intensity for the Nsh sample. Another band at ~2165 cm^{-1} is ascribed to the (100) surface, present only in Bipy sample. Conversely, the band at ~2160 cm^{-1}, in a frequency range expected for CO adsorbed on Ti^{4+} sites on (001) surface, is only present in the Nsh sample. This proves that P25 and Bipy structures have dominant (101) faces, while Nsh TiO_2 exposes (001) faces as the dominant surfaces.

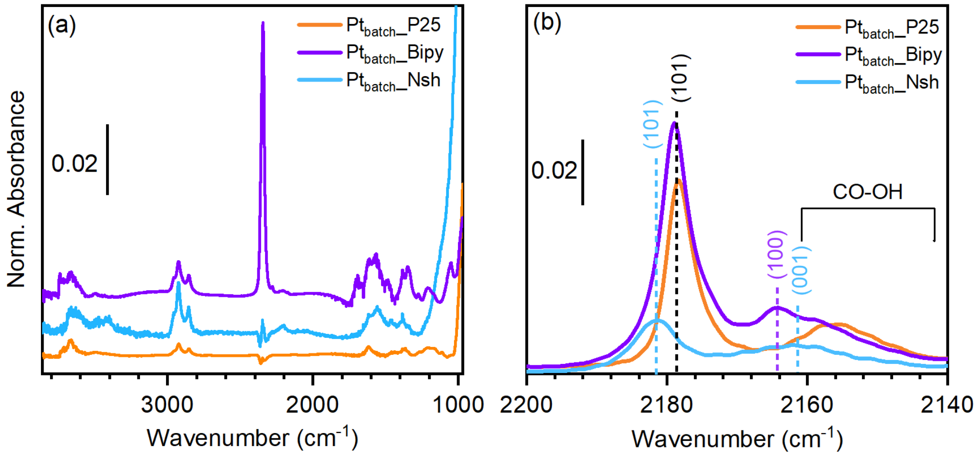

Figure 28. (a) IR spectra before sending CO at 70 K right after oxidation at 400°C. Spectra normalized to the optical density of the pellet and after beasline substruction. (b) IR spectra of CO absorbed 30 min (P_{CO} = 5 mbar). The spectrum of the sample before dosing CO was subtracted from all the others. The spectra are normalized to the optical density of the pellet.

This observation is particularly significant, as previous studies shown that Pt nanoparticles are expected to form mainly on the (101) surfaces of TiO_2 nanocrystals during UV light exposure [150, 151]. This occurs because, when UV light irradiate TiO_2, electrons tend to move to the (101) surfaces, while positive charges (holes) move to the (001) surfaces. This charge separation facilitates the reduction of Pt^{4+} to Pt^0 on the (101) surfaces. Once some Pt nanoparticles begin to form, they attract more electrons, accelerating the redaction of neighboring Pt ions and leading to the growth of small Pt clusters around the initial nanoparticles. Consequently, Pt is selectively deposited on the (101) faces of TiO_2 Nsh despite the limited exposure degree of these faces. This conclusion is supported by the results of X-ray absorption spectroscopy, which show a different trend in the deposition of Pt on Nsh TiO_2.

As expected, FTIR spectra of adsorbed CO on these samples at room temperature, which allowed to probe Pt sites and not Ti, demonstrate significant differences between Pt_{batch}/Nsh compared to Pt_{batch}/P25 and Pt_{batch}/Bipy (***Figure 29***).

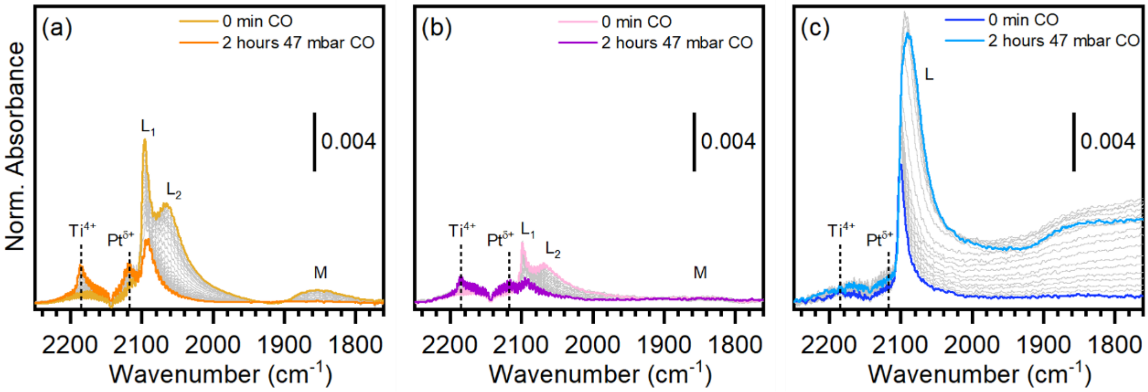

Figure 29. Evolution of IR spectra of CO upon increasing contact times up to 2 hours (P_{CO} = 47 mbar) absorbed at room temperature on Pt_P25 (a), Pt_Bipy (b) and Pt_Nsh previously oxidized at 400 °C. The spectrum of the sample before dosing CO was subtracted from all the others. The spectra are normalized to the optical density of the pellet.

The signal around ~2180 cm^{-1}, attributed to CO on (101) Ti^{4+} sites, is more intense for Pt_{batch}/P25 and Pt_{batch}/Bipy samples, due to the high regularity of the anatase (101) facets, which are characterized by an excellent crystallinity. This observation is in agreement with previous FTIR results [152]. In general, these signals are relatively weak because of the low binding energy of CO on Ti^{4+} cations, which results in low CO coverage on TiO_2 surfaces during room temperature adsorption.

Regarding the spectral features associated with the interaction between CO and Pt sites, the initial IR spectrum intensity is significantly higher for Pt_{batch}/Nsh sample. This may be due to smaller particles, which are in contradiction with the same average Pt particle size, obtained from the coordination number of Pt-Pt atoms. This suggests that this behavior was caused by some factor which preventing the interaction between Pt and CO, possibly due to the interaction of the substrate with platinum nanoparticles.

The band at ~2090 cm^{-1} along with its shoulder at ~2070 cm^{-1} is attributed to linear carbonyls on metallic platinum with high coordinated (e.g., terrace sites) and low coordinated (e.g., corner sites) Pt atoms [153]. Additionally, the weak broad band at ~1850 cm^{-1} is associated with bridged Pt^0–CO–Pt^0 species. The higher proportion of well-coordinated sited in the Pt$_{batch}$/P25 and Pt$_{batch}$/Bipy samples indicates a stronger bond with Pt on the TiO$_2$ carrier.

It is also noteworthy, that the presence of a group of signals around ~2120 cm^{-1}, attributed to Pt$^{\delta+}$–CO species, is observed only in the Pt$_{batch}$/P25 and Pt$_{batch}$/Bipy samples. These Pt$^{\delta+}$-CO species are sensitive to charge transfer nearby the Pt sites [154]. In previous studies, these signals have been associated with strong metal-support interactions [152, 155].

4.8 TiO$_2$ morphology effect on metal-support interaction

To investigate in more detail the different behavior of the samples potentially associated with the metal-carrier interaction, an experiment with temperature-controlled oxidation and reduction was conducted. The SMSI effect is commonly observed in metal NPs supported on reducible metal oxide carriers in a reducing atmosphere [156-162]. It has been recognized that SMSI can also occurs following vacuum treatments [163]. under oxidizing environments [164-166], and after the photodeposition of metal particles [77, 167].

Therefore, the Pt$_{batch}$/P25, Pt$_{batch}$/Bipy and Pt$_{batch}$/Nsh samples were studied under both reducing and oxidizing conditions using XAS, to examine the effect of morphology on formation on SMSI formation. Additionally, a sample with a higher metal loading of 2% was included to evaluate the potential influence of nanoparticle size on the SMSI effect. The samples are referred to as 2%Pt$_{batch}$/P25, 0.8%Pt$_{batch}$/P25, 0.8%Pt$_{batch}$/Bipy and 0.8%Pt$_{batch}$/Nsh, depending on the substrate and metal loading.

The as-synthesized samples exhibit significant differences in the average oxidation state, as determined by XANES spectroscopy (***Figure 30a***).

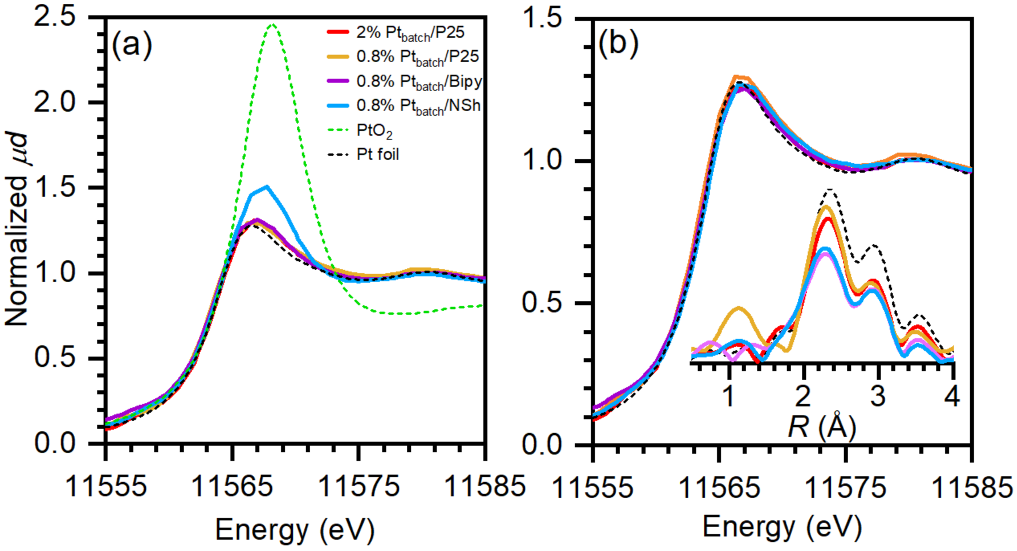

Figure 30. XANES spectra of Pt_{batch}/TiO_2 as synthesized (a) and H_2-reduced at 150 °C (b), compared to PtO_2 (dotted green) and Pt foil (dashed black) references. The inset in part (b) shows the |FT|-EXAFS data.

The 0.8%Pt_{batch}/Nsh sample was partially oxidized, with a Pt^{4+} fraction of 0.23 ± 0.018, determined by linear combination fitting (LCF) using reference spectra of Pt foil and PtO_2, while samples on other TiO_2 supports have just 4% Pt^{4+} fraction. Reductive treatment in H_2 at 150 °C ((see Chapter 2 section 3.2.2) completely reduces all samples to Pt^0 states (***Figure 30b***).

Using *in situ* XANES, the changes in the local atomic and electronic structure of the Pt phase during oxidation were monitored (***Figure 31***). The reduced samples were heated in O_2 atmosphere from 50 to 400 °C and maintained at this temperature for 25 min (see Chapter 2 section 3.2.2). The 0.8%Pt_{batch}/Nsh sample was subject to oxidation with a Pt^{4+} fraction of 0.15 ± 0.01 (***Figure 31d***) but it did not reach the same oxidation state as it had immediately after synthesis (***Figure 31e***). In contrast, the 2% Pt_{batch}/P25 sample did not undergo any oxidation, even at the maximum temperature of 400 °C.

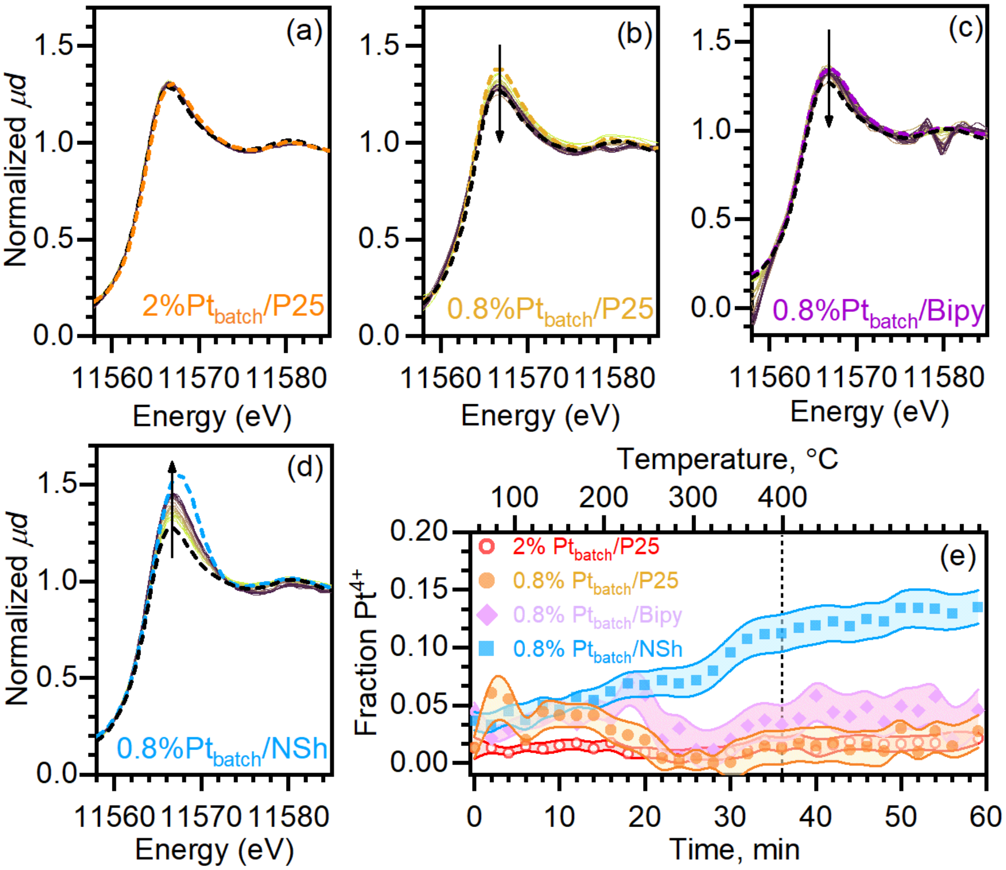

Figure 31. Evolution of XANES spectra for Pd/TiO$_2$ samples (a-f from green to brown) in O$_2$ from 50 to 400 °C with dashed lines for XAS spectra for samples as synthesized and Pt foil (dashed black), and (f) fraction of Pt^{4+} obtained by LCF. The line width is proportional to the error bars.

Interestingly, a similar sample with a lower metal loading 0.8%Pt$_{batch}$/P25 along with 0.8%Pt$_{batch}$/Bipy exhibited an unusual behavior. During heating, the intensity of the white line decrease, indicating sample reduction, followed by slow and weak oxidation that began only after reaching 400 °C, as confirmed LCF analysis (***Figure 31e***).

Such behavior is unusual for nanoparticles of deposited metals and may be attributed to the fact that in these two samples, as in 2%Pt$_{batch}$/P25, there was no direct interaction with oxygen. Instead, the reduction occurs due to the exchange of electrons between the substrate and the metal during high temperature treatment, suggesting the presence of strong metal-support interaction [168].

These findings, together with the FTIR data, confirm the presence of SMSI when platinum nanoparticles are photodeposited onto P25 and Bipy TiO_2. The dominant (101) surface in these titanium dioxide morphologies serves as a site for electron accumulation during UV irradiation, subsequently initiating the formation of Pt NPs with enhanced metal-substrate interaction. This SMSI effect facilitates the donation of electrons from the support material to the platinum, thereby weakening the bonding of oxygen molecules on the platinum surface.

4.9 Structure and shape of Pt NPs on TiO_2.

The samples synthesized both *in situ* and in a laboratory reactor, were analyzed using high-resolution transmission electron microscopy, as shown in ***Figure 32***. The three TiO_2 morphologies exhibited forms consistent with descriptions in the literature [30, 31]. Additionally, Bipy TiO_2 displayed a cavity within its structure, which aligns with expected synthesis outcomes (see Materials section).

Pt particles on titanium dioxide substrates with P25 and Bipy morphologies were relatively flat and exhibited a tendency to agglomerate, deviating from previous findings [31]. In contrast, nanoparticles on Nsh type of TiO_2 were more spherical, with isolated nanoparticles observed more frequently. This observation was quantified using the *Roundness Parameter*, defined as $4 \times \frac{[Area]}{\pi \times [\text{Major axis}]^2}$, where *Area* is the area of the ellipse used to highlight the nanoparticle and *Major* axis is its longer axis. A *Roundness Parameter* value of 1.0 indicates a perfect circle. The samples Pt/P25 and Pt/Bipy had *Roundness* valu6 es around 0.82, while for Pt/Nsh the averaged value of roundness was approximately 0.9. This deviation in shape may be attributed to the higher nominal loading compared to that used in previous reports.

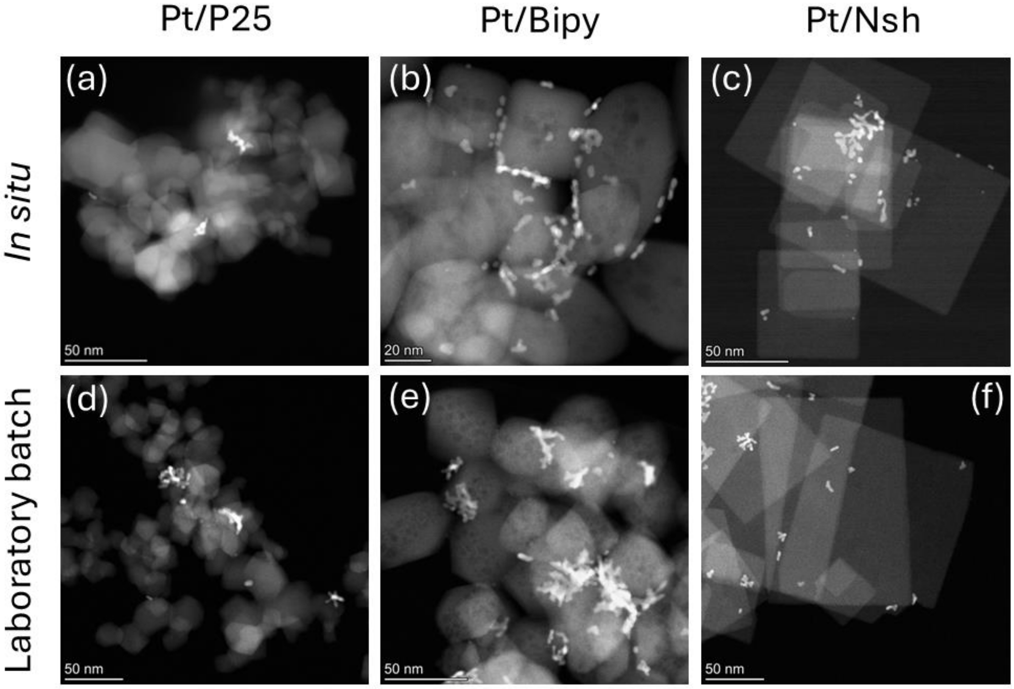

Figure 32. HAADF-TEM images of *in situ* synthesized samples (a) Pt_{insitu}/P25 (b) Pt_{insitu}/Bipy (c) Pt_{insitu}/Nsh with nominal metal loading of 2 wt.%. compared with batch synthesized (c) Pt_{batch}/P25, (d) Pt_{batch}/Bipy, (e) Pt_{batch}/Nsh with nominal metal loading of 0.8%.

Nanoparticle size distributions were derived from *Area* measurements, applying the formula for the diameter of the spherical particle. Larger 'coral'-shaped agglomerates were excluded from this analysis, focusing solely on individual nanoparticles. Pt NPs synthesized in the laboratory batch across all samples exhibited an average size of 3.5 ± 0.8 nm, while slightly smaller sizes were observed for samples synthesized *in situ* as shown in ***Figure 33*** (though insufficient particles were available for the Pt_{insitu}/P25 sample to allow the size analysis). The observed particle size distributions align with XAS results, supporting consistency in nanoparticle sizing across different TiO_2 morphologies.

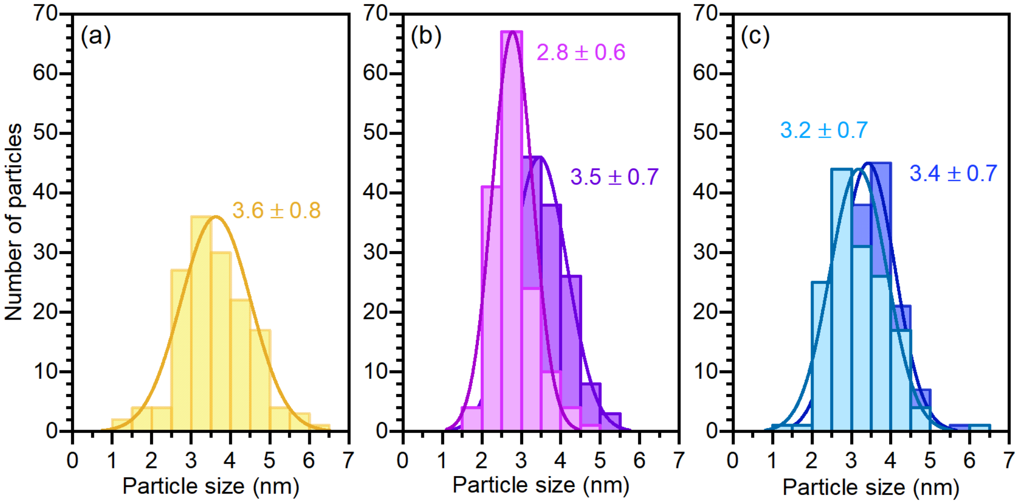

Figure 33. The size distributions obtained from HR-TEM images for (a) Pt_{batch}/P25 (b) $\mathrm{Pt}_{in\ situ}$/Bipy (pink) and Pt_{batch}/Bipy (purple) (c) $\mathrm{Pt}_{in\ situ}$/Nsh (light blue) and Pt_{batch}/Nsh (dark blue).

HR-TEM analysis revealed that Pt agglomerates, which were formed regardless of the metal loadings and tended to form around a central particle, with growth occurring progressively outward (***Figure* 34**). Moreover, Pt nanoparticles exhibited a preference for deposition on the TiO_2 faces rather than on the edges.

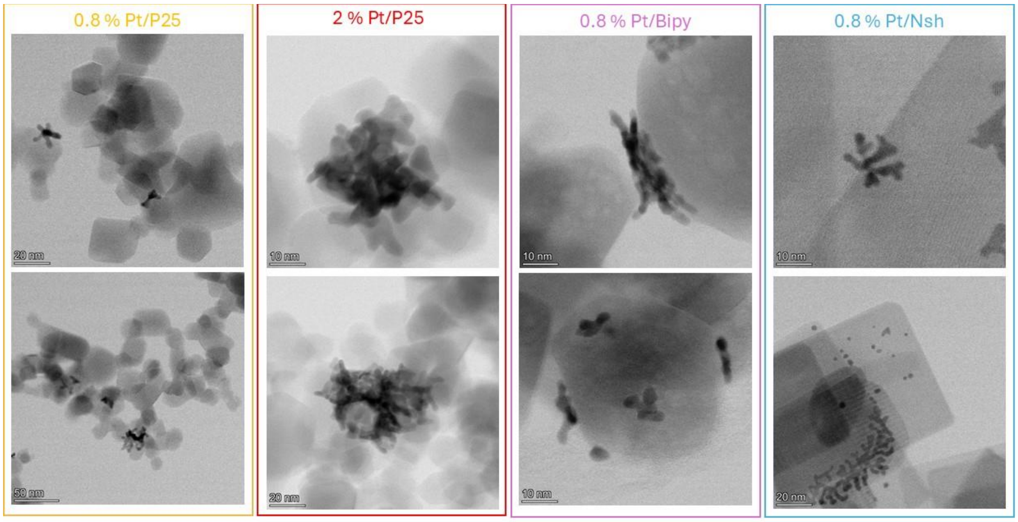

Figure 34. BF-TEM images Pt/P25 with 0.8% and 2% loading (yellow and red) Pt/Bipy (purple) Pt/Nsh (blue).

It is noteworthy that the oval shape of nanoparticles may suggest a stronger interaction between the substrate and metal nanoparticles, ultimately influencing the redox properties observed in the previous section. However, samples with presumably SMSI, as evidenced by TEM and XAS (specifically Pt/P25 and Pt/Bipy), displayed a higher number of agglomerates and clustered nanoparticle structures, which undoubtedly affect particle interaction with oxygen.

While the overall results are closely aligned, some differences in TEM images are notable. For instance, Pt NPs on Nsh differ in morphology, likely due to the dominance of the (001) facet in this morphology, which influenced both the photodeposition of platinum and hydrogen production. This leads to the conclusion that the nanoparticles favor localization on the (101) surface of TiO_2 due to the reductive nature of this face. The balance between the (101) and (001) surfaces allow for the presence of a “surface heterojunction,” which enhances the reactivity of the (101) surface with the co-catalyst deposited on it. Thus, despite the presence of agglomerates that might initially appear to reduce photocatalytic activity, the Pt/P25 sample demonstrated the highest efficiency in hydrogen production, underscoring the critical role of surface orientation and metal-support interaction in optimizing catalytic performance.

4.10 Summary

The chapter demonstrate the experimental and methodological advances for *in situ* and *operando* studies of photocatalysts at the laboratory and synchrotron facilities, employing a combination of X-ray absorption spectroscopy, optical spectroscopy and mass spectrometry to elucidate the photodeposition process of Pt on TiO_2 support and subsequent hydrogen evolution reaction over the formed Pt/TiO_2 catalysts. Complimentary and extended research utilizing synchrotron sources highlights the importance of the TiO_2 particle shape and their effect on the Pt photodeposition and photocatalytic hydrogen production. This understanding is crucial for optimizing photocatalysts through adjustment in the synthesis procedure, aiming to tuning the properties of Pt/TiO_2 systems for various applications.

The results provide valuable insights into the formation and evolution of Pt/TiO_2 photocatalysts and propose an effective multi-technique approach for *in situ* and *operando* studies at both laboratory and synchrotron scales, for the development of photocatalyst aimed for hydrogen production.

5 *In situ* photodeposition of palladium particles on TiO_2

In the previous chapter, combination of laboratory and synchrotron X-ray absorption spectroscopy, UV-Vis spectroscopy and mass spectrometry were utilized to investigate catalyst formation and photocatalytic H_2 production over Pt/TiO_2. This chapter employs a similar *in situ* approach for Pd/TiO_2 based photocatalyst using an enhanced custom-made photocatalytic cell. The nucleation stages of Pd on TiO_2 samples are monitored using synchrotron XAS and complemented by HAADF-TEM microscopy. Two Pd/TiO_2 samples were examined: one prepared *in situ* in photocatalytic cell, and the other synthesized using a conventional batch reactor with suspended TiO_2.

As discussed in Chapter 2, the limited amount of sample in photocatalysis and/or dimensions of the cell are typically imposing constrains on XAS data collection, which is usually incompatible with transmission geometry. In Chapter 4 this issue was solved by measuring of the samples in fluorescence mode, where the catalyst was deposited on the window of a photocatalytic cell. In this chapter, efforts were made to further improve the cell to enable XAS data collection in both fluorescence and transmission modes due to high penetration depth of X-rays aat Pd *K*-edge. Thus, the configuration of custom-made photocatalytic cell was modified and the length of the main cell body was increased. The windows were oriented perpendicularly to the incoming X-ray beam, allowing the collection of both fluorescence and transmission signals (***Figure 35a***). The cell was placed between the first and second ionization chambers, with a Pd metallic reference foil placed between the second and the third chambers for energy calibration. This cell design allowed to perform measurements of Pd/TiO_2 catalyst dispersed in the volume of the cell. However, the main results presented in this chapter focus on the systems with the catalyst deposited on the window, as in case of Pt, and measured in fluorescence mode, with the transmission signal giving some complementary information on Pd concentration and speciation in the liquid phase.

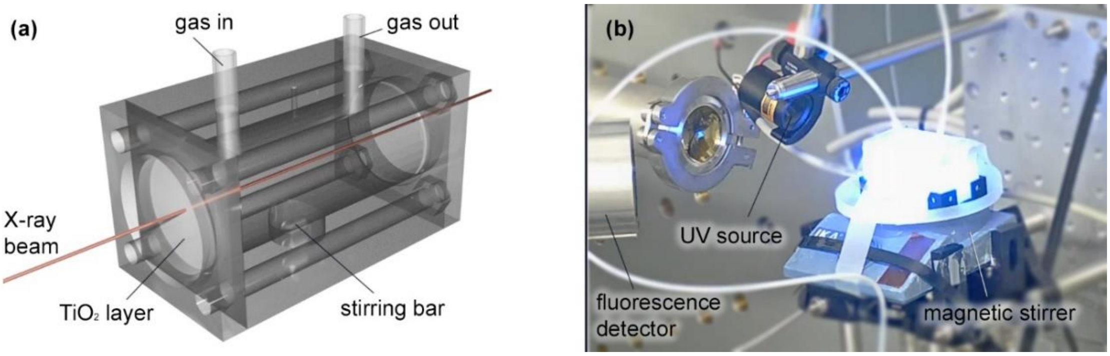

Figure 35. Schematic (a) and photo (b) of the *operando* photocatalytic cell employed at the NOTOS beamline at ALBA synchrotron (Spain).

The standard experimental procedure involved repeating the synthesis using the previously utilized cell, where a thin layer of P25 TiO_2 was applied on the front cell window. The cell was then filled with a solution of Pd-precursor under continuous stirring and flushing with helium. The UV radiation was applied from the outside of the cell to the front window by setting the irradiance to 400 W/m^2. The cumulative irradiation times were 10 s, 30 s, 1 min, 5 min, and 20 min, as previously conducted for Pt. The progressive growth and evolution of Pd species on TiO_2 during UV irradiation were monitored using XAS in fluorescence mode from the same side as UV source, with simultaneous XAS data collection in transmission mode to track changes of Pd species in the reaction solution.

To reduce the beam effects observed during beam damage tests from Pt/TiO_2 study (see Chapter 4 section 4.4), the cell was automatically moved horizontally by 0.5 mm (and when the row is finished, by 0.5 mm vertically) after each XAS spectrum acquisition (see ***Figure 36***). This procedure limited the maximum exposure of any fraction of the sample to the X-ray beam to approximately 1 minute and ensured that no palladium nanoparticles were formed on the window in the absence of UV light.

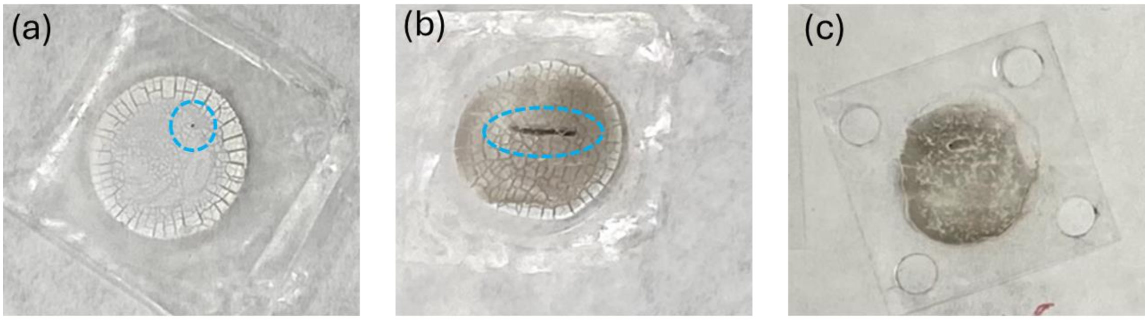

Figure 36. Picture of samples during Pd photodeposition on TiO_2 after the contact with X-ray beam (a) XAS data collection in one spot without UV irradiation, (b) XAS data collection during UV irradiation, while adjusting the movement along the sample to reduce beam effect (c) Final approach used for XAS data collection under UV.

5.1 Evolution of Pd species during photodeposition on TiO_2 monitored by XAS

Figure 37 shows the evolution of XANES and EXAFS data from fluorescence signal indicating a gradual formation of metallic Pd species, as compared to the reference Pd foil. The photodeposition process was accompanied with progressive formation of distinct XANES features, characteristic of metallic Pd, a decrease of the first-shell Pd–Cl contribution in EXAFS and a growth of the Pd–Pd one. Due to the nanometric dimensions, the intensity of the latter was smaller with respect to the Pd reference foil. The average Pd–Pd coordination number obtained through EXAFS fitting was 7.9 ± 0.8, corresponding to an average particle size of *ca*. 1.2 nm, assuming their *fcc*-like structure.

The transmission XANES signal (***Figure 38a***) was challenging to analyze due to the small edge jump at Pd *K*-edge, however the decrease of this signal over time due to consumption of homogenously distributed Pd-species from the liquid phase allowed to quantitatively follow the kinetics of the photodeposition (***Figure 38b***). This is explained by the fact that, as Pd began to deposit on the TiO_2 layer, which was inhomogeneous both in its thickness and distribution over the window, this inhomogeneity led to lower edge jump.

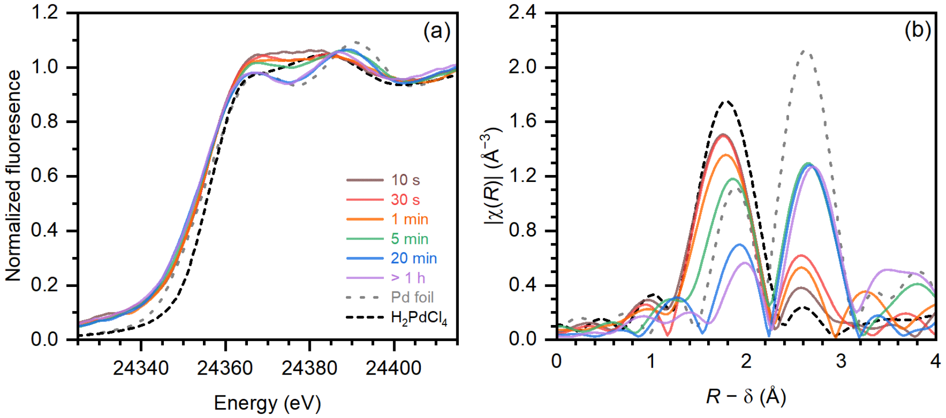

Figure 37. XANES (a) and phase-uncorrected FT-EXAFS (b) data taken in fluorescence mode collected during *in situ* photodeposition of palladium on TiO_2. Colored lines correspond to different irradiation times. Dashed black and grey lines correspond to the reference H_2PdCl_4 and Pd foil, respectively.

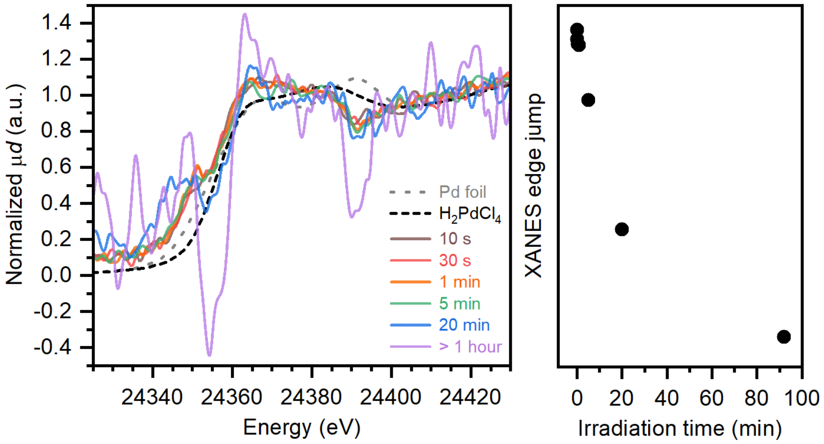

Figure 38. The same sample and data collected during *in situ* photodeposition of palladium on TiO_2 that in previous figure, but XANES was recorded in transmission mode. (b) Relative changes in the Pd loading on TiO_2 as a function of irradiation time estimated based on the decrease of the Pd edge-jump in XAS signal due to inhomogeneities of the TiO_2 layer.

Notably, after only 10 s of the UV irradiation, the position of the edge in XANES, collected in fluorescence mode, corresponded to the oxidation state of Pd^0 (***Figure 37a***). Moreover, this spectrum could not be reproduced by a linear combination of the reference spectra of H_2PdCl_4 (the spectrum of this reference was identical to that of the precursor as shown in ***Figure 39a***) and Pd foil, which is evidenced by the absence of isosbestic points in these spectra. This observation provides critical insight into the formation mechanism of Pd/TiO_2 catalyst, suggesting that the photoreduction of Pd initiated with the formation of isolated Pd^0 species, followed by a subsequent growth of Pd nanoparticles, most likely around those initial Pd^0 sites.

The signals for H_2 and CO_2, resulting from the decomposition of formic acid were observed in mass spectrometry data (***Figure 39b***) during each UV illumination.

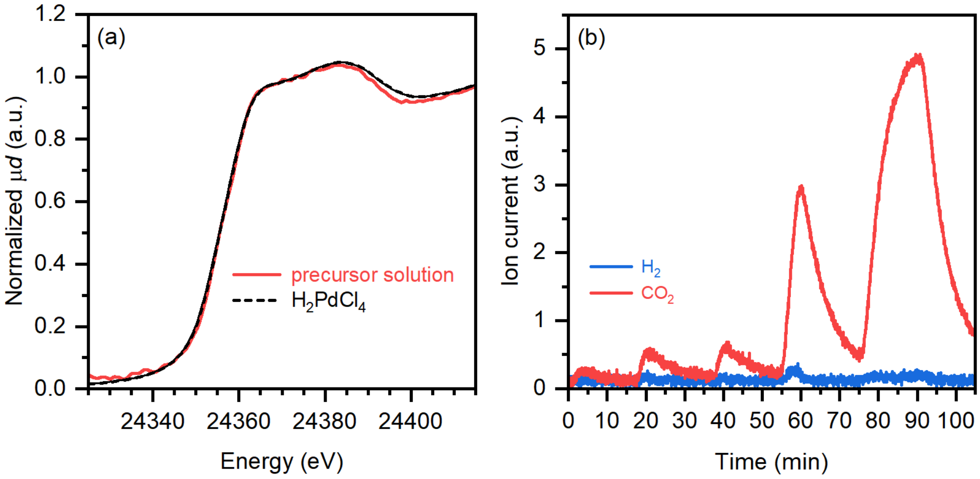

Figure 39. (a) XANES spectra of the solution of palladium precursor, measured in transmission mode, compared with the H_2PdCl_4 reference, (b) mass spectrometry data for m/Z ratios of 2 (blue) and 44 (red) collected during *in situ* photodeposition of palladium.

The average Pd–Pd interatomic distance in the formed nanoparticles was 2.81 ±0.01 Å, which is significantly higher than the value of 2.74 ±0.01 Å determined for Pd foil. The shaping of XANES spectra, specifically the positions and the relative intensities of the first two maxima, indicated that such elongation was caused by the formation of palladium hydride [169, 170], while the presence of carbide like phase was unlikely [112, 171].

The sample prepared through conventional batch synthesis was also investigated. It was applied to the window of the photocatalytic cell in a similar way, as pure TiO_2. The average Pd–Pd coordination number for this batch-synthesized sample was higher (11.6 ± 0.6) indicating that bigger particles were present. Upon the addition of the formic acid solution, the typical XANES features of palladium hydride also appeared (***Figure 40a***) and the average Pd–Pd interatomic distances increased from 2.73 ±0.01 Å to 2.84 ±0.01 Å, which is visually evidenced in ***Figure 40b***. The greater elongation of the interatomic distance upon formation of palladium hydride phase for this sample, compared to the one generated *in situ*, correlates with the assumption of a larger particle size. Notably, the hydride features in XANES and increased Pd–Pd distances remained even after the solution was removed.

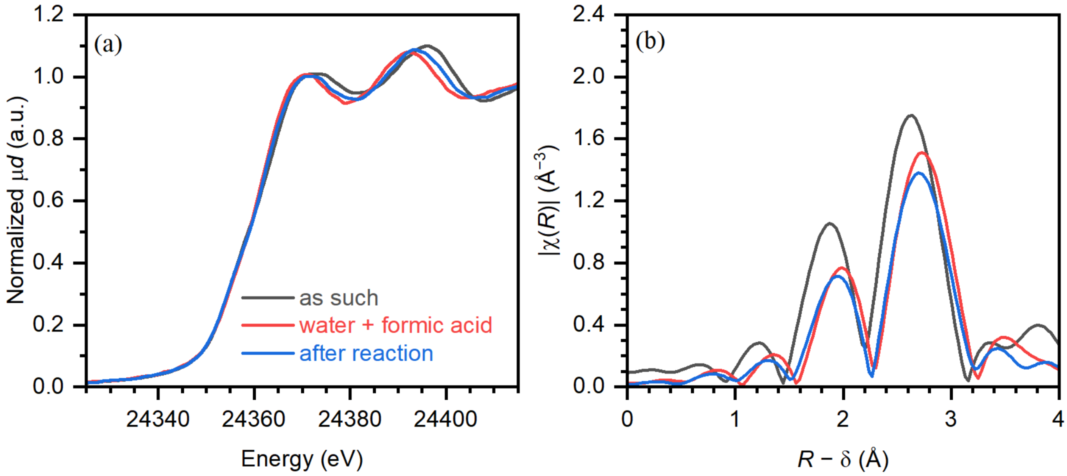

Figure 40. XANES (a) and phase-uncorrected FT-EXAFS (b) data for the sample, synthesized using conventional batch procedure, in the initial state (black), after addition of water and formic acid to the photocatalytic cell (red) and after performing UV irradiation and removing the liquid (blue).

5.2 Morphology of Pd/TiO_2 samples

The series of Pd/TiO_2 samples were investigated using HAADF-STEM. The samples prepared *in situ* and collected from the window of the photocatalytic cell after XAS investigation will be referred to as Pd_{insitu}/TiO_2 and the sample synthesized in the conventional batch procedure as Pd_{batch}/TiO_2.

As evident from ***Figure 41*** and ***Figure 42*** and additional micrographs, the *in situ* generated sample exhibited homogenous distribution of palladium over TiO_2 with a narrow particle size distribution centered around 1 nm (***Figure 41c***), in agreement with EXAFS data. In contrast, a very inhomogeneous distribution of Pd was observed for Pd_{batch}/TiO_2. This sample had bigger particles, which correlates with EXAFS results, and broader particle size distribution (***Figure 42c***).

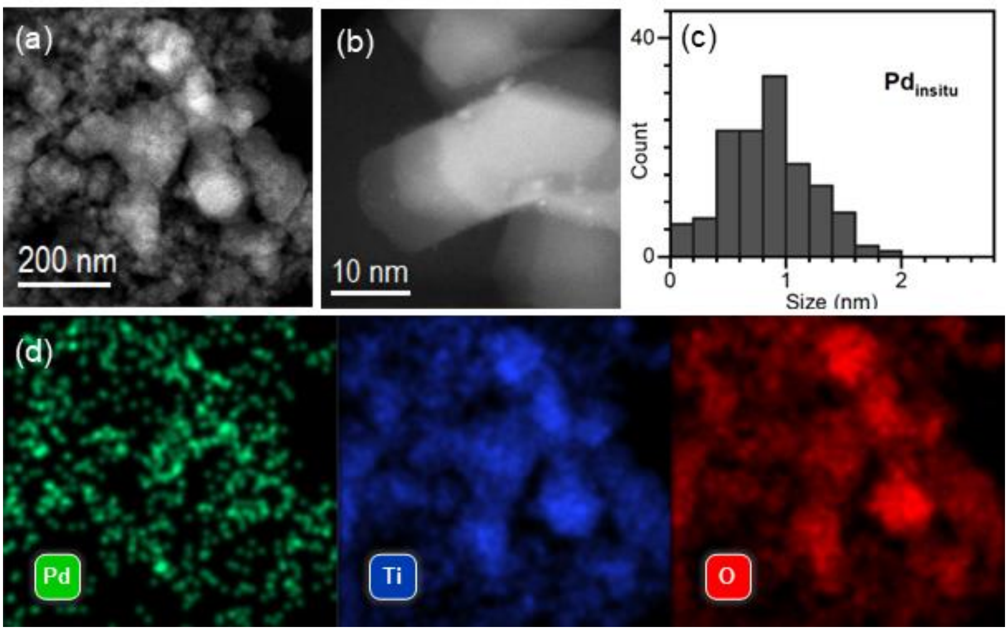

Figure 41. STEM characterization of Pd_{insitu} sample. Low (a) and high (b) magnification HAADF-STEM images. (c) Histogram of Pd particle size distribution. (d) EDX elemental maps corresponding to the area shown in part (a).

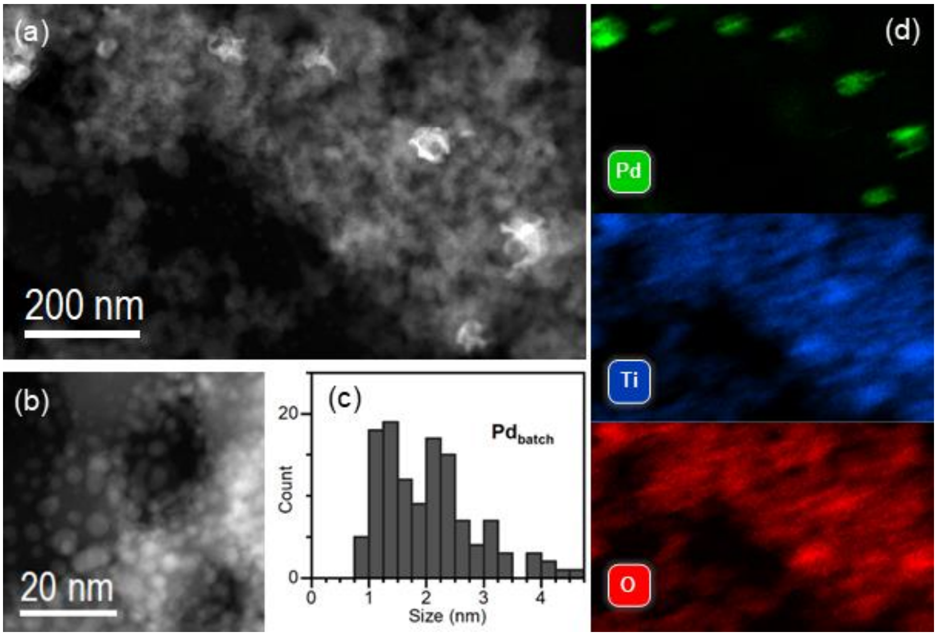

Figure 42. STEM characterization of Pd$_{batch}$ sample. Low (a) and high (b) magnification HAADF-STEM images. (c) Histogram of Pd particle size distribution. (d) EDX elemental maps corresponding to the area shown in part (a).

Moreover, particles or particle agglomerates with sizes up to 100 nm were detected, which were almost absent for Pd$_{insitu}$/TiO$_2$ (***Figure 43***).

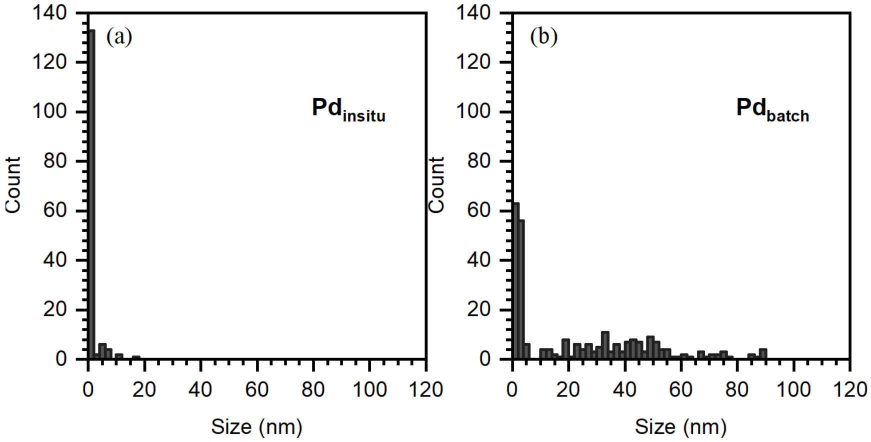

Figure 43. Histograms of particle size distribution for Pd$_{insitu}$/TiO$_2$ (a) and Pd$_{batch}$/TiO$_2$ (b) in a wider range with respect to Figure 6 of the main text.

To gain further insights, it was decided to return to studying the sample under different irradiances (as was made for Pt in Chapter 4 section 4.4). Two additional samples that were generated *in situ* during XAS experiments following a similar procedure as for Pd_{insitu}/TiO_2 but using a lower irradiance of 80 and 200 W/m^2. Unfortunately, a smaller degree of Pd incorporation into TiO_2 limited the interpretation of XAS data (***Figure 44a***), although, the presence of Pd^0 species could be unambiguously detected for the sample generated with 200 W/m^2 irradiation, based on XANES spectra. HAADF-STEM data of these samples highlighted the presence of ultra-small Pd clusters (< 1 nm) or single-atom Pd-sites (***Figure 44b***), confirming the photodeposition mechanism proposed in the previous section.

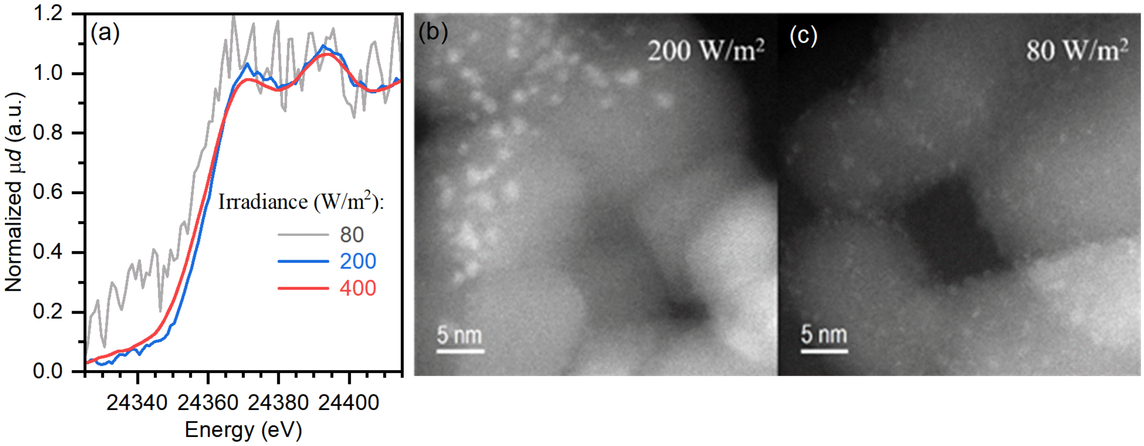

Figure 44. (a) XANES spectra of *in situ* generated samples after 20 min of UV illumination with different irradiance (400, 200 and 80 W/m2) and HAADF-STEM images *in situ* samples generated with UV 200 (b) and 80 W/m2 (c) irradiance.

Bigger particles obtained for Pd_{batch}/TiO_2 can be explained by the fact that part of Pd was reduced in the liquid phase, acting as nucleation centers that facilitated the growth of larger particles that were then deposited on TiO_2. This correlates with recent study, in which I was involved, on Pt-based samples [172], where photoinduced Pt reduction and formation of Pt nanoparticles were observed even in the absence of TiO_2. Conversely, in Pd_{insitu}/TiO_2, the interaction of the solution with UV light was minimized since the radiation was mainly absorbed by the TiO_2 layer. Thus, photoexcited TiO_2 could act by providing the binding sites for Pd^0 single atoms while the maximum particle size could be limited due to the interaction with the support.

5.3 Summary

In situ XAS spectroscopy, complemented by HAADF-STEM data, revealed the formation of either single-atom Pd^0 sites or ultra-small Pd^0 clusters immediately after the photodeposition of Pd species on TiO_2. These initial Pd^0 species subsequently acted as nucleation sites for the growth of nanometer-sized Pd particles. The state of Pd in the presence of water and a hole scavenger (formic acid) was identified as Pd hydride.

This approach, employing the generation of the Pd/TiO_2 sample using TiO_2 immobilized on the front window of the photocatalytic cell, can be utilized not only to investigate the properties of the catalyst but also as an alternative synthesis procedure. It facilitates the production of a homogeneously distributed Pd over the photoactive support, with a narrow particle size distribution.

6 Origin and impact of strong metal-support interaction in Pd/TiO_2 catalysts on structural and redox properties

In the case of Pd/TiO_2, the study was also conducted to investigate the strong metal-support Interaction effect, like what was investigated for the Pt/TiO_2 samples. However, the focus was not on the difference of TiO_2 morphology, but rather on the role of synthesis procedure. This approach was chosen due to the use of several *in situ* experimental methods, including XAS, IR and EPR spectroscopy with environmental high-resolution scanning transmission electron microscopy (HR-STEM). These techniques are both time-consuming and costly, making it impractical to analyze a large number of samples. Therefore, in addition to the Pd/TiO_2 sample synthetized in conventional batch under laboratory condition (as studied in previous chapter), two distinct synthesis methods were applied: photodeposition and deposition-precipitation (for more details see Chapter 3 section 3.1.2). To distinguish between the samples, the terms "Pd_photo" (synthesized via photodeposition) and "Pd_dep" (synthesized via deposition-precipitation) are used, emphasizing the difference in their synthesis methods.

The investigation of the SMSI effect in Pd/TiO_2 was expanded beyond the scope presented for platinum (Chapter 4). This was possible due to support from the ReMade@ARIE project, funded by the European Union as part of the Horizon Europe call HORIZON-INFRA-2021-SERV-01 (grant agreement number 101058414), which enabled a more detailed study of the origin of the SMSI effect.

6.1 The structure of Pd/TiO_2 samples after the synthesis

To focus on the role of SMSI, two Pd/TiO_2 samples were synthesized by keeping constant the support (TiO_2 P25, supplied by Evonik) and the nominal metal loading (2 wt%).

According to *in situ* photodeposition study of Pd on TiO_2 (Chapter 5), the expected mechanism for this synthesis involves the adsorption of the Pd precursor at the TiO_2 surface in water solution, followed by its reduction to Pd^0 by photogenerated electrons in presence of methanol as hole scavenger, what also was reported in literature [173, 174]. While for a new sample Pd_dep the processes of the deposition-precipitation, instead, involves the precipitation in water solution of Pd oxide/hydroxide (using Na_2PdCl_4 as precursor and Na_2CO_3 as precipitating agent) and its precipitation on TiO_2 [175] followed by reduction in liquid phase by HCOONa to Pd NPs [176]. Sample without reduction step was named as Pd_dep(NR).

Both samples were then investigated by XANES spectroscopy. And first observation was the actual Pd loading after photodeposition is ca. 1 wt.%, determined by the edge jump in XAS spectra. Moreover, the two samples exhibited significantly different average oxidation state, as shown by the XANES spectra of Pd_dep and Pd_photo with those of Pd foil and PdO references (***Figure 45s***).

As expected Pd_dep(NR) was in oxidized state right after the synthesis (***Figure 45***), however despite the reduction step applied during the synthesis, Pd_dep was also partially oxidized, with a Pd^{2+} fraction of 0.53 ± 0.02, determined by LCF analysis using reference spectra of Pd foil and PdO. In contrast, the Pd^{2+} fraction in Pd_photo was only 16 %, which may correspond to the surface layer of oxygen. The oxidation of similarly synthesized samples while they were exposed to air were previously reported on various supports [177, 178]. Therefore, the high fraction of Pd^{2+} for Pd_dep sample for metal nanoparticles indicates the surface and subsurface oxidation. In contrast, the Pd^{2+} fraction in Pd_photo was much lower than expected for passivated Pd NPs.

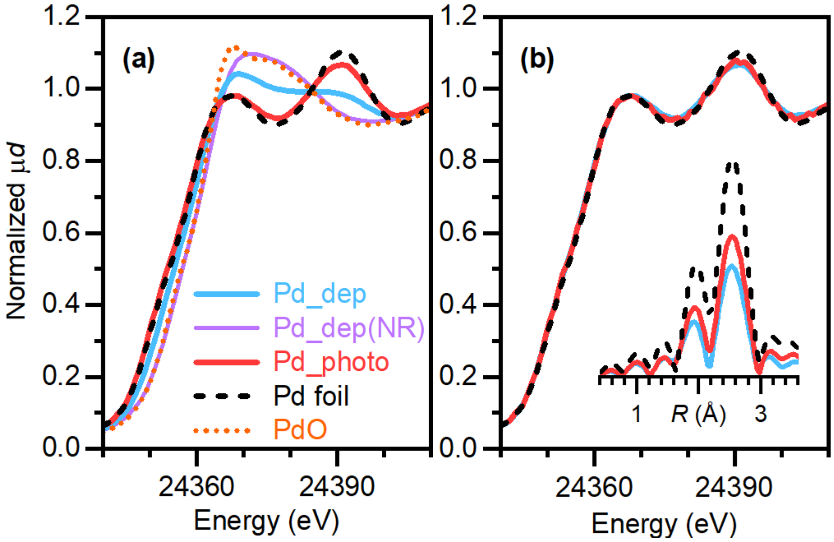

Figure 45. XANES spectra of Pd_photo (red) and Pd_dep (blue) Pd_dep(NR) (purple) as synthesized (a) and H_2-reduced at 150 °C (b), compared to PdO (dotted orange) and Pd foil (dashed black) references. The inset in part (b) shows the |FT|-EXAFS data.

Usually, an oxidized layer could be easily removed by a reductive treatment in H_2 at mild temperatures [176, 179, 180]. As was expected reductive treatment in H_2 at 150 °C completely reduced both samples to Pd^0 states, as shown in ***Figure 45b***. The average particle size of Pd_dep sample was of 2.6 nm determined based on the first-shell coordination numbers, and for Pd_photo an average particle size was ca. 1.3 nm (***Table 2***).

Table 2. EXAFS analysis of the reduced states of Pd_photo and Pd_dep in H_2 at 150 °C.

Sample	***R*, Å**	***N***	**σ^2, Å^2**	**Particle size, nm**
Pd_dep	2.73 ± 0.01	10.1 ± 0.5	0.010 ± 0.001	2.6
Pd_photo	2.73 ± 0.01	10.3 ± 0.4	0.008 ± 0.001	2.9

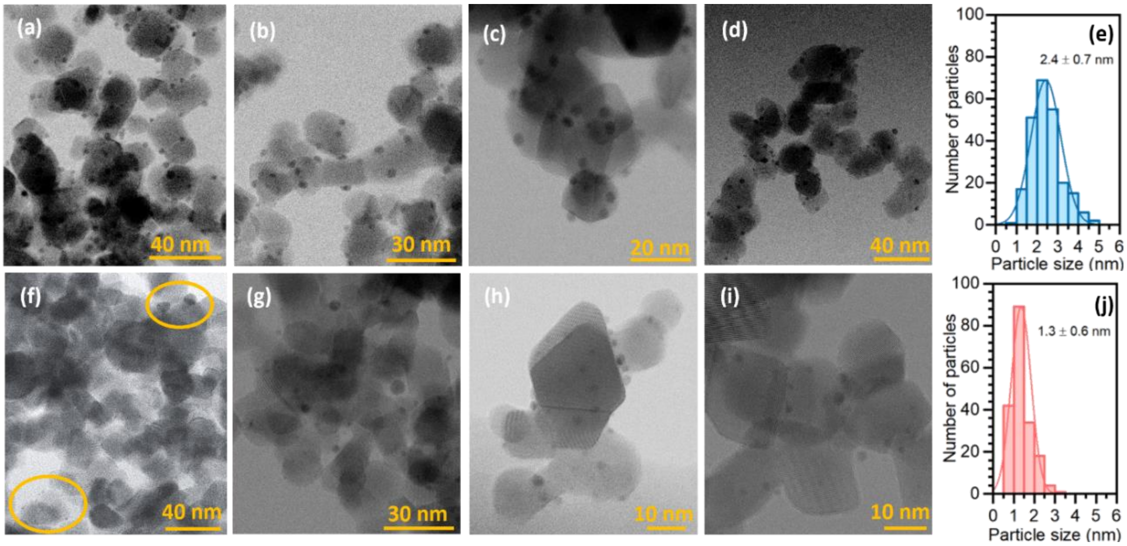

Figure 46. HR-STEM images and corresponding particle size distribution obtained for Pd_dep (a-e) and Pd_photo (f-l), showing the distribution of the Pd nanoparticles on the TiO_2 support. For Pd_photo, the particle size distribution is calculated on the majority of small particles, neglecting the few larger clusters.

The reduced samples were extensively characterized by HR-STEM (***Figure 46***). In Pd_dep, the Pd particles were spherically shaped, with an average dimension of 2.4 ± 0.7 nm (***Figure 46***), and regular crystalline planes and facets. Instead, the majority of Pd particles in Pd_photo were smaller, with narrow size distribution cantered at 1.3 ± 0.6 nm, and a few larger clusters (circles in ***Figure 46j***). These particles did not exhibit crystalline planes as regular as in Pd_dep, which correlates with previous studies on photodeposited Rh particles [167]. Remarkably, for Pd_dep the Pd particle size determined by HR-TEM in agreement with that inferred by a first shell analysis of the EXAFS spectra (inset in ***Figure 45b*** and ***Table 2***). In contrast, EXAFS largely overestimated the average particle size for Pd_photo, as the signal is influenced by a small number of larger particles.

6.2 Effect of SMSI on catalysts under oxidizing conditions

The reduced samples were heated in O_2 from 50 to 400 °C and left for 15 min at this temperature. The evolution of XANES spectra of Pd_dep and Pd_photo presented in ***Figure 47***, parts ***a*** and ***b***, respectively. In both cases, the white line at ca. 24370 eV intensified and the edge position shifted towards higher energies, which indicates the oxidation of Pd^0 to Pd^{2+}, but the effect was more pronounced for Pd_dep. To quantify the fraction of Pd^{2+} in the samples, LCF analysis was performed using the reference spectra of Pd foil and PdO (***Figure 47c***). When exposed to O_2 at 50 °C, both Pd_dep and Pd_photo samples were immediately reoxidized at the surface with Pd^{2+} fractions of 0.22 and 0.16, respectively. However, the two samples displayed a very different behavior upon increasing the temperature.

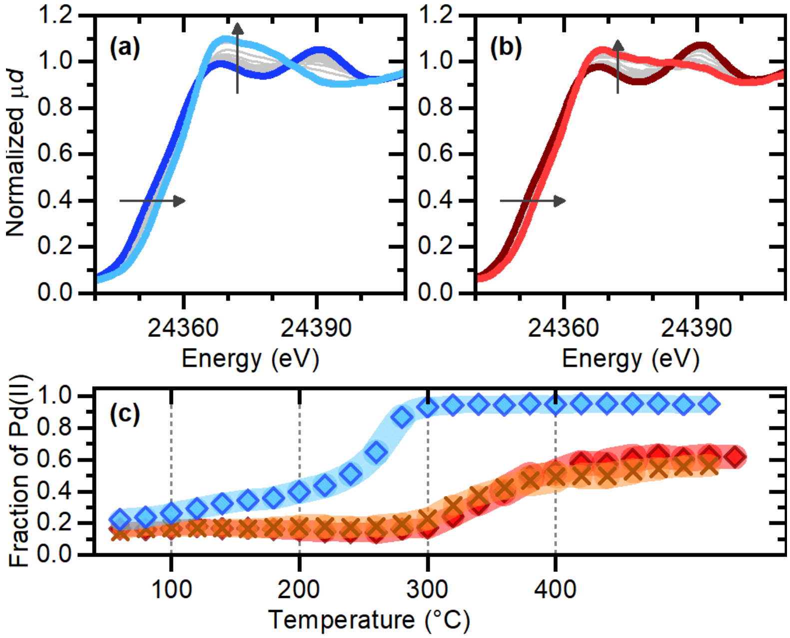

Figure 47. Evolution of XANES spectra for Pd_dep (a, from dark to light blue) and Pd_photo (b, from dark to light red) in O_2 from 50 to 400 °C, and fraction of Pd^{2+} obtained by LCF (c) for Pd_dep (blue) and Pd_photo (first oxidation – red circles, second oxidation – orange crosses). The line width is proportional to the error bars.

Pd_dep experienced further oxidation, which was fastened above 200 °C, up to be fully oxidized when the temperature reached 300 °C. This is in agreement with recent study on similarly sized particles in Pd/Al_2O_3, that showed surface and bulk oxidation of Pd NPs above 200 °C [177]. In contrast, Pd_photo remained in a prevalently metallic state up to 300 °C and did not reach complete oxidation even at 400 °C.

The stability of the Pd^0 state under oxidizing conditions is unusual for supported Pd particles, can be a result of SMSI in Pd_photo. Notably, after subsequent reduction at 400 °C followed by another oxidation run, the same oxidation profile was observed (orange crosses in ***Figure 47c***).

Moreover, from the analysis of the extended EXAFS spectra, the Pd–Pd interatomic distances contracted of upon oxidation and upon thermal treatment under inert atmosphere for Pd_dep in agreement with recent study [177, 181]. This, however, did not occur to Pd_photo sample (***Figure 48***), which further indicates an improved stability of Pd NPs in Pd_photo attributed to the SMSI effect.

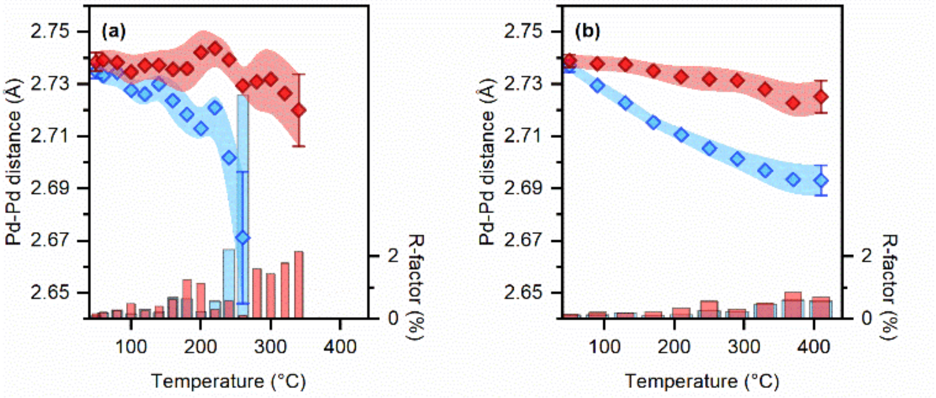

Figure 48. Evolution of the first-shell Pd–Pd distances in Pd_dep (blue) and Pd_photo (red) upon heating in (a) oxygen and (b) argon. Line width is proportional to the error bars.

To get atomic scale insights into the oxidation process and to demonstrate the occurrence of the SMSI effect in Pd_photo, both Pd/TiO_2 samples were studied by *in situ* HR-STEM. The TEM experiment conditions were adopted to reproduce the conditions of *in situ* XANES experiment. The lower partial pressures of the reactive gasses were used, as limited by the sample environment of the microscope (see Chapter 3 section 3.10).

For both samples, moving from H_2 to O_2 atmosphere led to the increase in the average NPs size (**Figure 49 *a*** and ***e***), due to particle agglomeration (***Figure 50***).

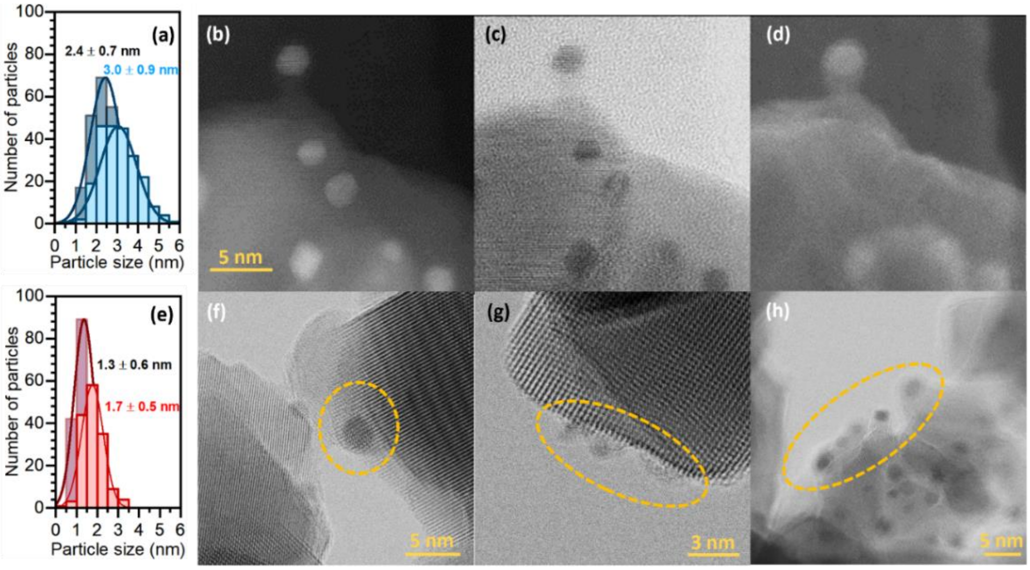

Figure 49. The size distributions obtained from *in situ* HR-STEM images for Pd_dep (a) and Pd_photo (e) under H_2 (dark color) and under O_2 (bright color). Electron micrographs of Pd_dep at 400 °C in O_2 obtained in the dark field (b), bright field (c) and secondary electron (d) modes demonstrating the presence of a PdO shell around metallic Pd core. Representative HR-STEM images of Pd NPs with volcano shape and encapsulated by TiO_2 in Pd_photo (f-h).

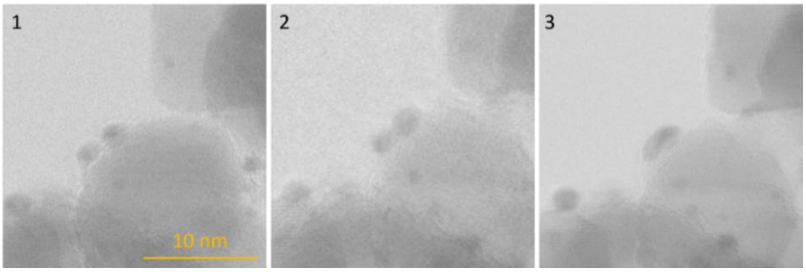

Figure 50. Bright field STEM images showing the agglomeration of 2 NPs while heating from R.T. to 400 °C in O_2.

Pd NPs in Pd_dep were generally more mobile under O_2 than in Pd_photo, often becoming visually separated from TiO_2 surface (***Figure 49b-d***). In Pd_dep two distinct phases were observed under O_2: a crystalline metal Pd core and an amorphous shell attributed to PdO (***Figure 49b-d***). Conversely, no PdO formation was apparent in Pd_photo during oxidation. The discrepancy with XANES data, which showed a minor oxidation, was likely due to lower O_2 partial pressure and electron beam's reductive effect. Instead, particles in Pd_photo became surrounded by a "volcano"-shaped layer attributed to TiO_2, based on HR-STEM (***Figure 49f-h***) and EDX (***Figure 51***) data. Furthermore, the Pearson correlation coefficient calculated for Pd L_3 and Ti L_3 EDX maps was −0.26 (negative correlation) for Pd_dep and +0.19 (positive correlation) for Pd_photo, in agreement with previous works reporting the encapsulation of NPs by TiO_2 [77-80, 166, 182].

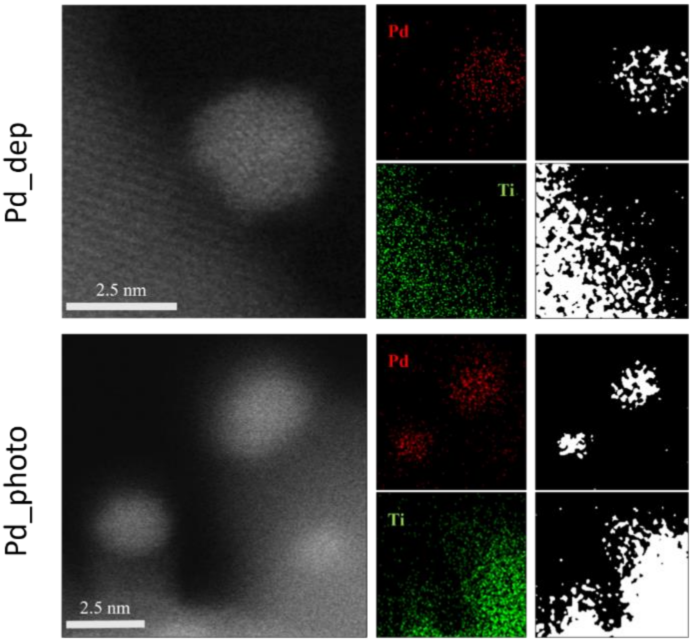

Figure 51. Dark field STEM images, corresponding EDX maps and threshold-filtered maps used for Pearson test for Pd_dep and Pd_photo.

Also, changes in the particle shape were observed: under H_2 atmosphere the particles were more flat, especially in Pd_photo, indicating a stronger interaction with the support, while in O_2 they became more spherical. This effect was quantitatively highlighted by the *Roundness* parameter (***Figure 52***), which is equal to unity for an ideal circle and approaches zero for an infinitely stretched ellipse.

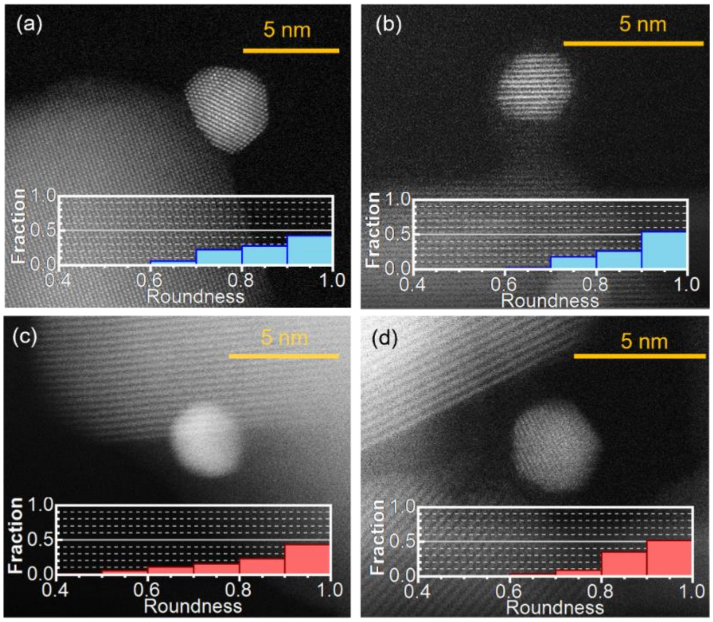

Figure 52. High-angle annular dark field (HAADF)– STEM images of Pd_photo after reduction (e) and oxidation (f) and Pd_dep after reduction (g) and oxidation (h). Insets in parts (e-h) demonstrate the distribution of the Roundness parameter.

The above observations for the Pd_photo sample can be summarized as follows:

1. Pd NPs are poorly crystalline
2. Pd NPs show larger deviation from the spherical shape
3. Sample has a lower tendency for oxidization
4. Absence of PdO surface layer
5. Encapsulation by TiO_2 support was observed

This suggests that the TiO_2 support alone is not sufficient to promote SMSI and that the deposition strategy for metal NPs also plays a crucial role.

6.3 Modifications in the TiO_2 due to the photodeposition of Pd

EPR and EELS spectroscopies (see Chapter 3 section 3.11 and 3.10) were employed to investigate the modifications that occurred in the TiO_2 support after depositing the Pd NPs and provided additional evidence for SMSI in Pd_photo. The Pd_dep sample after reduction showed a weak EPR response (***Figure 53a***, blue trace), characterized by a nearly isotropic signal centered at g = 2.003 and an anisotropic powder pattern in the range of $1.978 < g < 1.991$. The first signal had been convincingly attributed to trapped electrons at particle necks and interfaces [183]. The second signal served as a fingerprint for Ti^{3+} species in anatase [184]. The same reduction experiment on the Pd_photo sample resulted in a significant increase in the intensities of all EPR signals (***Figure 53b***, red trace).

The stronger Ti^{3+} signals allowed for the resolution of the resonance at $g \approx 1.95$, which was assigned to Ti^{3+} species in the rutile phase, as expected for TiO_2 P25 with mixed anatase/rutile phases [185]. After oxidation, the Pd_dep sample (***Figure 53a***, black trace) became EPR silent, while the Pd_photo sample revealed a small signal due to residual Ti^{3+} species in the oxidized sample (***Figure 53b***, black trace).

In summary, EPR spectroscopy showed a higher reducibility in the Pd_photo sample, with excess electrons being stabilized in the form of Ti^{3+} species. Additionally, the high intensity of the isotropic signal at g = 2.003 suggested a higher density of particle interfaces in the Pd_photo sample, indicating a stronger interaction between the Pd nanoparticles and TiO_2.

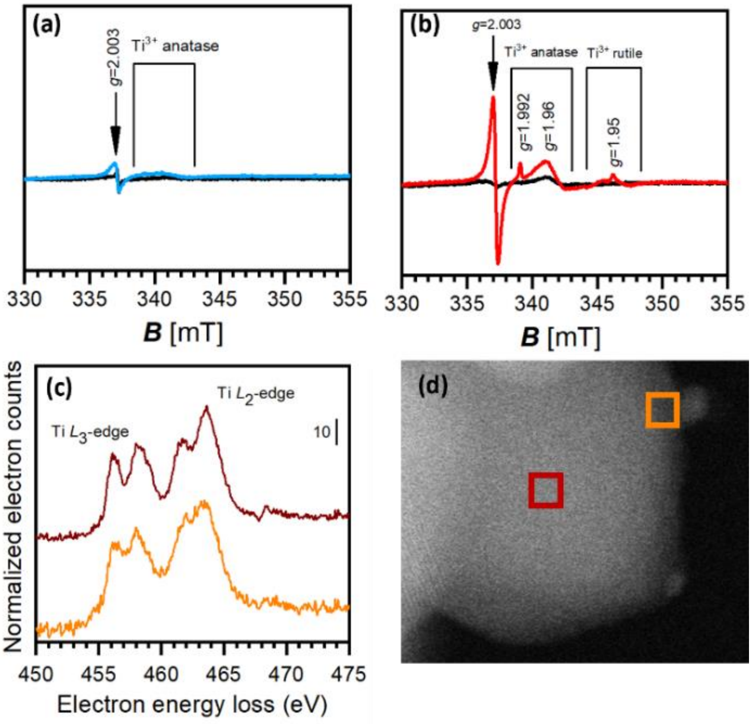

Figure 53. EPR spectra measured at liquid nitrogen temperature for (a) Pd_dep and (b) Pd_photo after oxidation (black) and after reduction (blue and red). (c) Ti *L*-edge normalized EELS spectra for Pd_photo taken from the points in the middle (red) of a TiO_2 particle and at the Pd/TiO_2 interface (orange), (d) Dark field STEM image with the corresponding highlighted areas where the EELS spectra were taken .

The formation of Ti^{3+} sites in H_2 at 150 °C is usually not observed in bare TiO_2, and is likely facilitated by the presence of Pd, which is responsible for hydrogen splitting and subsequent spillover. This was proven by EELS spectra, which measure the Ti(2*p*) → Ti(3*d*) electronic transitions, and allowed to locate the Ti^{3+} sites in Pd_photo at the interface of the Pd NPs (***Figure 53 c and d***). In the spectrum collected in the center of the TiO_2 particle (red color in ***Figure 53d***) both Ti L_2- and L_3-edges were split in two peaks at approximately 456-457 and 461-463 eV. This is typically observed for Ti^{4+} sites in octahedral coordination, as a consequence of the splitting of the unoccupied 3*d* states into lower t_{2g} and higher e_g levels. In the EELS spectrum collected near the Pd NP (orange color in ***Figure***

53d), instead, these 4 peaks were merged in the two, corresponding to the Ti L_2- and L_3-edges (about 457 and 463 eV), indicative of Ti^{3+}. Therefore, EELS spectra allowed not only to prove the presence Ti^{3+} species but also to locate them.

Finally, to have a proof of directly detecting the Pd–Ti interaction using Pd *K*-edge XAS spectroscopy a wavelet transformation approach was applied (***Figure 54***). This method differentiates contributions from different neighboring elements that are at the same distance from the absorbing atom. To this aim, a sample similar to Pd_photo but extracted from the synthesis batch after only 5 min of UV irradiation (instead of 20 min) was analyzed.

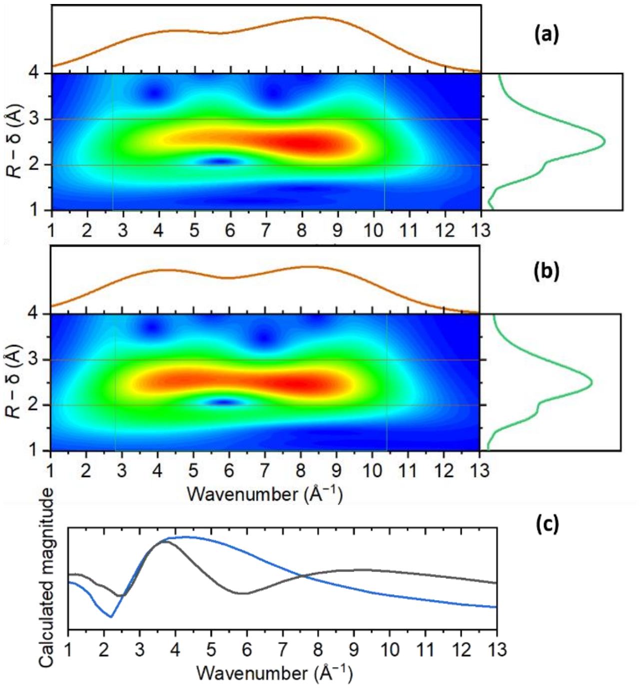

Figure 54. Wavelet-transform analysis of the EXAFS data of Pd_photo (a) and of a similar sample exposed to UV irradiation for only 5 min (b), complemented by the theoretical backscattering magnitudes for Pd–Pd (black) and Pd–Ti (blue) paths (c). The integration along radial distance and wavenumber, in the selected *k*- and *R*-regions, shown by vertical and horizontal bars, respectively in parts (a) and (b), are shown in the corresponding panels by green and, respectively, brown lines

This sample had a lower Pd–Pd coordination number of 8.9 (vs. 10.3 in Pd_photo), which enhanced the sensitivity to the surface atoms that could interact directly with Ti-sites. A comparison of the wavelet transformed EXAFS data between photodeposited samples irradiated for 20 min (***Figure 54a***) and 5 min (***Figure 54b***) evidenced the enhanced contribution around $k \sim 4$ Å^{-1} in the latter. This signal was attributed to Pd–Ti scattering, based on the theoretical backscattering magnitude of Pd-Pd and Pd-Ti paths (***Figure 54*c**). In addition, EXAFS fitting further supported this conclusion (***Figure 55*** and ***Table 3***). While the spectrum of Pd_photo (20 min) could be fitted with a single Pd–Pd path at 2.73 Å (***Figure 55a***), the use of a single path for the sample irradiated for 5 min resulted in a worse fit quality with a single path (***Figure 55b***), which could be improved by introduction of a Pd–Ti path at 2.66 Å (***Figure 55c***).

Table 3. EXAFS analysis of the reduced states of the samples, prepared by photodeposition method with irradiation time of 5 min, using single Pd–Pd path and combination of Pd–Pd and Pd–Ti paths.

Path	***R*, Å**	***N***	**σ^2, Å^2**	**R-factor, %**
Pd–Pd	2.72 ± 0.01	9.0 ± 0.6	0.010 ± 0.001	1.1
Pd–Pd	2.72 ± 0.01	8.8 ± 0.6	0.010 ± 0.001	0.4
Pd–Ti	2.66 ± 0.03	0.7 ± 0.9	0.006 ± 0.004	

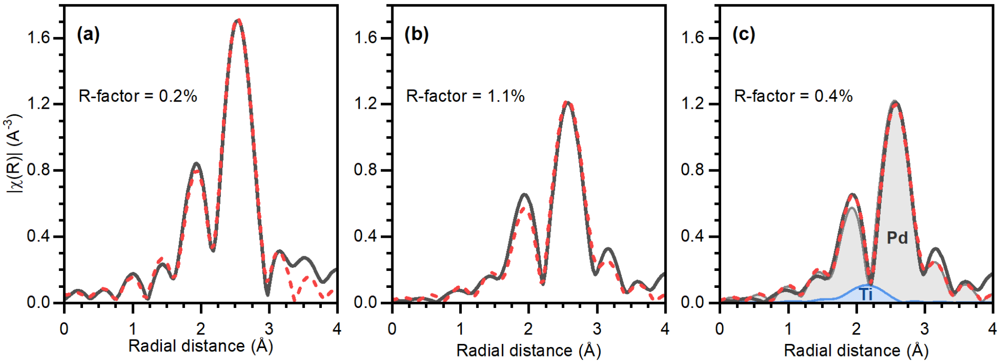

Figure 55. Experimental (solid black), fitted (dashed red) of the first-shell Pd–Pd distances and fitted of the first-shell Pd–Ti distances (solid blue) in Pd_ photo after 20 min (a) and 5 min of irradiation (b and c).

Going back to the differences in the synthesis procedure, the hypostasis is that the Ti^{3+} sites, were formed upon UV irradiation in presence of CH_3OH, and then the SMSI in Pd_photo facilitated the stabilization of the Ti^{3+} sites by Pd NPs. This is in agreement with previous reports, where preliminary created oxygen vacancies were shown to promote the photodeposition of metal particles on TiO_2 [186].

6.4 Structure of surface sites affected by SMSI in the Pd/TiO_2 samples

Complementary *in situ* FTIR spectra were measured using CO as a probe molecule to examine the surface properties and evolution of the surface sites. The two Pd/TiO_2 samples were investigated after oxidation at 400 °C (see Chapter 3 section 3.8), where the SMSI effect is maximized. CO was sent at room temperature (equilibrium pressure P_{CO} = 35 mbar) and IR spectra were collected repeatedly for 1 hour.

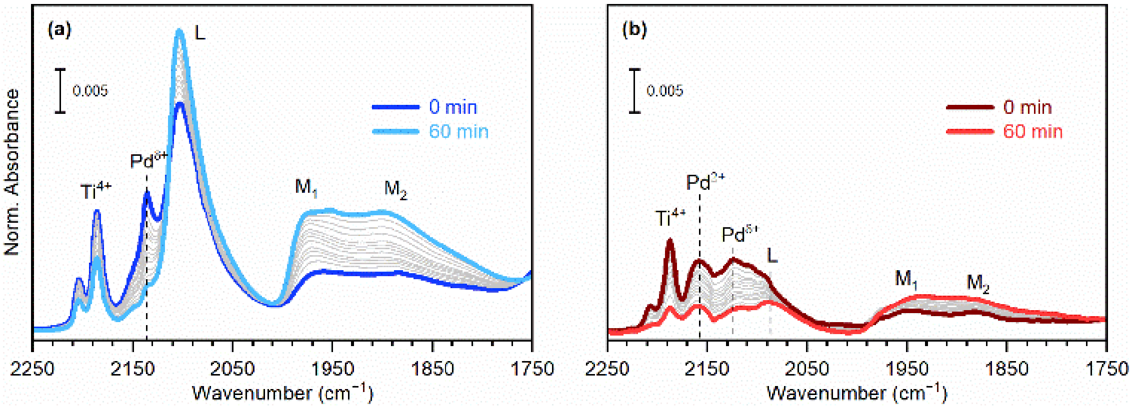

Figure 56. IR spectra of CO (P_{CO} = 35 mbar) adsorbed at room temperature on Pd_dep (a) and Pd_photo (b) previously oxidized at 400 °C (a). Evolution of the IR spectra of CO (P_{CO} = 35 mbar) adsorbed on Pd_dep (b) and Pd_photo (c) oxidized at 400 °C upon increasing contact times up to 60 min. The spectrum of the sample before dosing CO was subtracted from all the others. The spectra are normalized to the optical density of the pellet.

The initial IR spectrum intensity in the v(CO) region was significantly lower for Pd_photo (***Figure 56a)***, despite the smaller average Pd particle size compared to Pd_dep. This reduced intensity cannot be solely explained by the lower amount of palladium in Pd_photo, and was instead associated with the reduced CO chemisorption typical for SMSI [70]. Additionally ,in the presence of CO, the IR spectra gradually evolved, because CO progressively reduced PdO, forming CO_2 that was stabilized on the surface in the form of carbonates what also was observed in similar case [112].

The two initial spectra displayed the same absorption bands, but with different relative intensities. From the beginning, CO detected Ti^{4+} sites on the surface of TiO_2 (band at 2186 cm^{-1}) [187] positively charged Pd sites (Pd^{2+}, band at 2155 cm^{-1} and $Pd^{\delta+}$, band at 2135 cm^{-1}) [188, 189] and different types of Pd^0 sites. Bands associated to linearly bonded CO on (111) surface defects (L in ***Figure 56 b*** and ***c***), and to multi-folded coordinated carbonyls on both (100) and (111) surfaces of metallic Pd (M1 and M2 in ***Figure 56 b*** and ***c***) gradually appeared, at the expenses of the bands associated to positively charged Pd species. The relative intensity of these bands differed between the two experiments, in agreement with the different particle shape evidenced by HR-STEM. Notably, the band at 2155 cm^{-1} ascribed to Pd^{2+} was relatively intense in Pd_photo, indicating a significant amount of palladium single sites, which are almost absent in Pd_dep. These single sites likely formed during the initial stages of the photodeposition process and served as nucleation centers for the growth of Pd NPs.

6.5 Photocatalytic hydrogen production on Pd/TiO_2

The formation of H_2 during the PHER was analyzed using gas chromatography under conditions identical to those used for Pt/TiO_2 (***Figure 57***). Similar to the observations with platinum, the high H_2 to CO_2 production ratio indicates the catalyst's efficiency.

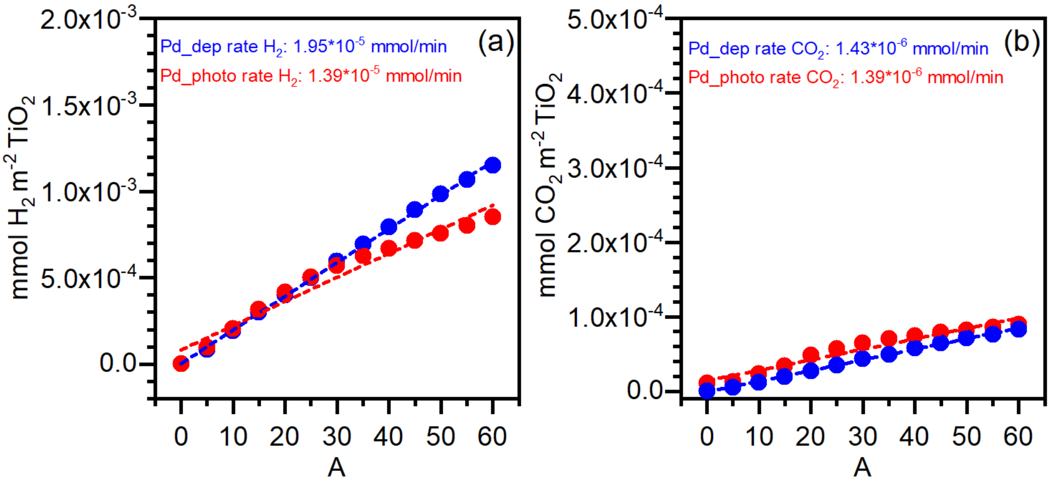

Figure 57. Photocatalytic H_2 (a) and CO_2 (b)production curves obtained for the Pd_dep (blue) and Pd_photo (red) normalized by specific surface area for different TiO_2 morphologies in the presence of methanol as hole scavenger.

It should be noted that the actual metal loading differed between the samples, a factor that must be considered when making quantitative comparisons of hydrogen production between them. Interestingly, the hydrogen production results showed comparable values for both samples, suggesting that the presence of SMSI effect does not negatively impact photocatalytic activity. This observation could also be related to the lower actual metal loading in the Pd_photo sample, as the efficiency of photocatalytic hydrogen production is highly dependent on this factor. When metal loading exceeds an optimal threshold, catalytic efficiency can decline. Because the excessive nanoparticle concentrations can act as recombination centers, reducing the catalytic activity.

It should also be noted that the photodeposited sample appeared to reach its maximum hydrogen production rate after about 30 minutes and then plateaued. This behavior is most likely related to the decomposition of methanol as shown ***on Figure 57b*** but also may indicate a saturation point or kinetic limitation in the reaction under these conditions.

6.6 Summary

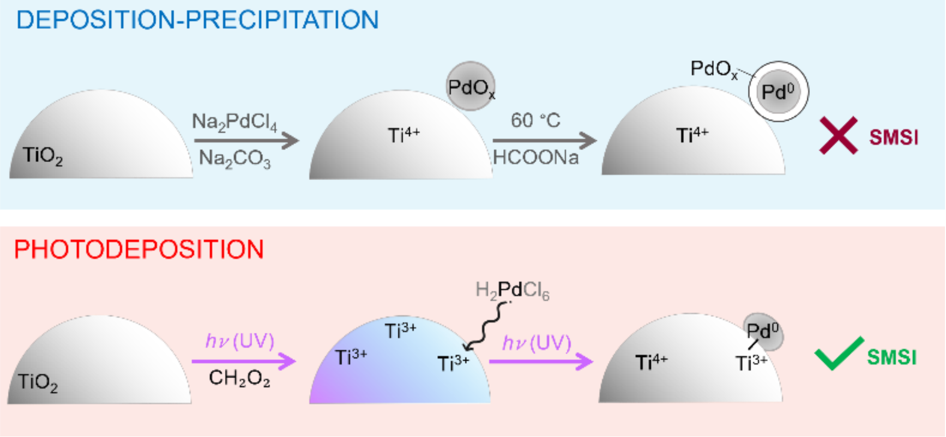

Using multiple analytical techniques, the SMSI was confirmed in Pd_photo sample. These findings demonstrate that the photodeposition method produced a pronounced SMSI effect, almost absent in samples obtained by deposition-precipitation. These findings suggest an alternative strategy for controlling metal-support interactions by adjusting the synthesis procedure of Pd nanoparticles on TiO_2. This approach provides a means to modulate the redox properties of Pd particles, thereby allowing for precise tuning of the catalytic properties of Pd/ TiO_2 based catalysts.

7 Conclusions

As the result of this work, notable advancements in the understanding of the relationships between synthesis conditions, reaction conditions, structure and photocatalytic activity have been achieved through the multi-technique study of metal nanoparticles supported on TiO_2 nanostructures, which have shown substantial promise for green hydrogen production.

This thesis provides an in-depth understanding of the mechanisms and processes involved in photocatalytic hydrogen production using metal-TiO_2 systems, specifically those containing Pt and Pd nanoparticles. The primary objective of this work was to investigate the interactions between metal nanoparticles and TiO_2 supports, with particular emphasis on how varying TiO_2 morphologies and synthesis methods affect these interactions.

To address these research questions, the catalysts were examined under realistic operating conditions, including specific temperature, pressure, and reactive environments, as well as UV irradiation. This study utilized advanced *in situ* and *operando* characterization techniques such as X-ray absorption spectroscopy (XAS), Fourier transform infrared spectroscopy (FTIR), and scanning transmission electron microscopy (STEM) to gain an understanding of the dynamic processes governing the photocatalytic hydrogen production and deepening the advancing knowledge of the photocatalyst behavior under operating conditions.

The application of *in situ* and *operando* methods in photocatalysis is less common compared to the field of heterogenous thermocatalysis due to the technical challenges associated with creating sample environments suitable for data collection during photocatalytic reactions. To overcome these limitations, a custom-designed photocatalytic cell was developed in the frame of my project, allowing for *in situ* and *operando* experiments that integrate multiple analytical techniques within a single setup.

The objective of this research was not to develop an improved photocatalyst but to achieve a deeper understanding of the catalyst systems, thereby paving the way for the rational design of photocatalysts in the future. Consequently, Pt and Pd supported on TiO_2 were selected due to their established efficiency in hydrogen production and their utility as initial model systems, given their extensive documentation in the literature.

The study demonstrated the critical roles of TiO_2 nanoparticle morphology, as well as the shape and size of the metal nanoparticles, in determining catalytic activity. Key factors affecting catalysts' photoactivity were identified, and potential strategies for optimizing the system to enhance hydrogen production efficiency were discussed.

The initial and essential objective of this research was to elucidate the mechanisms underlying the photodeposition of metallic co-catalysts on TiO_2. Photodeposition of Pt on TiO_2 was initiated by the reduction of Pt precursors (Pt^{4+} to Pt^0) via photogenerated electrons in the presence of a hole scavenger, such as methanol or formic acid. This process was highly influenced by the morphology of the TiO_2 support, with the (101) surfaces enabling superior electron transfer and facilitating the efficient reduction of Pt ions. Consequently, Pt nanoparticles were preferably deposited on the (101) facets of TiO_2 due to the preferential migration of photogenerated electrons to these surfaces. XAS analysis further indicated that Pt nanoparticle formation occurred directly, without the formation of intermediate species.

In contrast, while Pd photodeposition followed a similar reduction pathway (from Pd^{2+} to Pd^0), it involved the formation of intermediate Pd^0 species, attributed to either single sites or ultra-small clusters. Additionally, palladium hydride phase was detected, which was not observed in the case of platinum. The resulting photodeposited nanoparticles of both Pt and Pd were in a metallic state. However, upon exposure to the atmosphere, Pd nanoparticles synthesized through alternative methods (deposition-precipitation), exhibiting behavior more typical of standard Pd NPs on oxide supports.

The findings reveal distinct formation mechanisms for Pt and Pd nanoparticles, significantly impacting their size and morphology. TEM analysis showed morphological differences between platinum and palladium nanoparticles synthesized via photodeposition. Pt NPs generally exhibited a flatter shape and a less homogeneous distribution on the TiO_2 support compared to Pd NPs. Additionally, Pt NPs tended to form coral-shaped agglomerates rather than being uniformly distributed, although previous studies with lower metal loading demonstrated that it is possible to synthesize individual, round Pt nanoparticles. Palladium nanoparticles, regardless of synthesis method, photodeposition or deposition-precipitation, were more uniformly distributed on the TiO_2 surface and consistently formed separate, round particles. This indicates that the morphology of the nanoparticles is largely determined by the metal itself rather than by the synthesis technique.

In situ synthesis of metal/TiO_2 photocatalysts, utilizing TiO_2 immobilized on the window of the photocatalytic cell, resulted in a highly uniform distribution of Pd nanoparticles with a narrow size distribution, around 1 nm. Conversely, laboratory batch synthesis produced Pd particles that were larger and less homogeneously distributed on the TiO_2 surface, with some nanoparticles exceeding 30 nm. This result highlighted the role of reactor design in addition to the synthesis protocol. In contrast, Pt NPs had larger sizes of about 3 nm in both the *in situ* synthesis in photocatalytic cell and in the lab reactor. This comparison highlights the influence of synthesis conditions on nanoparticle size, morphology, and distribution, as well as the differential behavior of Pt and Pd on TiO_2, which may affect their photocatalytic performance.

The Strong Metal-Support Interaction (SMSI) was observed in both Pt and Pd systems synthesized via photodeposition, underscoring that this synthesis method effectively promotes SMSI. The SMSI effect facilitates electron donation from the TiO_2 support to the metal nanoparticles, weakening oxygen bonding on the metal surface and significantly impacting the redox properties of the material. Importantly, SMSI formation depends not only on the synthesis method but also on specific titanium dioxide morphologies. My studies indicated that the (101) surface in TiO_2 morphologies serves as a site for electron accumulation under UV irradiation, which further initiates the formation of metal nanoparticles with enhanced metal-substrate interaction. Given that P25 predominantly exposes (101) surfaces and possesses a mixed anatase-rutile phase structure, it exhibits improved charge carrier separation and migration. The interaction of Pt and Pd co-catalysts with P25 TiO_2 optimizes the separation of photoinduced charge carriers, making metal/P25 samples highly effective for hydrogen production, despite significant differences in the morphology of Pt and Pd nanoparticles.

Interestingly, while SMSI enhances charge carrier separation and stabilizes metal nanoparticles on the TiO_2 surface and expected to boost catalytic efficiency and durability. However, the presence of SMSI itself had only a modest impact on the overall hydrogen production. This suggests that while SMSI contributes to the photocatalyst's stability and charge separation, it may not be the sole factor governing photocatalytic hydrogen production efficiency.

This study provides valuable insights into the mechanisms of metal photodeposition and the role of SMSI in improving the catalytic stability and activity of these systems. The findings demonstrate that the photodeposition of Pt and Pd on TiO_2 can be optimized by controlling the synthesis method, enhancing metal-support interactions, and fine-tuning nanoparticle size. It is important to note, that in contrast to supported metal nanoparticles synthesized by conventional deposition-precipitation methods, SMSI in photodeposited samples prevents both Pt- and Pd- particles from oxidation even at high temperatures under molecular oxygen. In addition, the stabilized Ti^{3+} species were identified in these samples using a combination of EPR and EELS spectroscopies.

In conclusion, this study demonstrates that rational design can pave the way for the development of advanced photocatalytic materials. The use of *in situ* and *operando* methods is essential to understand the dynamic nature of photocatalytic systems and provide mechanistic insights needed to optimize performance.

8 Side activities

Apart from the main research focused on the *in situ* and *operando* characterization of the Pt- and Pd-based photocatalysts on TiO_2, presented in the Chapters 4 – 6, I was also involved in several other research projects led by my colleagues in the University of Turin, Paul Scherrer Institute, ALBA Synchrotron, University of Palermo, KU Leuven and Southern Federal University. Although these projects differ slightly in materials and applications, they are linked by the use of *in situ* and *operando* spectroscopy for characterization of materials, which is quite close to the main topic of my research. This Chapter aims to present a brief overview of the most important of these projects.

All these parallel activities described in this chapter, although not included in my main PhD thesis, have played a significant role in my research. Through conducting this supplementary research, I gained valuable insights that enhanced my primary work, while also enhancing my skills in *operando* and *in situ* characterization techniques for materials.

8.1 Photoreforming of glycerol for H_2 production on Pt/TiO_2

The first and fairly close study was conducted on platinum deposited on different TiO_2 polymorphs. Photocatalysts were used for H_2 production from glycerol photoreforming [190]. This project is led by Prof. Marianna Bellardita University of Palermo and my supervisor Prof. Lorenzo Mino.

Since the direct splitting of water is a very difficult process to carry out both from a thermodynamic and kinetic point of view the photo-reforming reaction, thus H_2 production from glycerol photoreforming can be used as promising reaction for this aim. This reaction was used as model one to compare activity of anatase, rutile and brookite TiO_2 polymorphs, functionalized with Pt as co-catalyst. To correlate the photocatalytic activity with the catalyst surface properties FT-IR spectroscopy was employed. The results show that the H_2 production from glycerol photoreforming and the intermediate products distribution are strongly dependent on the nature of the TiO_2 support. Brookite was the most active sample, and its amount decreases in the order Pt-brookite > Pt-P25 ≈ Pt-anatase > Pt-rutile, and this trend follows the hydrophilicity order of the different polymorphs.

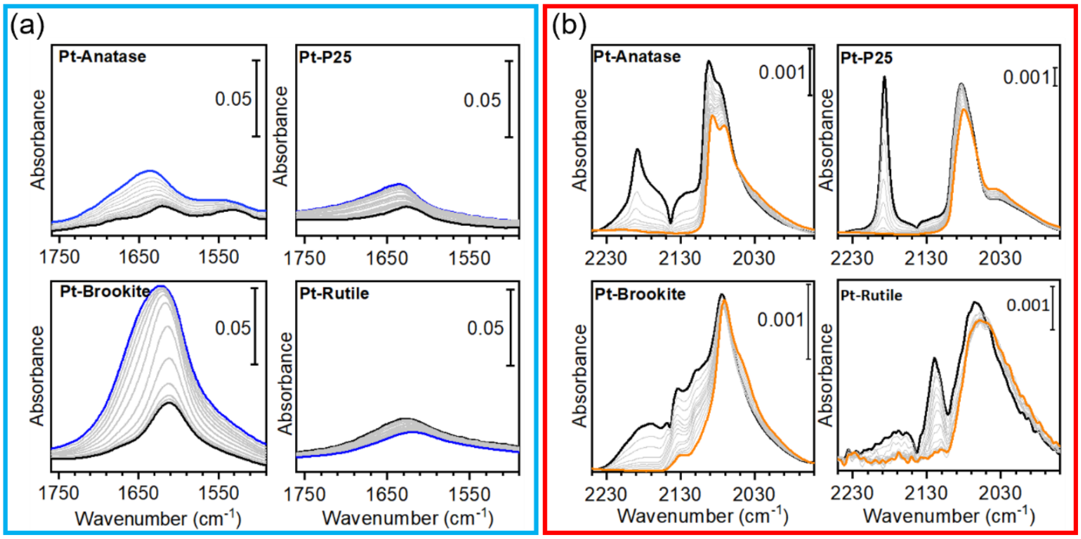

Figure 58. FT-IR spectra of the different materials (a) in contact with H_2O at 15 mbar (blue curve) and progressive decreasing of the water coverage till outgassing for 15 minutes at beam temperature (black curve), (b) after activation at 673 K and reduction at 423 K, in contact with CO at 40 mbar (black curve) and progressive decreasing of the CO coverage till outgassing for 15 minutes at beam temperature (orange curve).

For this project, I did FT-IR spectroscopy measurements (***Figure 58***) to assess the water adsorption properties of catalyst and to probe, by CO adsorption, the Pt active sites. This project helped to shed light on the metal-support interactions in the case of platinum and was used to interpretate the data in Chapter 4.

8.2 Spectroscopic studies of Pd NPs on metal-oxide supports

The second part two of side activities are devoted to the characterization of Pd NPs on oxide support using advanced spectroscopic analysis.

The work under the guidance of Oleg Usoltsev and Aram Bugaev [112] demonstrates a method for extracting quantitative structural information by application of machine learning (ML) algorithms for quantitative characterization of nanoparticles from infrared spectra. ML algorithms were applied to study palladium hydride formation, which is an important catalyst in numerous hydrogenation reactions. This work presents a novel phenomenon of the metal–metal interatomic distances effect on the vibrational spectra of probe molecules and turn it to a new method for quantitative characterization of IR data. The work also showed that CO molecules which was used as probes molecule in FTIR, can originate as reaction intermediates, have an irreversible effect on the PdH_x phase, highlighting the necessity of use *in situ* characterization techniques.

The next work [191] with this group investigates the oxidation and reduction processes Pd nanoparticles supported on a substrate, sing *in situ* time-resolved XAS and theoretical simulations. During oxidation, the Pd nanoparticles develop a core@shell structure, where a palladium oxide (PdO) shell forms around a metallic Pd core. This oxidation begins at low-coordinated sites (edges) of the nanoparticles and increases as the temperature rises above 200 °C. The oxidation weakens the interaction between the metal and the support material, causing the particles to become more spherical. Importantly, the PdO shell does not affect the average Pd–Pd coordination within the metallic core, but the metallic core shrinks slightly as the PdO phase grows. This research provides valuable insights into the dynamic structural changes of Pd during catalytic reactions, such as methane combustion and alcohol oxidation.

During these projects, I participated in beamtime sessions at the Paul Scherrer Institute (Switzerland) and ESRF (Grenoble, France), which provided valuable hands-on experience and helped to gain insight into the behavior of Pd NPs on an oxide support, which was used to interpret the data in Chapter 5 and 6.

8.3 Investigation of MOF-based catalysts

A slightly different research direction, also focused on Pd nanoparticles, was led by Alina Skorynina, Aram Bugaev, and colleagues from the University of Oslo and the Turin. This study [192] explores the structural evolution of Pd nanoparticles embedded in Zr-based metal-organic frameworks (MOFs), specifically UiO-67, during CO_2 hydrogenation. The Pd@UiO-67 catalyst was examined under varying temperatures and pressures using advanced *operando* techniques, including simultaneous X-ray diffraction and XAS spectroscopy.

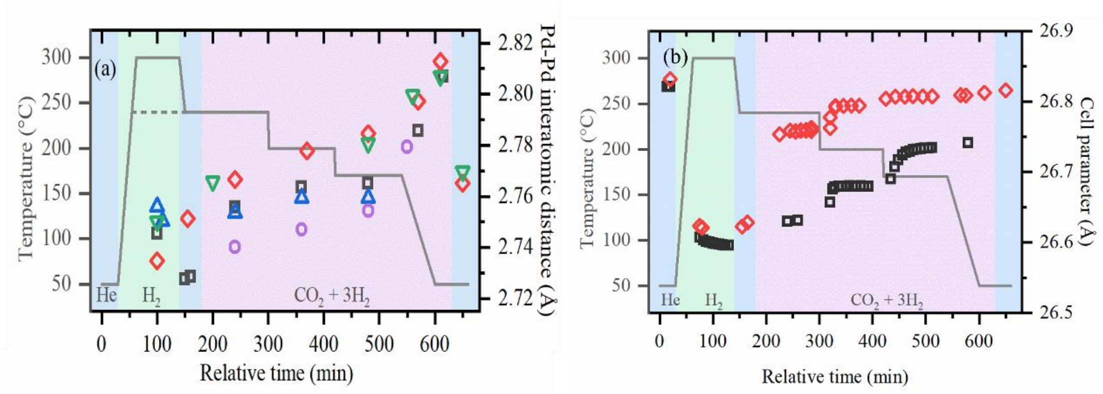

Figure 59. Pd–Pd interatomic distances (a) determined by first-shell fitting of EXAFS data collected for the samples activated at 300 °C in H_2 and used for CO_2 hydrogenation under 1 bar and 8 bar (black squares and red diamonds, respectively), activated at 240 °C in H_2 and used for CO_2 hydrogenation under 1 bar and 8 bar (blue up and green down triangles, respectively) and activated directly in reaction mixture at 1 bar at 240 °C (purple circles). Colored areas of the background correspond to different gas environment: blue – helium flow, green – hydrogen flow, pink – reaction mixture. (b) Cell parameter of UiO-67 samples during activation in H_2 and reaction under 1 bar (black squares) and 8 bar (red diamonds) obtained by the refinement of XRPD data.

These methods allowed to monitor changes in both the Pd nanoparticles and the MOF structure during the reaction. The analysis revealed that formed of mixed palladium carbide and hydride phases during the adsorption of CO on the surface of the Pd nanoparticles played a key role in the hydrogenation process. Notably, this work achieved the first observation of the Pd/Zr interface in the Zr-based metal-organic frameworks and its association with methanol formation, highlighting the importance of the metal-support interaction in enhancing catalytic activity for CO_2 hydrogenation.

During this project, I was part of the team which conducted experimental procedures and performing data analysis in beamtimes at ESRF (Grenoble, France) and gained useful experience.

8.4 XANES and DFT simulations for Pd^{II}/Ag^{I}-based homogenous catalyst for electrophilic amination of simple arenes

Another study focused on palladium was dedicated to the optimization of the catalytic system of electrophilic amidation (EA) of simple arenes [193]. Where EA involving transition metal-catalyzed C-H activation of the arene is a promising method for directly constructing C-N aryl bonds. This method is promising because it allows for the direct formation of these bonds. To make the reaction easygoing, a special leaving group is attached to the nitrogen, helping to overcome energy barriers and make the reaction more efficient. However, there are some challenges, any studies only work well with arenes that have large, specific groups attached or require nitrogen partners with complex leaving groups. Additionally, many of these reactions need extra chemicals (like ligands or bases) in large amounts. In this work the system based on Pd^{II}/Ag^{I} ligand-free method was used for electrophilic amidation (EA) of simple arenes with O-acetyl acetohydroxamic acid (AcNHOAc). In contrast with previously reported systems, the reaction neither requires a ligand, nor super stoichiometric amounts of additives. Furthermore, the proposed mechanism only involving Pd^{II} species (according to kinetic, *in situ* spectroscopic data corelated with DFT), in which coordination of AcNHOAc occurs before C-H activation. The new mechanism offers a more detailed and refined understanding of the steps involved, addressing potential gaps or inaccuracies in Emmert's original proposal [194].

In this and the next paper in which I was involved, in addition to characterizing the catalysts using *in situ* spectroscopy (***Figure 60b***), I also contributed to the density functional theory (DFT) calculations (***Figure 60a***), which provided valuable support for the experimental data.

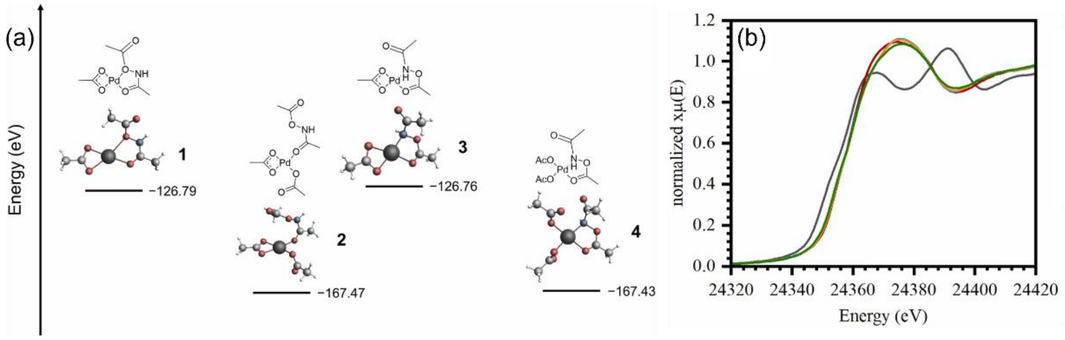

Figure 60. (a) Results of DFT relaxation of various coordination modes of Pd with acetate and AcNHOAc ligands with corresponding bond energies in eV (with respect to the elemental states), (b) XANES spectra for the diferemt catalyst intermidiets during the reaction ($Pd(OAc)_2$ (red), $Pd(OAc)_2$ + AcNHOAc at 80 °C (blue) and at 105 °C (orange), and $Pd(OAc)_2$ + AcNHOAc + AgOAc at 105 °C (green)) with reference Pd^0 foil (black).

8.5 High-pressure sample environment, machine learning for XANES analysis and DFT calculation of Ru-based hydrodeoxygenation catalyst evolution

The second parallel research activity was done for Ru-catalyzed selective hydrodeoxygenation of glycerol. This work establishes structure-property relationship s in Ru-based catalytic systems by combining extensive catalytic testing, *in situ* XAS under high pressures and temperatures, and *ex situ* XAS structural characterization supported by DFT calculations (***Figure 61***) [194].

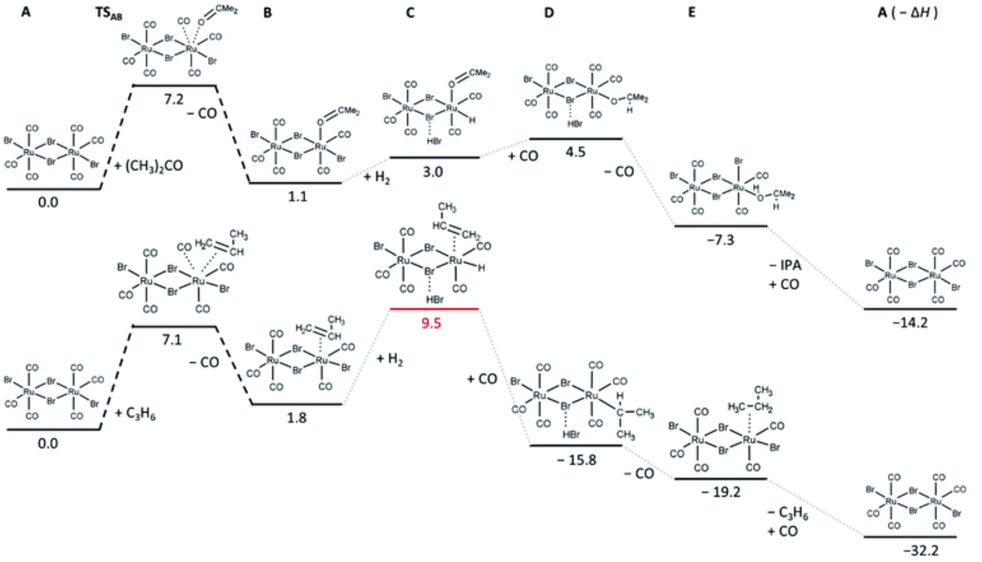

Figure 61. Relative energies in kcal mol−1 of the most stable intermediates and first transition state determined for acetone (top) and propene (bottom) hydrogenation reactions. Screening of possible intermediate states in the hydrogenation of acetone and propene was performed at DFT level of theory, based on the minimal energy of their relaxed structures.

We develop a special cell for this work, which allows experiments to be performed in high-pressure and high-temperature conditions to study the catalytic processes under relevant industrial conditions [195]. The homogeneous ruthenium catalysts have a promising application in the reaction of hydrodeoxygenation of sugar alcohols to alkenes, which are essentially the building blocks for the modern chemical industry. But unfortunately, this reaction can further lead to the hydrogenation of alkenes into less valuable alkanes. Addition of ionic liquid Bu_4PBr (IL) and CO gas to the system can help to avoid this transition. This work focuses on elucidating the different catalytic steps in the Ru-catalyzed hydrodeoxygenation of glycerol to propene by monitoring the evolution of Ru-species. It was proved that catalyst dissolution ($RuBr_3$) in the IL leads to the formation of new active complexes $[RuBr_2(CO)_3]_2$ in the presence of CO gas, which only under these conditions can selectively hydrogenate C=O bonds over C=C bonds.

9 Acknowledgement

Big thanks to my amazing supervisor, Lorenzo Mino! Your endless patience deserves a medal — especially after all the times I bombarded you with a million questions and occasionally some “brilliant” ideas that needed shutting down right before the deadline Thank you for your guidance and kindness, for truly listening to my thoughts. You've managed to make this journey not only possible but genuinely enjoyable, both professionally and personally. I honestly couldn’t have done it without you!

Huge thanks to my co-supervisor, Aram Bugayev. Thank you for believing in me. You were always there with your wisdom and a perfectly timed motivational kick to keep me moving forward (and let’s be real, I definitely needed it). Thanks for all those “let’s try this again” moments and for making the lab a place where hard work somehow felt like a good time. Your support has meant the world, especially when you encouraged me to step out and connect with the broader scientific community, opening doors I never imagined possible. And let’s not forget the endless supply of wild ideas and fun projects you pulled me into. Your enthusiasm made everything feel possible, and you, fooling around at the synchrotron, kept the late nights of work entertaining. Thanks for showing me that even the toughest work can come with a good laugh!

Thanks to Elena Groppo who has been a key figure throughout my studies, lending her expertise and mentorship at every turn. Your willingness to step in, offer advice, and share your knowledge was really valuable.

Thanks to Francesco Pellegrino, my chemistry hero! Thanks for being such an awesome and patient mentor and staying with me even when my synthesis skills were...well, let’s say, “a work in progress.”

I owe a huge thank to Guillermo, my Spanish buddy, who didn’t just welcome me to the UniTo PhD circus but made it feel like home. From day one, you were there, helping me find my way, introducing me to new friends, and making sure I was just as comfortable outside the lab as inside. You've taught me that this whole PhD thing isn't just about getting results — it's about finding real friends.

To everyone from UniTo especially from Via Guria - professors, colleagues, and students. Thank you for filling these 3 years with laughter, friendship, and endless support. You've made this time unforgettable, and I feel lucky to be part of such an amazing community.

To my awesome colleagues from Southern Federal University — Alina, Oleg, and Anna. Alina and Oleg, thank you for letting me ask you every question that I didn't dare to ask my supervisor, because you never judged. And Anna, thank you for always helping with my strangest requests, no questions asked. You all went beyond just "colleagues"— you're the friends who were there when I needed it most. Thanks for the amazing support I could count on!

To my family — thank you for your endless love and support. To my parents, Inna and Gena, Mama and Papa: you have supported me through all these miles, always encouraging me from afar. Knowing that you are by my side has given me the courage to keep going. I owe so much of who I am to. To my husband, Zhenia: thank you for being not just my partner but my best friend. You've been my rock and my laughter through these PhD years. You didn't just change your life to be here with me, you built a whole new one around us, and I couldn't be more grateful. And to my twin sister, Sonechka, my lifelong buddy: thank you for holding my hand through every step, for always protecting me, and for being there to share every challenge and every victory. Thank you for always believing in me, especially on days when I didn't believe in myself.

This journey has been about more than just research. It's been about resilience, growth, and the people who lift me up. I couldn't have done this without each and every one of you. Thank you for being my family, my friends, and my forever cheerleaders. I'm so, so lucky to have you all in my life!

10 Bibliography

[1] E. Parliament, Regulation (EU) 2018/1999 and Directive 98/70/EC as regards the promotion of energy from renewable sources, and repealing Council Directive (EU) 2015/652, European Parliament - Legislative observatory, Procedure number: 2021/0218/COD, The Member States, 2023.

[2] IEA, Global hydrogen review, Licence: CC BY 4.0, Paris, 2023.

[3] J.D. Holladay, J. Hu, D.L. King, Y. Wang, An overview of hydrogen production technologies, Catalysis Today, 139 (2009) 244-260.

[4] L.M. Ringsgwandl, J. Schaffert, N. Brücken, R. Albus, K. Görner, Current legislative framework for green hydrogen production by electrolysis plants in Germany, Energies, 15 (2022) 1786.

[5] B.S. Zainal, P.J. Ker, H. Mohamed, H.C. Ong, I.M.R. Fattah, S.M.A. Rahman, L.D. Nghiem, T.M.I. Mahlia, Recent advancement and assessment of green hydrogen production technologies, Renewable and Sustainable Energy Reviews, 189 (2024) 113941.

[6] C.-H. Liao, C.-W. Huang, J.C.S. Wu, Hydrogen production from semiconductor-based photocatalysis via water splitting, Catalysts, 2 (2012) 490-516.

[7] J.A. Turner, Sustainable hydrogen production, Science, 305 (2004) 972-974.

[8] J.H. Kim, D. Hansora, P. Sharma, J.-W. Jang, J.S. Lee, Toward practical solar hydrogen production – an artificial photosynthetic leaf-to-farm challenge, Chemical Society Reviews, 48 (2019) 1908-1971.

[9] H. Nishiyama, T. Yamada, M. Nakabayashi, Y. Maehara, M. Yamaguchi, Y. Kuromiya, Y. Nagatsuma, H. Tokudome, S. Akiyama, T. Watanabe, R. Narushima, S. Okunaka, N. Shibata, T. Takata, T. Hisatomi, K. Domen, Photocatalytic solar hydrogen production from water on a 100-m^2 scale, Nature, 598 (2021) 304-307.

[10] H. Wang, L. Zhang, Z. Chen, J. Hu, S. Li, Z. Wang, J. Liu, X. Wang, Semiconductor heterojunction photocatalysts: design, construction, and photocatalytic performances, Chemical Society Reviews, 43 (2014) 5234-5244.

[11] X. An, C. Hu, H. Liu, J. Qu, Hierarchical nanotubular anatase/rutile/TiO_2 (B) heterophase junction with oxygen vacancies for enhanced photocatalytic H_2 production, Langmuir, 34 (2018) 1883-1889.

[12] A.S. Hainer, J.S. Hodgins, V. Sandre, M. Vallieres, A.E. Lanterna, J.C. Scaiano, Photocatalytic hydrogen generation using metal-decorated TiO_2: Sacrificial donors vs true water splitting, ACS Energy Letters, 3 (2018) 542-545.

[13] Q. Xu, B. Cheng, J. Yu, G. Liu, Making co-condensed amorphous carbon/g-C3N_4 composites with improved visible-light photocatalytic H_2-production performance using Pt as cocatalyst, Carbon, 118 (2017) 241-249.

[14] W.-K. Jo, N.C.S. Selvam, Z-scheme CdS/g-C_3N_4 composites with RGO as an electron mediator for efficient photocatalytic H_2 production and pollutant degradation, Chemical Engineering Journal, 317 (2017) 913-924.

[15] X. Liu, P. Wang, H. Zhai, Q. Zhang, B. Huang, Z. Wang, Y. Liu, Y. Dai, X. Qin, X. Zhang, Synthesis of synergetic phosphorus and cyano groups (CN) modified g-C_3N_4 for enhanced

photocatalytic H_2 production and CO_2 reduction under visible light irradiation, Applied Catalysis B: Environmental, 232 (2018) 521-530.

[16] M. Zhang, H. Lin, J. Cao, X. Guo, S. Chen, Construction of novel S/CdS type II heterojunction for photocatalytic H_2 production under visible light: The intrinsic positive role of elementary α-S, Chemical Engineering Journal, 321 (2017) 484-494.

[17] N. Qin, J. Xiong, R. Liang, Y. Liu, S. Zhang, Y. Li, Z. Li, L. Wu, Highly efficient photocatalytic H_2 evolution over MoS_2/CdS-TiO_2 nanofibers prepared by an electrospinning mediated photodeposition method, Applied Catalysis B: Environmental, 202 (2017) 374-380.

[18] X. Xing, M. Zhang, L. Hou, L. Xiao, Q. Li, J. Yang, Z-scheme BCN-TiO_2 nanocomposites with oxygen vacancy for high efficiency visible light driven hydrogen production, International Journal of Hydrogen Energy, 42 (2017) 28434-28444.

[19] A. Fujishima, K. Honda, Electrochemical photolysis of water at a semiconductor electrode, Nature, 238 (1972) 37-38.

[20] B. Bakbolat, C. Daulbayev, F. Sultanov, R. Beissenov, A. Umirzakov, A. Mereke, A. Bekbaev, I. Chuprakov, Recent developments of TiO_2-based photocatalysis in the hydrogen evolution and photodegradation: A review, Nanomaterials, 10 (2020) 1790.

[21] J.L. White, M.F. Baruch, J.E. Pander, III, Y. Hu, I.C. Fortmeyer, J.E. Park, T. Zhang, K. Liao, J. Gu, Y. Yan, T.W. Shaw, E. Abelev, A.B. Bocarsly, Light-driven heterogeneous reduction of carbon dioxide: Photocatalysts and photoelectrodes, Chemical Reviews, 115 (2015) 12888-12935.

[22] T. Kawai, T. Sakata, Photocatalytic hydrogen production from water by the decomposition of poly-vinylchloride, protein, algae, dead insects, and excrement, Chemistry Letters, 10 (1981) 81-84.

[23] T. Sakata, T. Kawai, K. Hashimoto, Photochemical diode model of Pt/TiO_2 particle and its photocatalytic activity, Chemical Physics Letters, 88 (1982) 50-54.

[24] T. Kawai, T. Sakata, Photocatalytic hydrogen production from liquid methanol and water, Journal of the Chemical Society, Chemical Communications, (1980) 694-695.

[25] T. Sakata, T. Kawai, Heterogeneous photocatalytic production of hydrogen and methane from ethanol and water, Chemical Physics Letters, 80 (1981) 341-344.

[26] J.T. Schneider, D.S. Firak, R.R. Ribeiro, P. Peralta-Zamora, Use of scavenger agents in heterogeneous photocatalysis: truths, half-truths, and misinterpretations, Physical Chemistry Chemical Physics, 22 (2020) 15723-15733.

[27] F. Pellegrino, F. Sordello, M. Minella, C. Minero, V. Maurino, The role of surface texture on the photocatalytic H_2 production on TiO_2, Catalysts, 9 (2019) 32.

[28] T.R. Gordon, M. Cargnello, T. Paik, F. Mangolini, R.T. Weber, P. Fornasiero, C.B. Murray, Nonaqueous synthesis of TiO_2 nanocrystals using TiF_4 to engineer morphology, oxygen vacancy concentration, and photocatalytic activity, Journal of the American Chemical Society, 134 (2012) 6751-6761.

[29] L. Mino, F. Pellegrino, S. Rades, J. Radnik, V.-D. Hodoroaba, G. Spoto, V. Maurino, G. Martra, Beyond shape engineering of TiO_2 nanoparticles: post-synthesis treatment dependence of surface hydration, hydroxylation, Lewis acidity and photocatalytic activity of TiO_2 anatase nanoparticles with dominant {001} or {101} facets, ACS Applied Nano Materials, 1 (2018) 5355-5365.

[30] L. Mino, G. Spoto, S. Bordiga, A. Zecchina, Particles morphology and surface properties as investigated by HRTEM, FTIR, and periodic DFT calculations: From pyrogenic TiO_2 (P25) to nanoanatase, The Journal of Physical Chemistry C, 116 (2012) 17008-17018.

[31] F. Pellegrino, F. Sordello, L. Mino, C. Minero, V.-D. Hodoroaba, G. Martra, V. Maurino, Formic acid photoreforming for hydrogen production on shape-controlled anatase TiO_2 nanoparticles: assessment of the role of fluorides, {101}/{001} surfaces ratio, and platinization, ACS Catalysis, 9 (2019) 6692-6697.

[32] M.M. Momeni, Y. Ghayeb, Visible light-driven photoelectrochemical water splitting on ZnO–TiO_2 heterogeneous nanotube photoanodes, Journal of Applied Electrochemistry, 45 (2015) 557-566.

[33] P. Varadhan, H.-C. Fu, D. Priante, J.R.D. Retamal, C. Zhao, M. Ebaid, T.K. Ng, I. Ajia, S. Mitra, I.S. Roqan, B.S. Ooi, J.-H. He, Surface passivation of GaN nanowires for enhanced photoelectrochemical water-splitting, Nano Letters, 17 (2017) 1520-1528.

[34] J. He, Y.-e. Du, Y. Bai, J. An, X. Cai, Y. Chen, P. Wang, X. Yang, Q. Feng, Facile formation of anatase/rutile TiO_2 nanocomposites with enhanced photocatalytic activity, Molecules, 24 (2019) 2996.

[35] D.Y. Leung, X. Fu, C. Wang, M. Ni, M.K. Leung, X. Wang, X. Fu, Hydrogen production over titania-based photocatalysts, ChemSusChem, 3 (2010) 681-694.

[36] Q. Wang, J. Lian, Y. Bai, J. Hui, J. Zhong, J. Li, N. An, J. Yu, F. Wang, Photocatalytic activity of hydrogen production from water over TiO_2 with different crystal structures, Materials Science in Semiconductor Processing, 40 (2015) 418-423.

[37] L.-L. Tan, W.-J. Ong, S.-P. Chai, A.R. Mohamed, Band gap engineered, oxygen-rich TiO_2 for visible light induced photocatalytic reduction of CO_2, Chemical Communications, 50 (2014) 6923-6926.

[38] Y. Lu, B. Ma, Y. Yang, E. Huang, Z. Ge, T. Zhang, S. Zhang, L. Li, N. Guan, Y. Ma, Y. Chen, High activity of hot electrons from bulk 3D graphene materials for efficient photocatalytic hydrogen production, Nano Research, 10 (2017) 1662-1672.

[39] M.J. Muñoz-Batista, D. Rodríguez-Padrón, A.R. Puente-Santiago, A. Kubacka, R. Luque, M. Fernández-García, Sunlight-driven hydrogen production using an annular flow photoreactor and g-C_3N_4-based catalysts, ChemPhotoChem, 2 (2018) 870-877.

[40] J.B. Priebe, J. Radnik, A.J.J. Lennox, M.-M. Pohl, M. Karnahl, D. Hollmann, K. Grabow, U. Bentrup, H. Junge, M. Beller, A. Brückner, Solar hydrogen production by plasmonic Au–TiO_2 catalysts: Impact of synthesis protocol and TiO_2 phase on charge transfer efficiency and H_2 evolution rates, ACS Catalysis, 5 (2015) 2137-2148.

[41] H.-y. Lin, C.-y. Shih, Efficient one-pot microwave-assisted hydrothermal synthesis of M (M=Cr, Ni, Cu, Nb) and nitrogen co-doped TiO_2 for hydrogen production by photocatalytic water splitting, Journal of Molecular Catalysis A: Chemical, 411 (2016) 128-137.

[42] M.M. Fadlallah, Magnetic, electronic, optical, and photocatalytic properties of nonmetal- and halogen-doped anatase TiO_2 nanotubes, Physica E: Low-dimensional Systems and Nanostructures, 89 (2017) 50-56.

[43] E. Song, Y.-T. Kim, J. Choi, Anion additives in rapid breakdown anodization for nonmetal-doped TiO_2 nanotube powders, Electrochemistry Communications, 109 (2019) 106610.

[44] Y. Yalçın, M. Kılıç, Z. Çınar, The role of non-metal doping in TiO_2 photocatalysis, Journal of Advanced Oxidation Technologies, 13 (2010) 281-296.

[45] K. Villa, A. Black, X. Domènech, J. Peral, Nitrogen doped TiO_2 for hydrogen production under visible light irradiation, Solar Energy, 86 (2012) 558-566.

[46] C. Di Valentin, E. Finazzi, G. Pacchioni, A. Selloni, S. Livraghi, M.C. Paganini, E. Giamello, N-doped TiO_2: Theory and experiment, Chemical Physics, 339 (2007) 44-56.

[47] B. Ahmmad, K. Kanomata, F. Hirose, Enhanced photocatalytic hydrogen production on TiO_2 by using carbon materials, Int J Chem Mater Sci Eng, 8 (2014) 24-29.

[48] P. Zhang, T. Tachikawa, M. Fujitsuka, T. Majima, *In situ* fluorine doping of TiO_2 superstructures for efficient visible-light driven hydrogen generation, ChemSusChem, 9 (2016) 617-623.

[49] Y.Y. Gurkan, E. Kasapbasi, Z. Cinar, Enhanced solar photocatalytic activity of TiO_2 by selenium(IV) ion-doping: Characterization and DFT modeling of the surface, Chemical Engineering Journal, 214 (2013) 34-44.

[50] Y. Pan, M. Wen, Noble metals enhanced catalytic activity of anatase TiO_2 for hydrogen evolution reaction, International Journal of Hydrogen Energy, 43 (2018) 22055-22063.

[51] P. Munnik, P.E. de Jongh, K.P. de Jong, Recent developments in the synthesis of supported catalysts, Chemical Reviews, 115 (2015) 6687-6718.

[52] K. Kimura, H. Einaga, Y. Teraoka, Catalytic properties of platinum supported on titanium dioxide by liquid-phase adsorption of colloidal nanoparticles, Catalysis Letters, 139 (2010) 72-76.

[53] A. Esrafili, M. Salimi, A. jonidi jafari, H. Reza Sobhi, M. Gholami, R. Rezaei Kalantary, Pt-based TiO_2 photocatalytic systems: A systematic review, Journal of Molecular Liquids, 352 (2022) 118685.

[54] C. Xia, T. Hong Chuong Nguyen, X. Cuong Nguyen, S. Young Kim, D.L.T. Nguyen, P. Raizada, P. Singh, V.-H. Nguyen, C. Chien Nguyen, V. Chinh Hoang, Q. Van Le, Emerging cocatalysts in TiO_2-based photocatalysts for light-driven catalytic hydrogen evolution: Progress and perspectives, Fuel, 307 (2022) 121745.

[55] N.S. Ibrahim, W.L. Leaw, D. Mohamad, S.H. Alias, H. Nur, A critical review of metal-doped TiO_2 and its structure–physical properties–photocatalytic activity relationship in hydrogen production, International Journal of Hydrogen Energy, 45 (2020) 28553-28565.

[56] J. Zhang, X. Jin, P.I. Morales-Guzman, X. Yu, H. Liu, H. Zhang, L. Razzari, J.P. Claverie, Engineering the absorption and field enhancement properties of Au–TiO_2 nanohybrids via whispering gallery mode resonances for photocatalytic water splitting, ACS Nano, 10 (2016) 4496-4503.

[57] J. Wu, S. Lu, D. Ge, L. Zhang, W. Chen, H. Gu, Photocatalytic properties of Pd/TiO_2 nanosheets for hydrogen evolution from water splitting, RSC Advances, 6 (2016) 67502-67508.

[58] F. Wu, X. Hu, J. Fan, E. Liu, T. Sun, L. Kang, W. Hou, C. Zhu, H. Liu, Photocatalytic activity of Ag/TiO_2 nanotube arrays enhanced by surface plasmon resonance and application in hydrogen evolution by water splitting, Plasmonics, 8 (2013) 501-508.

[59] W. Ouyang, M.J. Muñoz-Batista, A. Kubacka, R. Luque, M. Fernández-García, Enhancing photocatalytic performance of TiO_2 in H_2 evolution via Ru co-catalyst deposition, Applied Catalysis B: Environmental, 238 (2018) 434-443.

[60] J. Huang, G. Li, Z. Zhou, Y. Jiang, Q. Hu, C. Xue, W. Guo, Efficient photocatalytic hydrogen production over Rh and Nb codoped TiO_2 nanorods, Chemical Engineering Journal, 337 (2018) 282-289.

[61] B. Banerjee, V. Amoli, A. Maurya, A.K. Sinha, A. Bhaumik, Green synthesis of Pt-doped TiO_2 nanocrystals with exposed (001) facets and mesoscopic void space for photo-splitting of water under solar irradiation, Nanoscale, 7 (2015) 10504-10512.

[62] I. Bahar, U. Deniz, On the limits of photocatalytic water splitting, in: E. Murat, Y. Ebubekir (Eds.) Water Chemistry, IntechOpen, Rijeka, 2019, pp. Ch. 10.

[63] Z.H.N. Al-Azri, M. AlOufi, A. Chan, G.I.N. Waterhouse, H. Idriss, Metal particle size effects on the photocatalytic hydrogen ion reduction, ACS Catalysis, 9 (2019) 3946-3958.

[64] T.W. van Deelen, C. Hernández Mejía, K.P. de Jong, Control of metal-support interactions in heterogeneous catalysts to enhance activity and selectivity, Nature Catalysis, 2 (2019) 955-970.

[65] M. Anpo, M. Takeuchi, The design and development of highly reactive titanium oxide photocatalysts operating under visible light irradiation, Journal of Catalysis, 216 (2003) 505-516.

[66] G. Kovács, F. Sz, A. Vulpoi, K. Schrantz, A. Dombi, K. Hernádi, V. Danciu, P. Zs, L. Baia, Polyhedral Pt vs. spherical Pt nanoparticles on commercial titanias: Is shape tailoring a guarantee of achieving high activity?, Journal of Catalysis, 325 (2015) 156-167.

[67] S. Fodor, G. Kovács, K. Hernádi, V. Danciu, L. Baia, Z. Pap, Shape tailored Pd nanoparticles' effect on the photocatalytic activity of commercial TiO_2, Catalysis Today, 284 (2017) 137-145.

[68] C. Hernández Mejía, T.W. van Deelen, K.P. de Jong, Activity enhancement of cobalt catalysts by tuning metal-support interactions, Nature Communications, 9 (2018) 4459.

[69] G.-M. Schwab, Alloy catalysts in dehydrogenation, Discussions of the Faraday Society, 8 (1950) 166-171.

[70] S.J. Tauster, S.C. Fung, R.L. Garten, Strong metal-support interactions. Group 8 noble metals supported on titanium dioxide, Journal of the American Chemical Society, 100 (1978) 170-175.

[71] J. Santos, J. Phillips, J.A. Dumesic, Metal-support interactions between iron and titania for catalysts prepared by thermal decomposition of iron pentacarbonyl and by impregnation, Journal of Catalysis, 81 (1983) 147-167.

[72] G.B. Raupp, J.A. Dumesic, Effect of titania surface species on the chemisorption of carbon monoxide and hydrogen on polycrystalline nickel, The Journal of Physical Chemistry, 88 (1984) 660-663.

[73] J.D. Bracey, R. Burch, Enhanced activity of $PdTiO_2$ catalysts for the COH_2 reaction in the absence of strong metal-support interactions (SMSI), Journal of Catalysis, 86 (1984) 384-391.

[74] A.D. Logan, E.J. Braunschweig, A.K. Datye, D.J. Smith, Direct observation of the surfaces of small metal crystallites: rhodium supported on titania, Langmuir, 4 (1988) 827-830.

[75] A.K. Datye, D.S. Kalakkad, M.H. Yao, D.J. Smith, Comparison of metal-support interactions in Pt/TiO_2 and Pt/CeO_2, Journal of Catalysis, 155 (1995) 148-153.

[76] J. Liu, Advanced electron microscopy characterization of nanostructured heterogeneous catalysts, Microscopy and Microanalysis, 10 (2004) 55-76.

[77] H. Chen, Z. Yang, X. Wang, F. Polo-Garzon, P.W. Halstenberg, T. Wang, X. Suo, S.Z. Yang, H.M. Meyer, 3rd, Z. Wu, S. Dai, Photoinduced strong metal-support interaction for enhanced catalysis, Journal of the American Chemical Society, 143 (2021) 8521-8526.

[78] A. Beck, X. Huang, L. Artiglia, M. Zabilskiy, X. Wang, P. Rzepka, D. Palagin, M.-G. Willinger, J.A. van Bokhoven, The dynamics of overlayer formation on catalyst nanoparticles and strong metal-support interaction, Nature Communications, 11 (2020) 3220.

[79] H. Frey, A. Beck, X. Huang, J.A. van Bokhoven, M.G. Willinger, Dynamic interplay between metal nanoparticles and oxide support under redox conditions, Science, 376 (2022) 982-987.

[80] S. Zhang, P.N. Plessow, J.J. Willis, S. Dai, M. Xu, G.W. Graham, M. Cargnello, F. Abild-Pedersen, X. Pan, Dynamical observation and detailed description of catalysts under strong metal–support interaction, Nano Letters, 16 (2016) 4528-4534.

[81] B.M. Weckhuysen, Determining the active site in a catalytic process: *Operando* spectroscopy is more than a buzzword, Physical Chemistry Chemical Physics, 5 (2003) 4351-4360.

[82] M.A. Bañares, M.O. Guerrero-Pérez, J.L.G. Fierro, G.G. Cortez, Raman spectroscopy during catalytic operations with on-line activity measurement (*operando* spectroscopy): a method for understanding the active centres of cations supported on porous materials, Journal of Materials Chemistry, 12 (2002) 3337-3342.

[83] T. Yoshida, Y. Minoura, Y. Nakano, M. Yamamoto, S. Yagi, H. Yoshida, XAFS study on a photodeposition process of Pt nanoparticles on TiO_2 photocatalyst, Journal of Physics: Conference Series, 712 (2016) 012076.

[84] C. Mu, C. Lv, X. Meng, J. Sun, Z. Tong, K. Huang, *In situ* characterization techniques applied in photocatalysis: A review, Advanced Materials Interfaces, 10 (2023) 2201842.

[85] B. Roldán Cuenya, M.A. Bañares, Introduction: *operando* and *in situ* studies in catalysis and electrocatalysis, Chemical Reviews, 124 (2024) 8011-8013.

[86] X. Wei, H. Liu, S. Gao, K. Jia, Z. Wang, J. Chen, Photocatalyst: To be dispersed or to be immobilized? The crucial role of electron transport in photocatalytic fixed bed reaction, The Journal of Physical Chemistry Letters, 13 (2022) 9642-9648.

[87] G.M. Haselmann, B. Baumgartner, J. Wang, K. Wieland, T. Gupta, C. Herzig, A. Limbeck, B. Lendl, D. Eder, *In situ* Pt photodeposition and methanol photooxidation on Pt/TiO_2: Pt-loading-dependent photocatalytic reaction pathways studied by liquid-phase infrared spectroscopy, ACS Catalysis, 10 (2020) 2964-2977.

[88] J.A. van Bokhoven, C. Lamberti, X-ray absorption and X-ray emission spectroscopy: theory and applications, Wiley & Sons, Chichester, 2016.

[89] L. Mino, G. Agostini, E. Borfecchia, D. Gianolio, A. Piovano, E. Gallo, C. Lamberti, Low-dimensional systems investigated by X-ray absorption spectroscopy: a selection of 2D, 1D and 0D cases, Journal of Physics D: Applied Physics, 46 (2013) Art. n. 423001.

[90] C. Giannini, V. Holy, L. De Caro, L. Mino, C. Lamberti, Watching nanomaterials with X-ray eyes: Probing different length scales by combining scattering with spectroscopy, Progress in Materials Science, 112 (2020).

[91] P.M. Abdala, O.V. Safonova, G. Wiker, W. van Beek, H. Emerich, J.A. van Bokhoven, J. Sá, J. Szlachetko, M. Nachtegaal, Scientific opportunities for heterogeneous catalysis research at the SuperXAS and SNBL beam lines, CHIMIA, 66 (2012) 699.

[92] S. Bordiga, E. Groppo, G. Agostini, J.A. van Bokhoven, C. Lamberti, Reactivity of surface species in heterogeneous catalysts probed by *in situ* X-ray absorption techniques, Chemical Reviews, 113 (2013) 1736-1850.

[93] J.A.L. van Bokhoven, C., X-Ray absorption and x-ray emission spectroscopy: Theory and applications, Wiley & Sons: Chichester, (2016) 896 Pages.

[94] D.F. Swinehart, The Beer-Lambert law, Journal of Chemical Education, 39 (1962) 333.

[95] H.E. Rose, Breakdown of the Lambert-Beer law, Nature, 169 (1952) 287-288.

[96] C. Natoli, Near edge absorption structure in the framework of the multiple scattering model. Potential resonance or barrier effects?, EXAFS and near edge structure, Springer1983, pp. 43-56.

[97] C. Natoli, Excitonic Resonances in X-Ray Absorption Near Edge, EXAFS and Near Edge Structure III: Proceedings of an International Conference, Springer Verlag, 1984, pp. 38.

[98] C. Natoli, Distance dependence of continuum and bound state of excitonic resonances in X-ray absorption near edge structure (XANES), EXAFS and near edge structure III, Springer1984, pp. 38-42.

[99] E.G. Kozyr, A.L. Bugaev, S.A. Guda, A.A. Guda, K.A. Lomachenko, K. Janssens, S. Smolders, D. De Vos, A.V. Soldatov, Speciation of Ru Molecular Complexes in a Homogeneous Catalytic System: Fingerprint XANES Analysis Guided by Machine Learning, The Journal of Physical Chemistry C, 125 (2021) 27844-27852.

[100] J. Timoshenko, D. Lu, Y. Lin, A.I. Frenkel, Supervised Machine-Learning-Based Determination of Three-Dimensional Structure of Metallic Nanoparticles, The Journal of Physical Chemistry Letters, 8 (2017) 5091-5098.

[101] Y. Lin, M. Topsakal, J. Timoshenko, D. Lu, S. Yoo, A.I. Frenkel, Machine-learning assisted structure determination of metallic nanoparticles: A benchmark, Handbook on Big Data and Machine Learning in the Physical Sciences, pp. 127-140.

[102] L. Piccolo, P. Afanasiev, F. Morfin, T. Len, C. Dessal, J.L. Rousset, M. Aouine, F. Bourgain, A. Aguilar-Tapia, O. Proux, Y. Chen, L. Soler, J. Llorca, *Operando* X-ray absorption spectroscopy investigation of photocatalytic hydrogen evolution over ultradispersed Pt/TiO_2 catalysts, ACS Catalysis, 10 (2020) 12696-12705.

[103] R. Khare, A. Jentys, J.A. Lercher, Development of photochemical and electrochemical cells for *operando* X-ray absorption spectroscopy during photocatalytic and electrocatalytic reactions, Physical Chemistry Chemical Physics, 22 (2020) 18891-18901.

[104] H. Issa Hamoud, L. Wolski, I. Pankin, M.A. Bañares, M. Daturi, M. El-Roz, *In situ* and *Operando* spectroscopies in photocatalysis: Powerful techniques for a better understanding of the performance and the reaction mechanism, Topics in Current Chemistry, 380 (2022) 37.

[105] S.J. Tinnemans, J.G. Mesu, K. Kervinen, T. Visser, T.A. Nijhuis, A.M. Beale, D.E. Keller, A.M.J. van der Eerden, B.M. Weckhuysen, Combining *operando* techniques in one spectroscopic-reaction cell: New opportunities for elucidating the active site and related reaction mechanism in catalysis, Catalysis Today, 113 (2006) 3-15.

[106] Y. Zhou, D.E. Doronkin, Z. Zhao, P.N. Plessow, J. Jelic, B. Detlefs, T. Pruessmann, F. Studt, J.-D. Grunwaldt, Photothermal catalysis over nonplasmonic Pt/TiO_2 studied by

operando HERFD-XANES, resonant XES, and DRIFTS, ACS Catalysis, 8 (2018) 11398-11406.

[107] M. Bauer, G. Heusel, S. Mangold, H. Bertagnolli, Spectroscopic set-up for simultaneous UV-Vis/(Q) EXAFS in situ and in *operando* studies of homogeneous reactions under laboratory conditions, Journal of Synchrotron Radiation, 17 (2010) 273-279.

[108] A.M. Beale, A.M.J. van der Eerden, K. Kervinen, M.A. Newton, B.M. Weckhuysen, Adding a third dimension to *operando* spectroscopy: a combined UV-Vis, Raman and XAFS setup to study heterogeneous catalysts under working conditions, Chemical Communications, (2005) 3015-3017.

[109] A.V. Chernyshev, A.A. Guda, A. Cannizzo, E.V. Solov'eva, N.A. Voloshin, Y. Rusalev, V.V. Shapovalov, G. Smolentsev, A.V. Soldatov, A.V. Metelitsa, *Operando* XAS and UV–Vis characterization of the photodynamic spiropyran–zinc complexes, The Journal of Physical Chemistry B, 123 (2019) 1324-1331.

[110] V.S.I. Sprakel, M.C. Feiters, R.J.M. Nolte, P.M.F.M. Hombergen, A. Groenen, H.J.R.D. Haas, A cell for combined UV-visible and X-ray absorption spectroscopy studies under low-temperature and air exclusion conditions, Review of Scientific Instruments, 73 (2002) 2994-2998.

[111] A. Zabilska, A.H. Clark, D. Ferri, M. Nachtegaal, O. Kröcher, O.V. Safonova, Beware of beam damage under reaction conditions: X-ray induced photochemical reduction of supported VO_x catalysts during *in situ* XAS experiments, Physical Chemistry Chemical Physics, 24 (2022) 21916-21926.

[112] O. Usoltsev, A. Tereshchenko, A. Skorynina, E. Kozyr, A. Soldatov, O. Safonova, A.H. Clark, F. D., M. Nachtegaal, A. Bugaev, Machine learning for quantitative structural information from infrared spectra: The case of palladium hydride, Small Methods, (2024) 2301397.

[113] Y. Zhou, D.E. Doronkin, M. Chen, S. Wei, J.-D. Grunwaldt, Interplay of Pt and crystal facets of TiO_2: CO oxidation activity and *operando* XAS/DRIFTS studies, ACS Catalysis, 6 (2016) 7799-7809.

[114] C. Dessal, T. Len, F. Morfin, J.-L. Rousset, M. Aouine, P. Afanasiev, L. Piccolo, Dynamics of single Pt atoms on alumina during CO oxidation monitored by *operando* X-ray and infrared spectroscopies, ACS Catalysis, 9 (2019) 5752-5759.

[115] L. Lukashuk, K. Foettinger, *In situ* and *operando* spectroscopy: A powerful approach towards understanding catalysts, Johnson Matthey Technology Review, 62 (2018) 316-331.

[116] P. Pichat, Representative examples of infrared spectroscopy uses in semiconductor photocatalysis, Catalysis Today, 224 (2014) 251-257.

[117] J.G. Highfield, M.H. Chen, P.T. Nguyen, Z. Chen, Mechanistic investigations of photo-driven processes over TiO_2 by *in-situ* DRIFTS-MS: Part 1. Platinization and methanol reforming, Energy & Environmental Science, 2 (2009) 991-1002.

[118] B. Hauchecorne, D. Terrens, S. Verbruggen, J.A. Martens, H. Van Langenhove, K. Demeestere, S. Lenaerts, Elucidating the photocatalytic degradation pathway of acetaldehyde: An FTIR *in situ* study under atmospheric conditions, Applied Catalysis B: Environmental, 106 (2011) 630-638.

[119] J.C.S. Wu, Y.-T. Cheng, *In situ* FTIR study of photocatalytic NO reaction on photocatalysts under UV irradiation, Journal of Catalysis, 237 (2006) 393-404.

[120] J.C.S. Wu, C.-W. Huang, *In situ* DRIFTS study of photocatalytic CO_2 reduction under UV irradiation, Frontiers of Chemical Engineering in China, 4 (2010) 120-126.

[121] L. Mino, C. Negri, A. Zecchina, G. Spoto, Photodegradation of organic pollutants on TiO_2 P25 surfaces investigated by transmission FTIR spectroscopy under *in situ* UV-Vis irradiation, Zeitschrift für Physikalische Chemie, 230 (2016) 1441-1451.

[122] S. Kataoka, M.I. Tejedor-Tejedor, J.M. Coronado, M.A. Anderson, Thin-film transmission IR spectroscopy as an in situ probe of the gas–solid interface in photocatalytic processes, Journal of Photochemistry and Photobiology A: Chemistry, 163 (2004) 323-329.

[123] I. Dolamic, T. Bürgi, Photocatalysis of dicarboxylic acids over TiO_2: An in situ ATR-IR study, Journal of Catalysis, 248 (2007) 268-276.

[124] J. Dankar, C. Pagis, M. Rivallan, M. El-Roz, *Operando* FTIR study of the photocatalytic reduction of CO_2 in the presence of water vapor over Pt/TiO_2: on the role of surface residual C-species, Sustainable Energy & Fuels, 7 (2023) 2819-2823.

[125] M. El-Roz, P. Bazin, F. Thibault-Starzyk, An *operando*-IR study of photocatalytic reaction of methanol on new *BEA supported TiO_2 catalyst, Catalysis Today, 205 (2013) 111-119.

[126] O. Usoltsev, A. Tereshchenko, A. Skorynina, E. Kozyr, A. Soldatov, O. Safonova, A.H. Clark, D. Ferri, M. Nachtegaal, A. Bugaev, Machine learning for quantitative structural information from infrared spectra: The case of palladium hydride, Small Methods, 8 (2024) e2301397.

[127] S.W. Chee, T. Lunkenbein, R. Schlögl, B. Roldán Cuenya, *Operando* electron microscopy of catalysts: The missing cornerstone in heterogeneous catalysis research, Chemical Reviews, 123 (2023) 13374-13418.

[128] Z.-W. Yin, S.B. Betzler, T. Sheng, Q. Zhang, X. Peng, J. Shangguan, K.C. Bustillo, J.-T. Li, S.-G. Sun, H. Zheng, Visualization of facet-dependent pseudo-photocatalytic behavior of TiO_2 nanorods for water splitting using *in situ* liquid cell TEM, Nano Energy, 62 (2019) 507-512.

[129] B. Weng, Y. Jiang, H.-G. Liao, M.B.J. Roeffaers, F. Lai, H. Huang, Z. Tang, Visualizing light-induced dynamic structural transformations of Au clusters-based photocatalyst via *in situ* TEM, Nano Research, 14 (2021) 2805-2809.

[130] F. Cavalca, A.B. Laursen, B.E. Kardynal, R.E. Dunin-Borkowski, S. Dahl, J.B. Wagner, T.W. Hansen, *In situ* transmission electron microscopy of light-induced photocatalytic reactions, Nanotechnology, 23 (2012) 075705.

[131] C. Deiana, M. Minella, G. Tabacchi, V. Maurino, E. Fois, G. Martra, Shape-controlled TiO_2 nanoparticles and TiO_2 P25 interacting with CO and H_2O_2 molecular probes: a synergic approach for surface structure recognition and physico-chemical understanding, Physical Chemistry Chemical Physics, 15 (2013) 307-315.

[132] T.A. Kandiel, A.A. Ismail, D.W. Bahnemann, Mesoporous TiO_2 nanostructures: a route to minimize Pt loading on titania photocatalysts for hydrogen production, Physical Chemistry Chemical Physics, 13 (2011) 20155-20161.

[133] B. Rusinque, S. Escobedo, H. de Lasa, Photoreduction of a Pd-doped mesoporous TiO_2 photocatalyst for hydrogen production under visible light, Catalysts, 10 (2020) 74.

[134] K. Wenderich, G. Mul, Methods, mechanism, and applications of photodeposition in photocatalysis: A review, Chemical Reviews, 116 (2016) 14587-14619.

[135] D. Bellet, B. Gorges, A. Dallery, P. Bernard, E. Pereiro, J. Baruchel, A 1300 K furnace for *in situ* X-ray microtomography, Journal of Applied Crystallography, 36 (2003) 366-367.

[136] B. Ravel, M. Newville, ATHENA, ARTEMIS, HEPHAESTUS: data analysis for X-ray absorption spectroscopy using IFEFFIT, Journal of Synchrotron Radiation, 12 (2005) 537-541.

[137] G.L. Chiarello, M. Nachtegaal, V. Marchionni, L. Quaroni, D. Ferri, Adding diffuse reflectance infrared Fourier transform spectroscopy capability to extended X-ray-absorption fine structure in a new cell to study solid catalysts in combination with a modulation approach, Review of Scientific Instruments, 85 (2014).

[138] P.M. Abdala, O.V. Safonova, G. Wiker, W. van Beek, H. Emerich, J.A. van Bokhoven, J. Sá, J. Szlachetko, M. Nachtegaal, Scientific opportunities for heterogeneous catalysis research at the SuperXAS and SNBL beam lines, Chimia (Aarau), 66 (2012) 699-705.

[139] A.H. Clark, J. Imbao, R. Frahm, M. Nachtegaal, ProQEXAFS: a highly optimized parallelized rapid processing software for QEXAFS data, Journal of Synchrotron Radiation, 27 (2020) 551-557.

[140] V. Petříček, M. Dušek, L. Palatinus, Crystallographic computing system JANA2006: General features, Zeitschrift für Kristallographie - Crystalline Materials, 229 (2014) 345-352.

[141] T.J. Collins, ImageJ for microscopy, BioTechniques, 43 (2007) S25-S30.

[142] E.P. Melián, C.R. López, A.O. Méndez, O.G. Díaz, M.N. Suárez, J.M. Doña Rodríguez, J.A. Navío, D. Fernández Hevia, Hydrogen production using Pt-loaded TiO_2 photocatalysts, International Journal of Hydrogen Energy, 38 (2013) 11737-11748.

[143] N.-T. Nguyen, D.-D. Zheng, S.-S. Chen, C.-T. Chang, Preparation and photocatalytic hydrogen production of pt-graphene/TiO_2 composites from water splitting, Journal of Nanoscience and Nanotechnology, 18 (2018) 48-55.

[144] M.-Y. Xie, K.-Y. Su, X.-Y. Peng, R.-J. Wu, M. Chavali, W.-C. Chang, Hydrogen production by photocatalytic water-splitting on Pt-doped TiO_2–ZnO under visible light, Journal of the Taiwan Institute of Chemical Engineers, 70 (2017) 161-167.

[145] G.L. Chiarello, M.V. Dozzi, M. Scavini, J.-D. Grunwaldt, E. Selli, One step flame-made fluorinated Pt/TiO_2 photocatalysts for hydrogen production, Applied Catalysis B: Environmental, 160-161 (2014) 144-151.

[146] H. Belhadj, S. Hamid, P.K.J. Robertson, D.W. Bahnemann, Mechanisms of simultaneous hydrogen production and formaldehyde oxidation in H_2O and D_2O over platinized TiO_2, ACS Catalysis, 7 (2017) 4753-4758.

[147] A. Watanabe, M. Kajita, J. Kim, A. Kanayama, K. Takahashi, T. Mashino, Y. Miyamoto, *In vitro* free radical scavenging activity of platinum nanoparticles, Nanotechnology, 20 (2009) 455105.

[148] Y. Obara, H. Ito, T. Ito, N. Kurahashi, S. Thürmer, H. Tanaka, T. Katayama, T. Togashi, S. Owada, Y.I. Yamamoto, S. Karashima, J. Nishitani, M. Yabashi, T. Suzuki, K. Misawa, Femtosecond time-resolved X-ray absorption spectroscopy of anatase TiO_2 nanoparticles using XFEL, Struct Dyn, 4 (2017) 044033.

[149] L. Chang, S.T. Yong, S.P. Chai, L.K. Putri, L.L. Tan, A.R. Mohamed, A review of methanol photoreforming: Elucidating the mechanisms, photocatalysts and recent advancement strategies, Materials Today Chemistry, 27 (2023) 101334.

[150] Z. Xiong, Z. Lei, X. Chen, B. Gong, Y. Zhao, J. Zhang, C. Zheng, J.C.S. Wu, CO_2 photocatalytic reduction over Pt deposited TiO_2 nanocrystals with coexposed {101} and {001} facets: effect of deposition method and Pt precursors, Catalysis Communications, 96 (2017) 1-5.

[151] W. Lin, H. Zheng, P. Zhang, T. Xu, Pt deposited TiO_2 films with exposed {001} facets for photocatalytic degradation of a pharmaceutical pollutant, Applied Catalysis A: General, 521 (2016) 75-82.

[152] C.M. Pecoraro, L. Mino, E. Kozyr, L. Palmisano, Pt-TiO_2 catalysts for glycerol photoreforming: impact of surface hydration of anatase, brookite and rutile polymorphs, reactions, 3 9.

[153] M. Wang, Y. Zhang, Z. Wu, Y. Zheng, Z. Zhou, W. Weng, Redox dynamics of platinum species on CeO_2 during CO oxidation reaction, Chemical Engineering Journal, 450 (2022) 138171.

[154] M. Macino, A.J. Barnes, S.M. Althahban, R. Qu, E.K. Gibson, D.J. Morgan, S.J. Freakley, N. Dimitratos, C.J. Kiely, X. Gao, Tuning of catalytic sites in Pt/TiO_2 catalysts for the chemoselective hydrogenation of 3-nitrostyrene, Nature Catalysis, 2 (2019) 873-881.

[155] L. Lan, H. Daly, Y. Jiao, Y. Yan, C. Hardacre, X. Fan, Comparative study of the effect of TiO_2 support composition and Pt loading on the performance of Pt/TiO_2 photocatalysts for catalytic photoreforming of cellulose, International Journal of Hydrogen Energy, 46 (2021) 31054-31066.

[156] H. Tang, Y. Su, B. Zhang, A.F. Lee, M.A. Isaacs, K. Wilson, L. Li, Y. Ren, J. Huang, M. Haruta, B. Qiao, X. Liu, C. Jin, D. Su, J. Wang, T. Zhang, Classical strong metal–support interactions between gold nanoparticles and titanium dioxide, Science Advances, 3 (2017) e1700231.

[157] J. Li, Y. Lin, X. Pan, D. Miao, D. Ding, Y. Cui, J. Dong, X. Bao, Enhanced CO_2 methanation activity of Ni/anatase catalyst by tuning strong metal–support interactions, ACS Catalysis, 9 (2019) 6342-6348.

[158] S. Li, Y. Xu, Y. Chen, W. Li, L. Lin, M. Li, Y. Deng, X. Wang, B. Ge, C. Yang, S. Yao, J. Xie, Y. Li, X. Liu, D. Ma, Tuning the selectivity of catalytic carbon dioxide hydrogenation over iridium/cerium oxide catalysts with a strong metal–support interaction, Angewandte Chemie International Edition, 56 (2017) 10761-10765.

[159] E.W. Zhao, H. Zheng, K. Ludden, Y. Xin, H.E. Hagelin-Weaver, C.R. Bowers, Strong metal–support interactions enhance the pairwise selectivity of parahydrogen addition over Ir/TiO_2, ACS Catalysis, 6 (2016) 974-978.

[160] M. Xu, S. Yao, D. Rao, Y. Niu, N. Liu, M. Peng, P. Zhai, Y. Man, L. Zheng, B. Wang, B. Zhang, D. Ma, M. Wei, Insights into interfacial synergistic catalysis over Ni@TiO_{2-x} catalyst toward water–gas shift reaction, Journal of the American Chemical Society, 140 (2018) 11241-11251.

[161] Z. Cai, J. Dai, W. Li, K.B. Tan, Z. Huang, G. Zhan, J. Huang, Q. Li, Pd supported on MIL-68(In)-derived In_2O_3 nanotubes as superior catalysts to boost CO_2 hydrogenation to methanol, ACS Catalysis, 10 (2020) 13275-13289.

[162] C.J. Breckner, K. Zhu, M. Wang, G. Zhang, C.W. Li, J.T. Miller, Controlled site coverage of strong metal–support interaction (SMSI) on Pd NP catalysts, Catalysis Science & Technology, 13 (2023) 157-169.

[163] M. Bowker, P. Stone, R. Bennett, N. Perkins, CO adsorption on a Pd/TiO_2(110) model catalyst, Surface Science, 497 (2002) 155-165.

[164] M.A. Aramendía, J.C. Colmenares, A. Marinas, J.M. Marinas, J.M. Moreno, J.A. Navío, F.J. Urbano, Effect of the redox treatment of Pt/TiO_2 system on its photocatalytic behaviour in the gas phase selective photooxidation of propan-2-ol, Catalysis Today, 128 (2007) 235-244.

[165] M. Zhang, Z. Jin, Z. Zhang, H. Dang, Study of strong interaction between Pt and TiO_2 under oxidizing atmosphere, Applied Surface Science, 250 (2005) 29-34.

[166] H. Tang, Y. Su, Y. Guo, L. Zhang, T. Li, K. Zang, F. Liu, L. Li, J. Luo, B. Qiao, J. Wang, Oxidative strong metal–support interactions (OMSI) of supported platinum-group metal catalysts, Chemical Science, 9 (2018) 6679-6684.

[167] A. Yamamoto, J. Ohyama, K. Teramura, T. Shishido, T. Tanaka, Effect of a crystalline phase of TiO_{-2} photocatalysts on the photodeposition of Rh metal nanoparticles, Catalysis Today, 232 (2014) 165-170.

[168] B.-J. Hsieh, M.-C. Tsai, C.-J. Pan, W.-N. Su, J. Rick, H.-L. Chou, J.-F. Lee, B.-J. Hwang, Tuning metal support interactions enhances the activity and durability of TiO_2-supported Pt nanocatalysts, Electrochimica Acta, 224 (2017) 452-459.

[169] A.L. Bugaev, V.V. Srabionyan, A.V. Soldatov, L.A. Bugaev, J.A. van Bokhoven, The role of hydrogen in formation of Pd XANES in Pd-nanoparticles, Journal of Physics: Conference Series, 430 (2013) 012028.

[170] A.L. Bugaev, A.A. Guda, K.A. Lomachenko, A. Lazzarini, V.V. Srabionyan, J.G. Vitillo, A. Piovano, E. Groppo, L.A. Bugaev, A.V. Soldatov, V.P. Dmitriev, R. Pellegrini, J.A. van Bokhoven, C. Lamberti, Hydride phase formation in carbon supported palladium hydride nanoparticles by *in situ* EXAFS and XRD, Journal of Physics: Conference Series, 712 (2016) 012032.

[171] A.L. Bugaev, A.A. Guda, I.A. Pankin, E. Groppo, R. Pellegrini, A. Longo, A.V. Soldatov, C. Lamberti, The role of palladium carbides in the catalytic hydrogenation of ethylene over supported palladium nanoparticles, Catalysis Today, 336 (2019) 40-44.

[172] E.G. Kozyr, P.N. Njoroge, S.V. Chapek, V.V. Shapovalov, A.A. Skorynina, A.Y. Pnevskaya, A.N. Bulgakov, A.V. Soldatov, F. Pellegrino, E. Groppo, S. Bordiga, L. Mino, A.L. Bugaev, *Operando* laboratory X-ray absorption spectroscopy and UV–Vis study of Pt/TiO_2 photocatalysts during photodeposition and hydrogen evolution reactions, Catalysts, 13 (2023) 414.

[173] F. Sordello, M. Prozzi, V.-D. Hodoroaba, J. Radnik, F. Pellegrino, Increasing the HER efficiency of photodeposited metal nanoparticles over TiO_2 using controlled periodic illumination, Journal of Catalysis, 429 (2024).

[174] E. Kozyr, S. Martí-Sánchez, A. Skorynina, J. Arbiol, C. Escudero, L. Mino, A. Bugaev, *In situ* photodeposition of ultra-small palladium particles on TiO_2, Journal of Synchrotron Radiation, 31 (2024).

[175] G. Agostini, E. Groppo, A. Piovano, R. Pellegrini, G. Leofanti, C. Lamberti, Preparation of supported pd catalysts: From the pd precursor solution to the deposited Pd^{2+} phase, Langmuir, 26 (2010) 11204-11211.

[176] E. Groppo, G. Agostini, A. Piovano, N.B. Muddada, G. Leofanti, R. Pellegrini, G. Portale, A. Longo, C. Lamberti, Effect of reduction in liquid phase on the properties and the catalytic activity of Pd/Al_2O_3 catalysts, Journal of Catalysis, 287 (2012) 44-54.
[177] O. Usoltsev, D. Stoian, A. Skorynina, E. Kozyr, P.N. Njoroge, R. Pellegrini, E. Groppo, J.A. van Bokhoven, A. Bugaev, Restructuring of palladium nanoparticles during oxidation by molecular oxygen, Small, (2024) 2401184.
[178] A.L. Bugaev, M. Zabilskiy, A.A. Skorynina, O.A. Usoltsev, A.V. Soldatov, J.A. van Bokhoven, *In situ* formation of surface and bulk oxides in small palladium nanoparticles, Chemical Communications, 56 (2020) 13097-13100.
[179] G. Agostini, C. Lamberti, R. Pellegrini, G. Leofanti, F. Giannici, A. Longo, E. Groppo, Effect of pre-reduction on the properties and the catalytic activity of Pd/carbon catalysts: A comparison with Pd/Al_2O_3, ACS Catalysis, 4 (2014) 187-194.
[180] O. Usoltsev, A. Tereshchenko, A. Skorynina, E. Kozyr, A. Soldatov, O. Safonova, A.H. Clark, F. D., M. Nachtegaal, A. Bugaev, Machine learning for quantitative structural information from infrared spectra: The case of palladium hydride, Small Methods, 8 (2024) 2301397.
[181] O.A. Usoltsev, A.A. Skorynina, B.O. Protsenko, V. Martin-Diaconescu, R. Pellegrini, A.V. Soldatov, J. van Bokhoven, A.L. Bugaev, Evolution of surface and bulk structure of supported palladium nanoparticles by *in situ* X-ray absorption and infrared spectroscopies: Effect of temperature, CO and CH_4 gas, Applied Surface Science, 614 (2023) 156171.
[182] X. Du, Y. Huang, X. Pan, B. Han, Y. Su, Q. Jiang, M. Li, H. Tang, G. Li, B. Qiao, Size-dependent strong metal-support interaction in TiO_2 supported Au nanocatalysts, Nature Communications, 11 (2020) 5811.
[183] S.O. Baumann, M.J. Elser, M. Auer, J. Bernardi, N. Hüsing, O. Diwald, Solid−Solid Interface Formation in TiO_2 Nanoparticle Networks, Langmuir, 27 (2011) 1946-1953.
[184] M. Chiesa, M.C. Paganini, S. Livraghi, E. Giamello, Charge trapping in TiO_2 polymorphs as seen by electron paramagnetic resonance spectroscopy, Physical Chemistry Chemical Physics, 15 (2013) 9435-9447.
[185] S. Livraghi, M. Rolando, S. Maurelli, M. Chiesa, M.C. Paganini, E. Giamello, Nature of reduced states in titanium dioxide as monitored by electron paramagnetic resonance. Ii: Rutile and brookite cases, The Journal of Physical Chemistry C, 118 (2014) 22141-22148.
[186] H. Qiu, X. Ma, C. Sun, B. Zhao, F. Chen, Surface oxygen vacancies enriched Pt/TiO_2 synthesized with a defect migration strategy for superior photocatalytic activity, Applied Surface Science, 506 (2020) 145021.
[187] S. Pantaleone, F. Pellegrino, V. Maurino, M. Corno, P. Ugliengo, L. Mino, Disclosing the true atomic structure of {001} facets in shape-engineered TiO_2 anatase nanoparticles, Journal of Materials Chemistry A, 12 (2024) 4325-4332.
[188] T. Wang, X. Tao, X. Li, K. Zhang, S. Liu, B. Li, Synergistic Pd single atoms, clusters, and oxygen vacancies on TiO_2 for photocatalytic hydrogen evolution coupled with selective organic oxidation, Small, 17 (2021) e2006255.
[189] Y. Guo, Y. Huang, B. Zeng, B. Han, M. Akri, M. Shi, Y. Zhao, Q. Li, Y. Su, L. Li, Q. Jiang, Y.-T. Cui, L. Li, R. Li, B. Qiao, T. Zhang, Photo-thermo semi-hydrogenation of acetylene on Pd1/TiO_2 single-atom catalyst, Nature Communications, 13 (2022) 2648.

[190] C.M. Pecoraro, L. Mino, E. Kozyr, L. Palmisano, F. di Franco, V. Loddo, M. Santamaria, M. Bellardita, Pt–TiO_2 catalysts for glycerol photoreforming: comparison of anatase, brookite and rutile polymorphs, Chemical Communications, 60 (2024) 3782-3785.

[191] O. Usoltsev, D. Stoian, A. Skorynina, E. Kozyr, P.N. Njoroge, R. Pellegrini, E. Groppo, J.A. van Bokhoven, A. Bugaev, Restructuring of palladium nanoparticles during oxidation by molecular oxygen, Small, n/a (2024) 2401184.

[192] A.A. Skorynina, A. Lazzarini, D.K. Sannes, E.G. Kozyr, C. Ahoba-Sam, S. Bordiga, U. Olsbye, A.L. Bugaev, The structure of Pd-functionalized UiO-67 during CO_2 hydrogenation, Journal of Materials Chemistry C, 12 (2024) 3564-3572.

[193] L. Van Emelen, R. Lemmens, E. Kozyr, A.L. Bugaev, K. Janssens, R. de Oliveira-Silva, W. Stuyck, C. Marquez, H. Van Dessel, D. Sakellariou, D.E. De Vos, Ligand-free Pd^{II}/Ag^{I}-catalysed electrophilic amidation of simple arenes with O-acetyl acetohydroxamic acid, Catalysis Today, 437 (2024) 114748.

[194] K. Janssens, A.L. Bugaev, E.G. Kozyr, V. Lemmens, A.A. Guda, O.A. Usoltsev, S. Smolders, A.V. Soldatov, D.E. De Vos, Evolution of the active species of homogeneous Ru hydrodeoxygenation catalysts in ionic liquids, Chemical Science, 13 (2022) 10251-10259.

[195] P.V. Shvets, P.A. Prokopovich, A.I. Dolgoborodov, O.A. Usoltsev, A.A. Skorynina, E.G. Kozyr, V.V. Shapovalov, A.A. Guda, A.L. Bugaev, E.R. Naranov, D.N. Gorbunov, K. Janssens, D.E. De Vos, A.L. Trigub, E. Fonda, M.B. Leshchinsky, V.R. Zagackij, A.V. Soldatov, A.Y. Goikhman, *In situ* X-ray absorption spectroscopy cells for high pressure homogeneous catalysis, Catalysts, 12 (2022) 1264.